LOW TEMPERATURE SPECIFIC HEAT OF Li_xNbS_2 INTERCALATION COMPOUNDS

by

DOUGLAS C. DAHN

B.Sc., Dalhousie University, 1977

M.Sc., Dalhousie University, 1980

A THESIS SUBMITTED IN PARTIAL FULFILMENT OF

THE REQUIREMENTS FOR THE DEGREE OF

DOCTOR OF PHILOSOPHY

in

THE FACULTY OF GRADUATE STUDIES

Department of Physics

We accept this thesis as conforming

to the required standard

THE UNIVERSITY OF BRITISH COLUMBIA

July 1985

In presenting this thesis in partial fulfilment of the requirements for an advanced degree at the The University of British Columbia, I agree that the Library shall make it freely available for reference and study. I further agree that permission for extensive copying of this thesis for scholarly purposes may be granted by the Head of my Department or by his or her representatives. It is understood that copying or publication of this thesis for financial gain shall not be allowed without my written permission.

Department of Physics

The University of British Columbia
2075 Wesbrook Place
Vancouver, Canada
V6T 1W5

Date: July 1985

Abstract

This thesis describes a study of the low temperature specific heat of Li_xNbS_2, where x is between 0 and 1. Samples were prepared by intercalating lithium into niobium disulfide in electrochemical cells. Structural data obtained by x-ray diffraction are presented. These, together with electrochemical measurements, show that staged phases exist for some values of x. The electronic specific heat of Li_xNbS_2 is consistent with complete charge transfer from the intercalated lithium to the bands of the NbS_2 host. The lattice specific heat also shows large changes as a function of x. A discussion of the data in terms of continuum elasticity theory suggests that intercalation produces large changes in the shear elastic constant c_{44}. A brief discussion of superconductivity in Li_xNbS_2 is also included.

Table of Contents

List of Tables

List of Figures

Acknowledgements

It is a pleasure to thank Jim Carolan and Rudi Haering for their guidance and encouragement throughout this project. I have also benefited from working with numerous other people both in the low temperature physics lab and in Rudi's intercalation research group. My co-workers have been a constant source of support, and I wish to thank all of them.

Several people have made important direct contributions to the work described in this thesis, and should be mentioned by name. Joos Perenboom and Barbara Frisken helped with the design of the cryostat. Beat Meyer's expert machine work and helpful suggestions are appreciated. Summer students Ravi Menon and Jeff Beis assisted with the specific heat experiment on many occasions. Steven Steel and Walter Hardy calibrated one of the thermometers used in the cryostat. Walter and his students also were always an invaluable source of advice on low temperature techniques. Ed Sternin made the NMR measurements mentioned on page 13. I also wish to thank Birger Bergersen, Jeff Dahn, and John Berlinsky for their interest and for useful discussions.

Financial support from the Faculty of Graduate Studies in the form of a University Graduate Fellowship is gratefully acknowledged.

Finally, I would like to thank my wife Julia and our children for their support and encouragement.

1. INTRODUCTION

1.1 INTERCALATION

Intercalation, as the term is used here, is the reversible insertion of 'guest' atoms or molecules into a 'host' solid, in such a way that the crystal structure of the host is not drastically altered. A necessary condition for intercalation is the existence of sites in the host which are available for occupation by the guest. These sites must be accessible from the surface of the host, and the guest, or intercalant, must be mobile in the host. Perhaps the best known intercalation host is graphite, in which a wide variety of atoms and molecules can be inserted between the carbon layers. Graphite intercalation compounds have been comprehensively reviewed by Dresselhaus and Dresselhaus (1981). Other layered materials which have been shown to be intercalation hosts include some of the layered silicates, and the layered transition metal dichalcogenides (LTMDs) such as NbS_2. For reviews of intercalation in the LTMDs see Whittingham and Jacobson (1982), Whittingham (1978), Levy (1979), or Marseglia (1983). Intercalation has also been observed in some non-layered hosts; for example lithium intercalates into V_2O_5 (Murphy et al. 1979) and some of the other transition metal oxides, and into Mo_6S_8 (Schollhorn and Kumpers 1977, Mulhern 1982).

Electrochemical cells based on intercalation (Whittingham 1976) have received a great deal of attention

in recent years, since they can form the basis of long life, high energy density rechargable batteries. The most promising systems from a practical point of view are those involving lithium intercalation into the LTMDs. Cells based on lithium intercalation into TiS_2 have been studied extensively (J.R.Dahn 1982, Whittingham 1979) and Li/MoS_2 cells (Py and Haering 1983) are now being produced commercially[1]. This thesis is concerned with the intercalation compound Li_xNbS_2, which can also be prepared and studied by means of electrochemical intercalation. A schematic diagram of a Li/Li_xNbS_2 cell is shown in figure 1, to illustrate the operation of an intercalation cell. The half cell reactions are

$$xLi \leftrightarrow xLi^+ + xe^- \qquad (1\text{-}1)$$

at the lithium metal anode and

$$xLi^+ + xe^- + NbS_2 \leftrightarrow Li_xNbS_2 \qquad (1\text{-}2)$$

at the Li_xNbS_2 cathode. The electrons move from the anode to the cathode through an external circuit, and the Li^+ ion moves through the electrolyte.

In addition to their practical applications, intercalation cells can be used to obtain a great deal of thermodynamic information about the intercalation compound. This is because the open circuit voltage of a lithium intercalation cell is given by (McKinnon and Haering 1983)

---

[1]Moli Energy Ltd., Burnaby, B.C.

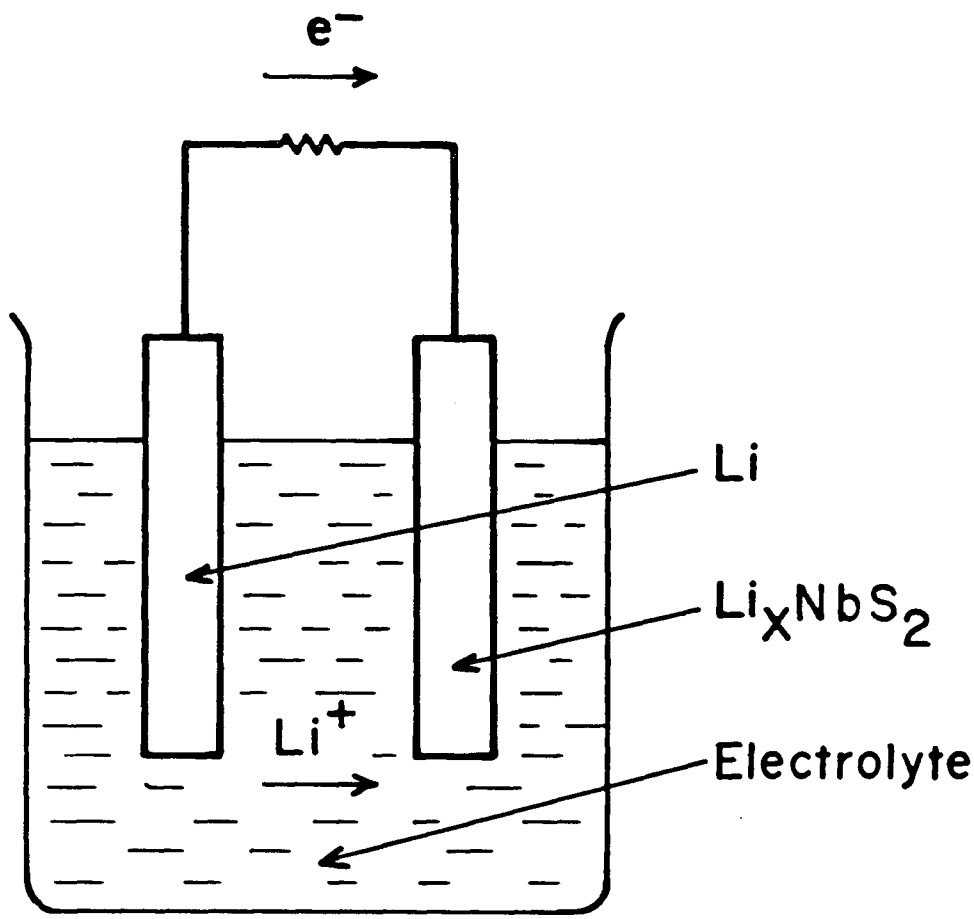

Figure 1: Schematic diagram of an intercalation cell. The electrolyte consists of a lithium salt dissolved in an organic solvent.

$$V(x)=(\mu_a-\mu_c)/e \qquad (1-3)$$

where μ_a and μ_c are the chemical potentials of lithium atoms in the anode and cathode, respectively, and e is the electronic charge.

A complete review of the literature of intercalation cells would be beyond the scope of this thesis, so only a few examples will be given. High resolution electrochemical measurements of V(x) and $\partial x/\partial V$ (J.R.Dahn and McKinnon 1984a) can be compared with theoretical models of the intercalation compound (Dahn, Dahn, and Haering 1982, McKinnon and Haering 1983). These and related electrochemical techniques have been used to study a number of phenomena which occur in layered intercalation compounds. One of these is staging. An intercalation compound of stage n is one in which every n^{th} interlayer gap contains a higher concentration of guest than the intervening n-1 gaps. Staging is best known in the graphite intercalation compounds, and also occurs in some of the intercalated LTMDs, such as Ag_xTaS_2 (Scholtz and Frindt 1980), Li_xNbSe_2 (D.C.Dahn and Haering 1982) and Li_xNbS_2. Li_xTaS_2 (J.R.Dahn and McKinnon 1984b) exhibits staging as well as two-dimensional lithium ordering in the interlayer gaps. In addition to V(x) measurements, the temperature coefficient $\partial V/\partial T$ of cell voltage has been used to obtain the entropy of intercalation compounds (J.R.Dahn and Haering 1983).

Intercalation cells can also be used as a convenient sample preparation technique, and it is primarily in this role that they appear in this thesis. By preparing a Li/NbS_2 cell and allowing it to discharge, the cathode material is converted to Li_xNbS_2, where x can be accurately determined by time-integrating the cell current. As shown in Chapter 2 for Li_xNbS_2, materials prepared this way may be in a different crystal phase than materials of the same composition prepared by other methods such as direct high temperature reaction of the elements.

1.2 NIOBIUM DISULFIDE

NbS_2 is one of the layered transition metal dichalcogenides. These are compounds of the form MX_2, where M is a group IV, V, or VI transition metal and X is sulfur, selenium, or tellurium. The LTMDs consist of strong covalently bonded MX_2 layers separated by so-called Van der Waals gaps. The interlayer bonding is relatively weak, although it is no longer believed to be due entirely to the Van der Waals interaction (Umrigar et al. 1983, Hibma 1982). A number of review articles dealing with the LTMDs (Wilson and Yoffe 1969, Yoffe 1973, Hullinger 1976, Lieth and Terhill 1977, Vandenberg-Voorhoeve 1976), their charge density waves (Wilson et al. 1975, Williams 1976), and superconductivity (Frindt and Huntley 1976), are available, and I will therefore restrict the following discussion to NbS_2 as much as possible.

NbS_2 is found in two polytypes; one (referred to as 2H) with a two layer high hexagonal unit cell and one (3R) with a three layer rhombohedral structure. The NbS_2 used in this work was 2H. These structures are shown in figure 2. If we consider the structures as stacks of two dimensional close packed planes, the stacking sequences are BaB-CaC for 2H-NbS_2 and BaB-CbC-AcA for 3R-NbS_2. The letters refer to the three inequivalent positions marked in figures 2 and 3. Capital letters refer to S and small letters to Nb. By analogy with Li_xTiS_2 (J.R.Dahn et al. 1980), intercalated lithium atoms are believed to lie in the octahedrally coordinated sites in the interlayer gaps.

1.3 BAND STRUCTURE AND THE RIGID BAND CHARGE TRANSFER MODEL

The electronic energy band schemes for NbS_2 and the other LTMDs first proposed by Wilson and Yoffe (1969) have since been confirmed by a number of experiments, as well as by detailed band structure calculations (Mattheis 1973, Wexler and Wooley 1976). The qualitative features of the 2H-NbS_2 bands are shown in figure 4. The valence bands are predominantly of sulfur 3s and 3p character, and the partially filled conduction band is derived primarily from niobium 4d states. The 3R polytype has an almost identical density of states, at least for the d states, since the coordination of S around Nb is trigonal prismatic in both polytypes, and this is the most important factor in determining the d state splitting. NbS_2 is metallic, since

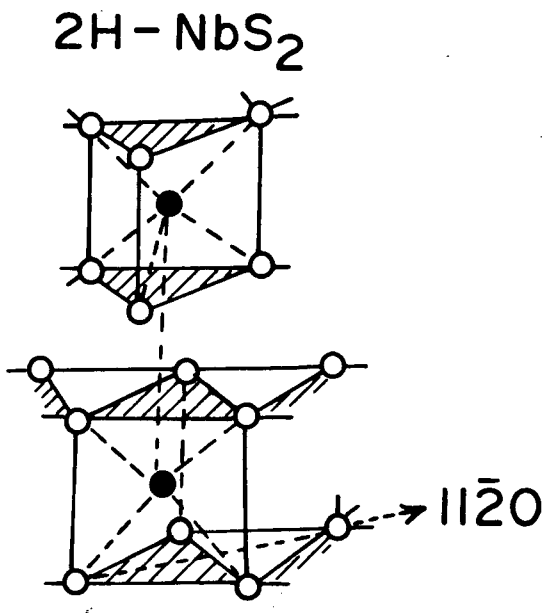

Figure 2: The structure of 2H-NbS_2. Black circles indicate niobium atoms and open cicles are sulfur. Intercalated lithium is believed to lie in the octahedral site halfway between the two niobium atoms. 3R-NbS_2 has layers of the same type, but a different interlayer stacking sequence.

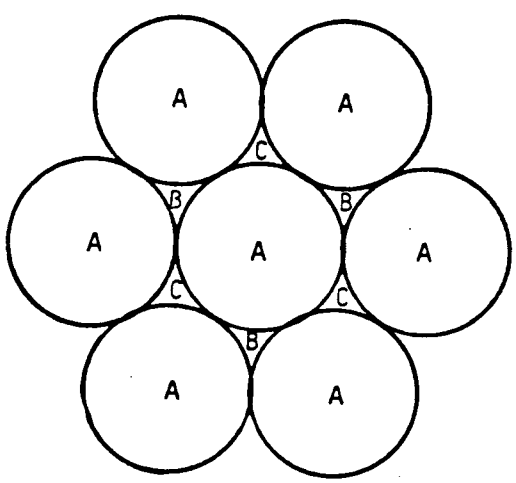

Figure 3: Definition of the letter notation for close-packed atomic planes.

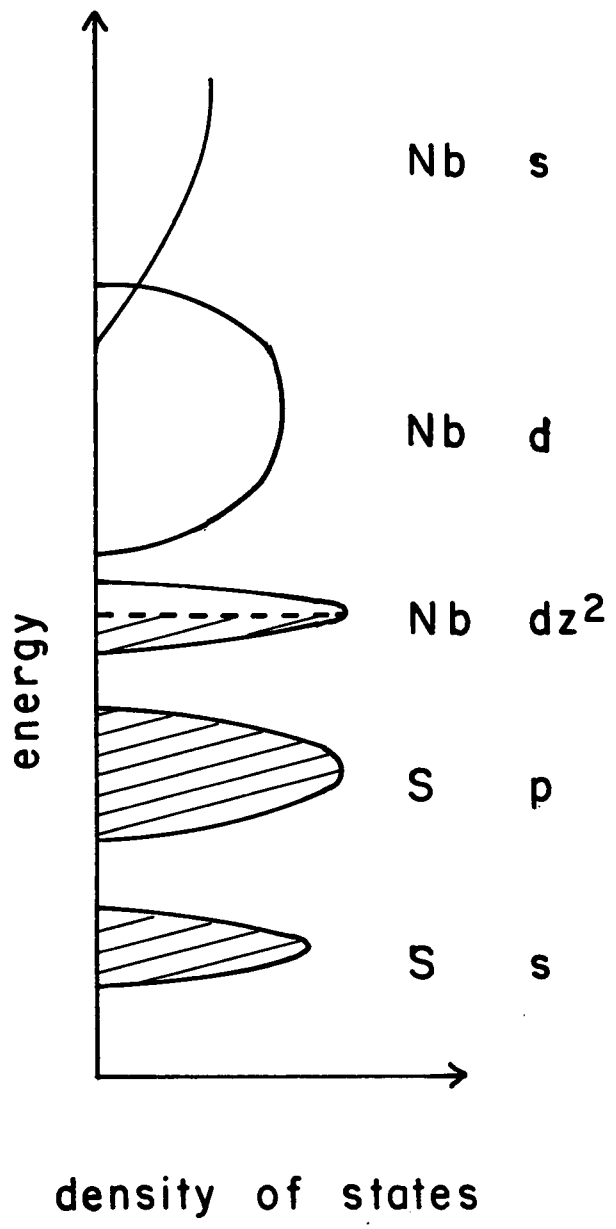

Figure 4: Schematic band structure of NbS_2.

the Fermi level lies in the middle of the half filled dz^2 band.

The properties of LTMDs and their intercalation compounds have frequently been discussed in terms of the rigid band charge transfer model (RBCT). This model assumes that:

1. The d bands at least are not affected very much by intercalation (rigid bands).
2. On intercalation of an alkali metal atom, its valence electron is donated to the lowest unoccupied state in the host bands (complete charge transfer). Other intercalated electron donors such as certain organic molecules exhibit incomplete charge transfer.

RBCT has been used extensively to explain the optical and electrical properties of intercalated LTMDs. The reviews by Marseglia (1983) and by Yoffe (1982), for example, discuss a number of experimental results from this point of view. Occasionally the predictions of RBCT fail; this is often due to intercalation induced changes in the s and p bands which can lead to overlap with the d band. Theoretical insight into the RBCT model has come from the calculations of McCanny (1979), and of Umrigar et al. (1983). In both these works, first principles band structure calculations for TiS_2 and Li_xTiS_2 are performed and compared. The calculated d bands are not significantly altered by intercalation, except by filling due to charge transfer. The sulfur 3s and 3p bands are, however, modified considerably, as is a

high-lying Ti 4s-like band. Although the tight-binding model of band structure is not accurate enough for calculations in the LTMDs, one can discuss the results in a tight-binding framework. From this point of view, the s and p bands are more strongly affected by intercalation because the atomic s and p states on which they are based are large in size, and extend significantly into the interlayer gap. (The sulfur p_z states extend farthest into the gap, and it is their overlap which is primarily responsible for interlayer bonding in the unintercalated LTMDs.) On intercalation, there is a large overlap of the s and p states with the Li 2s state. The metal atom d states, because of their smaller size, do not extend into the gap and are not affected.

From the above discussion, there is good reason to expect RBCT to be a valid way of understanding those electronic properties of intercalated LTMDs which depend primarily on electrons at or near the Fermi level (that is, in the d bands). One such property is the electronic contribution to the low temperature specific heat, and it was the possibility of making a quantitative test of the RBCT model in this way which motivated the work described in this thesis.

1.4 CONTRIBUTIONS OF THIS THESIS

Chapter 2 of this thesis is concerned with the preparation and characterization of NbS_2 and Li_xNbS_2. It will be shown that staged phases exist in Li_xNbS_2, as in Li_xNbSe_2

(D.C.Dahn and Haering 1982). This has not been realized by previous authors (McEwan and Sienko 1982, McEwan 1983).

Chapter 3 describes the low temperature heat capacity cryostat built for this work, and the procedures used for measurements and data analysis. The results for eleven Li_xNbS_2 samples covering the range 0 to 1 in x are given in chapter 4.

The specific heat of a normal metal at sufficiently low temperatures has the form (Ashcroft and Mermin 1976, for example)

$$c=\gamma T+\beta T^3 \qquad (1-4)$$

where γ and β are constants[2]. The first term in (1-4) is due to the electrons and is proportional to the density of states at the Fermi level. It can be separated from the cubic term by fitting the data to (1-4). In the RBCT model, as x is increased by intercalation, the Fermi level moves up through the host bands, and the variation of γ with x directly maps out the d band density of states. The interpretation of the electronic specific heat data in this fashion is discussed in chapter 5.

---

[2] Note that it has not been specified whether this is the specific heat at constant volume or constant pressure. Experimental evidence and thermodynamic arguments show that the difference between these is insignificant in solids, especially at low temperatures (Ashcroft and Mermin 1976, p427). Although we can ignore the difference between the two, the experimental data in this thesis were measured at constant pressure, while the theoretical expressions in chapters 5 and 6 are, strictly speaking, valid for constant volume.

The cubic term in the low temperature specific heat is due to lattice vibrations. The coefficient β of this phonon term also changes as a function of x, and some possible reasons for this are presented in chapter 6.

Chapter 7 is a brief discussion of superconductivity in Li_xNbS_2 and chapter 8 summarizes the thesis. Suggestions for future work are also given.

2. PREPARATION AND STRUCTURE OF INTERCALATED NIOBIUM DISULFIDE

2.1 PREPARATION OF NbS_2

The NbS_2 used in this work was prepared by reaction of the elements in evacuated quartz ampoules. The starting materials were 99.9% pure niobium powder and 99.9999% pure sulfur powder[3]. The niobium powder was reduced by heating it to 500°C in hydrogen.[4] After reduction the niobium was handled only in an argon atmosphere. Weighed amounts of niobium and sulfur were placed in quartz ampoules which were then evacuated using a diffusion pump, and sealed. Enough excess sulfur was added to produce approximately 6 atmospheres of sulfur gas pressure at the annealing temperature of 750°C[5]. The excess sulfur is required in order to get a stoichiometric product with the 2H structure

---

[3] Both from SPEX Industries, Metuchen, N.J.

[4] Hydrogen can be absorbed into Niobium to form a metal hydride. It has recently been learned that the reduction procedure that was used leaves a significant amount of hydrogen in the niobium metal. X-ray diffraction measurements of the niobium that was used to prepare NbS_2 batch DD12 indicated that it contained about 20 atomic percent hydrogen. (The lattice parameters of H_xNb are known as a function of x; see Schober and Wenzl 1978.) However, proton NMR measurements failed to detect any hydrogen in the NbS_2 that was produced from this material. When NbS_2 is prepared by high temperature reaction, the hydrogen may react with some of the excess sulfur present to form H_2S.

[5] The thermodynamic properties of sulfur vapour have been measured by Rau et al. (1973)

(Fisher and Sienko 1980). Typical ampoules had an interior volume of about 12cm^3, and contained about a 6g total charge, of which about .2g was excess sulfur. The ampoules were heated slowly to the reaction temperature of 950°C, left there for 2 to 3 days, then annealed at 750°C for one day. This was followed by a quench into cold water. The quench is necessary in order to obtain the 2H phase, and also neatly separates the excess sulfur from the NbS_2, since all the sulfur vapour condenses out on the cold walls of the ampoule during the quench. The product is a free flowing powder. Since the excess sulfur adheres to the walls, only the material which can be poured freely out of the ampoule when it is cracked open is used.

X-ray powder diffraction measurements were made on the NbS_2 powders. For the three batches of NbS_2 used in this work, the dimensions of the hexagonal unit cell are listed in table I. All these batches are pure 2H phase. No Bragg peaks corresponding to the 3R structure were seen. The lattice parameters were determined by a least squares fit to the positions of at least 8 Bragg peaks[6]. The three batches of NbS_2 have the same lattice parameters, within the accuracy of the measurements. The values depend to some extent on the details of the fitting procedure and the methods used to correct for diffractometer errors such as

---

[6]Using computer programs written by J.R.Dahn, P.Mulhern and the author.

the off-axis effect (J.R.Dahn et al. 1982). Estimates of these possible systematic errors have been included in the errors quoted in the table, and this is why the differences between the three a values, in particular, are less than the uncertainty in each one. Lattice parameters from the previous literature are also included in the table, and agree reasonably well with the present values.

As noted by previous authors (Jellinek et al. 1960, Revelli 1973, Fisher and Sienko 1980), some of the Bragg peaks are quite broad. For example, the (104) peak of DD9 NbS_2 has a width at half maximum of 1.3° in 2θ, where θ is the Bragg angle[7]. The broad peaks indicate some disorder in the crystals. The type of disorder can be deduced from the fact that all the lines with Miller indices $(hkl)=(00l)$ or $(11l)$ are sharp. It can be shown (Revelli 1973, for example) that these lines are not broadened if the disorder is due only to stacking faults. Stacking faults occur frequently in layered transition metal dichalcogenide crystals, and are, in this case, errors in the registry between adjacent S-Nb-S sandwiches. In terms of the letter notation of section 1.2, the sequence

...BaB-CaC-BaB-AbA-CbC...

has a stacking fault between the third and fourth layers.

---

[7]Diffractometer results are usually given in terms of 2θ rather than θ since the instrument actually measures 2θ.

Table I

Properties of 2H-NbS_2

Included are hexagonal lattice parameters a and c, superconducting transition temperature, T_c, and specific heat coefficients γ and β. Unless indicated otherwise, T_c was measured by a magnetic susceptibility method, and T_c taken as the temperature when the transition was 50% complete.

Reference	a (A)	c (A)	T_c(K)	range of T_c (K)	γ (mJ/mole-K^2)	β (mJ/mole-K^4)
This work:						
DD6	3.325	11.96				
DD9	3.323	11.96	5.7*	5.5-6.0	19.3±1.5	0.31±0.04
DD12	3.324	11.95				
	(±.005)	(±.01)				
Fisher and Sienko (1980)	3.324 (±.003)	11.95 (±.02)	6.33	6.25-6.41		
McEwan (1983)			6.46	0.41K wide		
Aoki et al (1983)			6.1†		18.2	0.33
Nakamura and Aoki (1983)			6.06†			
Revelli (1973)	3.31	11.90	6.1	5.5-6.6		
Van Maaren and Harland (1969)			5.5*		10.7	0.31
Van Marren and Schaeffer (1966)						
powders				5.8-6.2		
single crystals				6.1-6.3		
Molinie et al (1974)			6.23†			

† - onset temperature
* - measured calorimetrically

Superconducting transition temperatures for NbS_2 from the literature are also given in table I. There is considerable disagreement on the superconducting transition. The transitions are all rather broad. This has been explained by some authors (Van Maaren and Schaeffer 1966, Revelli 1973) in terms of variations in stoichiometry within the sample. Many LTMDs are known to have metal rich phases, which are essentially the stoichiometric phases with some excess metal intercalated between the layers. The assumption made is that the samples were actually 2H-$Nb_{1+y}S_2$, with slight variations y within each sample and between samples. The transition temperature is said to drop very rapidly with increasing y, in agreement with the rigid band charge transfer model, since intercalated excess Nb should donate electrons to the dz^2 band and hence lower the density of states at the Fermi level. Revelli (1973) stated that the transition drops by about 1.5K for each change in y of .01. Non-stoichiometry might be a satisfactory explanation of the variations of the transition temperature, except for the results of Fisher and Sienko (1980), which indicate that $Nb_{1+y}S_2$ exists only in the 3R structure, and that 3R-$Nb_{1+y}S_2$ is not a superconductor. Fisher and Sienko did not, however, offer an alternate explanation of the broad and variable transitions.

The superconducting properties of stoichiometric 3R-NbS_2 are also unclear. Jones et al. (1972) reported a transition at 5.9K, while Van Maaren and Schaeffer(1966) saw

a transition extending from 5.0 to 5.5K. Fisher and Sienko were not able to prepare stoichiometric 3R-NbS_2 and suggested that the earlier samples were all non-stoichiometric, and that the observed superconductivity was due to small amounts of 2H present as impurities. However, further work by the same group confirms that stoichiometric 3R-NbS_2 can be prepared, provided the reaction temperature is sufficiently low (McEwan 1983). McEwan found T_c=4.67K for the stoichiometric 3R phase.

Previous specific heat results for the 2H phase (table I) are also in disagreement. Although the values for β in

$$c=\gamma T+\beta T^3 \qquad (1-4)$$

agree, the value for γ given by Van Maaren and Harland (1969) is much smaller than that reported by Aoki et al.(1983). The specific heat of NbS_2 was measured during the course of the work leading to this thesis, and the results (section 4.3) are in agreement with those of Aoki et al. The differences in γ values may be due to the methods used to fit the data to equation (1-4). Equation (1-4) is only valid in the normal state. As will be discussed in section 4.3, however, the normal state data alone are not sufficient to determine γ accurately. It is possible to use the specific heat data in the superconducting state to derive an extra constraint on the fit, and only if this is done can the parameters in (1-4) be determined accurately.

2.2 PREPARATION OF Li_xNbS_2

To prepare Li_xNbS_2, lithium was intercalated into NbS_2 in electrochemical cells. The cell cathodes (positive electrodes) were prepared by fixing NbS_2 powder to a nickel foil substrate using the following procedure. First, the nickel foil substrates were etched in nitric acid to clean and roughen them. They were then thoroughly rinsed and dryed. NbS_2 was ground using a mortar and pestle, until it passed through a 400 mesh (38μm) sieve. The powder was then mixed with cyclohexane to form a thick slurry, which was spread evenly over the substrates. After the cyclohexane evaporated, the cathodes were passed between two steel rollers, which compact the NbS_2 layer, thereby improving the electrical contact between the NbS_2 grains, and between the NbS_2 and the substrate. Inserting a sheet of weighing paper between the cathode and the upper roller helps to prevent the NbS_2 from sticking to the roller. The mass of NbS_2 on the cathodes was established by weighing the bare substrates and the finished cathodes. Cathodes used for preparation of low temperature specific heat samples were 1.75 inches in diameter, and contained typically 0.3g of NbS_2. Similar but smaller cathodes containing 10 to 20 mg of NbS_2 were used in cells intended for the electrochemical measurements to be described later in this chapter.

Anodes for the cells were lithium metal foil[8]. The

---

[8]From Foote Minerals, Exton, Pa.

cells were assembled in an argon filled glovebox. They were of the flange cell type (figure 5). Cells were assembled by placing a porous polypropylene film separator[9] between the anode and cathode. The separators were wet with an electrolyte consisting of a 1 molar solution of $LiAsF_6$[10] in propylene carbonate. The active components of the cells were sandwiched between stainless steel flanges, which were separated by Viton rubber o-rings. The o-rings served to provide airtight seals for the cells, as well as electrically isolating the flanges. The anode and cathode are each in electrical contact with one of the flanges, so that electrical connection to the cell is accomplished by simply connecting a lead to each flange. Li_xNbS_2 samples for low temperature specific heat measurements were made by discharging flange cells to a preset voltage using a Princeton Applied Research model 173 Potentiostat/Galvanostat. The current which passed through the cell during discharge was integrated by a PAR model 179 digital coulometer. Since for each Li^+ ion which moves from anode to cathode during the discharge, one electron moves through the external circuit, the value of x in the Li_xNbS_2 samples could be calculated using

$$x = \frac{QM}{m\ (96{,}500\ \text{Coul/mole})} \qquad (2\text{-}1)$$

---

[9]Celanese Plastics Celgard #2500 or 3501

[10]U.S.Steel Agrichemicals, 'Lectrosalt' brand.

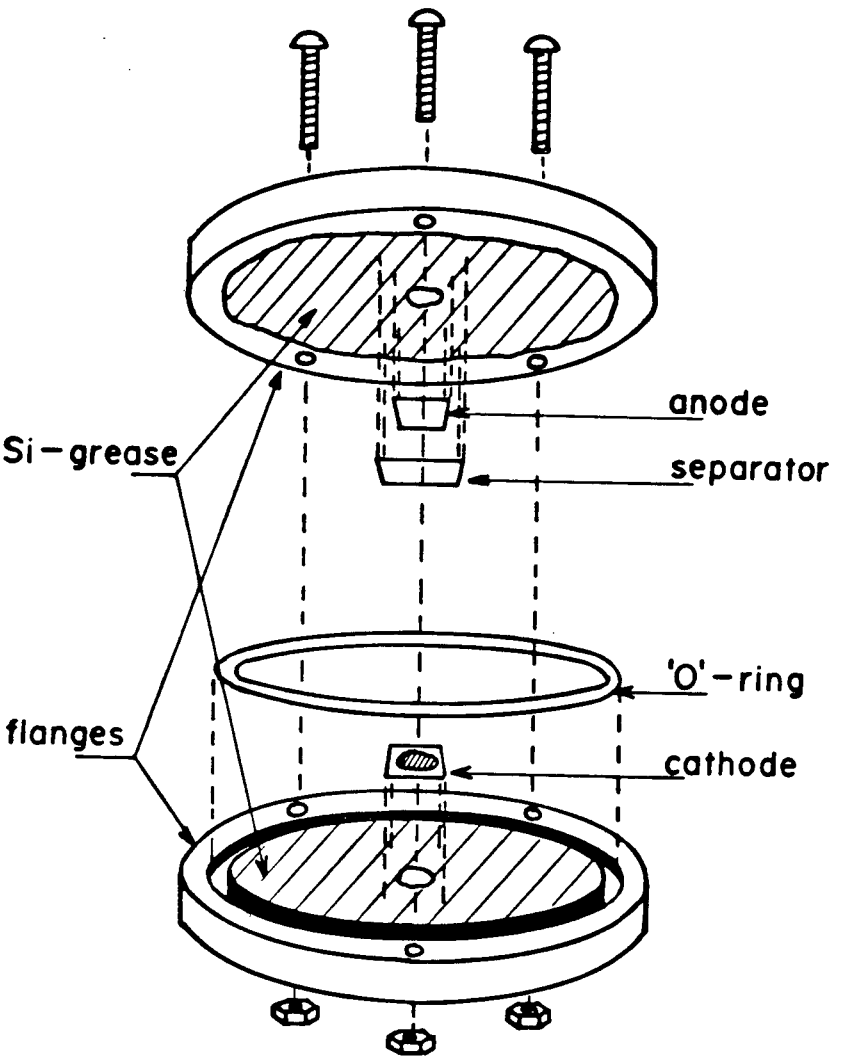

Figure 5: A typical flange cell.

where Q is the charge which has passed through the cell, M is the molecular weight of NbS_2 (157.0g/mole), and m is the mass of NbS_2 on the cathode.

In order to have a uniformly intercalated sample, a cell must be allowed to fully equilibrate. When a freshly prepared cell (x=0, open circuit voltage $\simeq$ 3.2V) is connected to a fixed voltage V_0 such as that provided by the PAR 173, current should flow until the cathode material is uniformly intercalated to a composition given by

$$V_0=V(x)=(\mu_a-\mu_c(x))/e \qquad (2-2)$$

(see equation 1-3). The equilibration of actual cells is not quite this simple, since the approach to equilibrium can be rather slow, and at some point as the intercalation current slowly dies away, spurious changes in Q due to coulometer drift and cell leakage currents may become significant. A useful way of monitoring an equilibration is to make a plot of current as a function of Q, or equivalently, x as determined from (2-1). This was done during the equilibrations of the sample preparation cells. The plots of current against x exhibited an almost linear appearance as the current approached zero. This sort of behavior is not surprising, since at least near equilibrium it is reasonable to expect the current to be proportional to the deviation from equilibrium. Discharges were stopped by observing this limiting behavior and disconnecting the cell only when x had come within about 1% of the apparent limiting value. The times required for this were usually 5 to 10 days, and the

final currents were always less than 5μA. Cells were generally not left on the PAR 173 for more than 10 days, in order to minimize the effects of drift and leakage currents.

One of the problems that has been associated with electrointercalation in the past is cathode utilization. Often some of the cathode particles are not in good electrical contact with the substrate, and consequently cannot be intercalated. This was seen, for example, in the author's previous work on Li_xNbSe_2 (D.C.Dahn and Haering 1982) The cathodes used in that study were not rolled, however, and the addition of the rolling step in the cathode preparation procedure appears to have eliminated all problems with cathode utilization. X-ray diffraction on Li_xNbS_2 prepared using rolled cathodes consistently shows no trace of Bragg peaks due to unintercalated material. Because of this, the uncertainty in x is determined primarily by cell leakage currents, coulometer drift, and possibly by side reactions in the cell. The magnitude of these effects is not easy to estimate accurately, but is believed to be a few percent of x.

The next step in the preparation of a specific heat sample was to take an equilibrated cell back into the argon glovebox, open it, and scrape the intercalated cathode material off the substrate. To remove the electrolyte which remained on the surfaces of the Li_xNbS_2 grains, they were rinsed with pure propylene carbonate and dried in vacuum. The propylene carbonate used was specially distilled and

contained about 10 to 20 parts per million of water. This was the same material used in the preparation of electrolyte. About 1ml was used for the rinse.

After drying, some of the Li_xNbS_2 powder was pressed into a pellet for use as a specific heat sample. The pressing was done in a steel piston die which forms a pellet 6mm in diameter and a few mm high. The force required to form a pellet is of order 1000N and is applied with a c-clamp. The pellet was then weighed and mounted in the cryostat as described in chapter 3. The remaining Li_xNbS_2 powder could be used for x-ray diffraction. All handling of the Li_xNbS_2 samples took place in an argon atmosphere.

2.3 THE STRUCTURE OF Li_xNbS_2

X-ray diffraction and electrochemical measurements have been used to determine the crystal structures and approximate phase boundaries of the Li_xNbS_2 phases formed by intercalation at room temperature. For $x \geq .23$, Li_xNbS_2 has a stage 1 structure, that is, there is an equal concentration of lithium in each interlayer gap. For x between (roughly) .11 and .19 there is a well-ordered stage 2 structure. In stage 2, every second gap contains lithium, and the intervening gaps are either empty or nearly so. There is evidence for a disordered stage 3 phase (lithium in every third layer on average but with no long range order in the staging sequence), which exists for compositions near x=.08. Samples with average compositions between those of the

staged phases are phase mixtures. The staging behavior is similar to that observed in Li_xNbSe_2 (D.C.Dahn and Haering 1982).

An especially powerful way of observing the staging phase transitions is the use of electrochemical cells with beryllium x-ray windows (J.R.Dahn et al. 1982). These cells are similar in construction to the flange cells described in the previous section. The NbS_2 powder, instead of being fixed to a nickel substrate, is fixed directly to the inner surface of a .25mm thick beryllium foil window which is set into one of the flanges. To keep preferred orientation of the cathode powder to a minimum, x-ray cell cathodes are not rolled. Ideally, it would be best to have completely random orientation of the cathode particles, since this simplifies interpretation of powder diffraction measurements. However the NbS_2 particles are thin platelets with their crystallographic c-axis normal to the flat faces. Because of their shape, they tend to settle with their c-axis normal to the substrate to which they are attached. With rolling, this orientation is enhanced to the point where only (00*l*) Bragg peaks can be seen.

Figure 6 shows portions of diffractometer scans made while an x-ray cell was slowly equilibrating to a final voltage of 2.760V. The region around the (008) Bragg peak is shown in the figure, although complete scans from 10 to 90° 2θ were made in each case. Only NbS_2 peaks were seen in the first scan, made before the discharge started. As

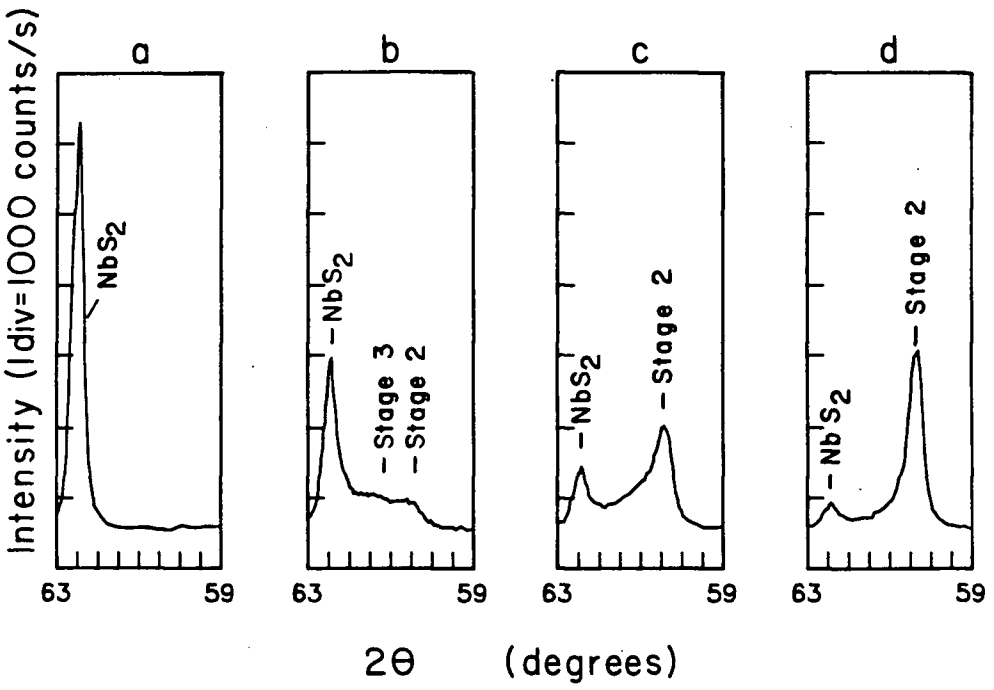

Figure 6: The (008) region during the discharge of a Li/Li_xNbS_2 x-ray cell to 2.760V.

a- Before discharge (x=0)

b- After 3 days (x=.06)

c- After 6 days (x=.08)

d- After 15 days (x=.14). At this point intercalation was essentially complete. The remaining intensity in the NbS_2 peak is due to material which was not electrically connected to the substrate.

intercalation proceeded, these peaks shrank. They did not disappear completely, because of incomplete cathode utilization. At the end of the equilibration the cathode (except for the non-utilized fraction) was in the stage 2 phase. A third set of peaks, corresponding to what is believed to be a disordered stage 3 phase, was seen during the intercalation process. This occured because while going from NbS_2 to stage 2, it is necessary to pass through stage 3 as an intermediate state. During the intercalation process in this cell, each cathode particle had NbS_2 at the center, surrounded by a region of stage 3, surrounded in turn by a region of stage 2 at the surface. Intercalation apparently proceeded by both phase boundaries propagating into the center.

That the phase between $x \simeq .11$ and .19 is truly stage 2 can be seen from the presence of a (009) Bragg peak. In pristine 2H-NbS_2 and in the stage 1 intercalation compound, (00*l*) Bragg peaks with *l* odd are all extinct. This happens because of a symmetry of the two layer high unit cell which causes the geometrical structure factor for these lines to be zero. In the stage 2 compound, only one of the two interlayer gaps in the unit cell contains lithium and is expanded. The two layers in the unit cell are no longer equally spaced along the c-axis, and (00*l*) peaks with *l* odd are allowed. Note that staging is observed primarily through the distortion of the host lattice due to the fact that intercalated gaps expand, as the scattering power of lithium

is very small. Although of the (00*l*) peaks with *l* odd, only (009) is observed, intensity calculations (Appendix 1) show that the (003), (005), and (00$\underline{11}$) peaks are weak. The (001) peak has a scattering angle which is too small for it to be detectable in the x-ray cell configuration. The (007) peak should be observable, but unfortunately a beryllium Bragg peak originating in the window interferes with it.

The stage 1 and 2 phases both appear to have the same structure as 2H-NbS_2, except for the addition of the lithium and the resultant expansion of the interlayer gaps. This is an important point, since McEwan (1983) and McEwan and Sienko (1982) report that Li_xNbS_2 prepared by direct high temperature reaction of the elements forms in the 3R phase or in a 2H-3R phase mixture for x between .01 and .13. Apparently, doing the intercalation at room temperature avoids this. Another comment on McEwan and Sienko's work should be made here. Although they state that all their samples were stage 1, they report the presence of (007) and (009) Bragg peaks in 2H-Li_xNbS_2 for x between .13 and .17. McEwan (1983) surmises that the (007) peak may be due to a superlattice of period $7c_o$ along the c-axis. This is clearly an incorrect explanation, since such a superlattice would produce (0,0,1/7) and related peaks, rather than a (007) peak. The most likely explanation is that McEwan and Sienko's samples were stage 2 between x=.13 and .17.

The dimensions a and c of the unit cell are shown as a function of x in figure 7. Accurate values of c and a could

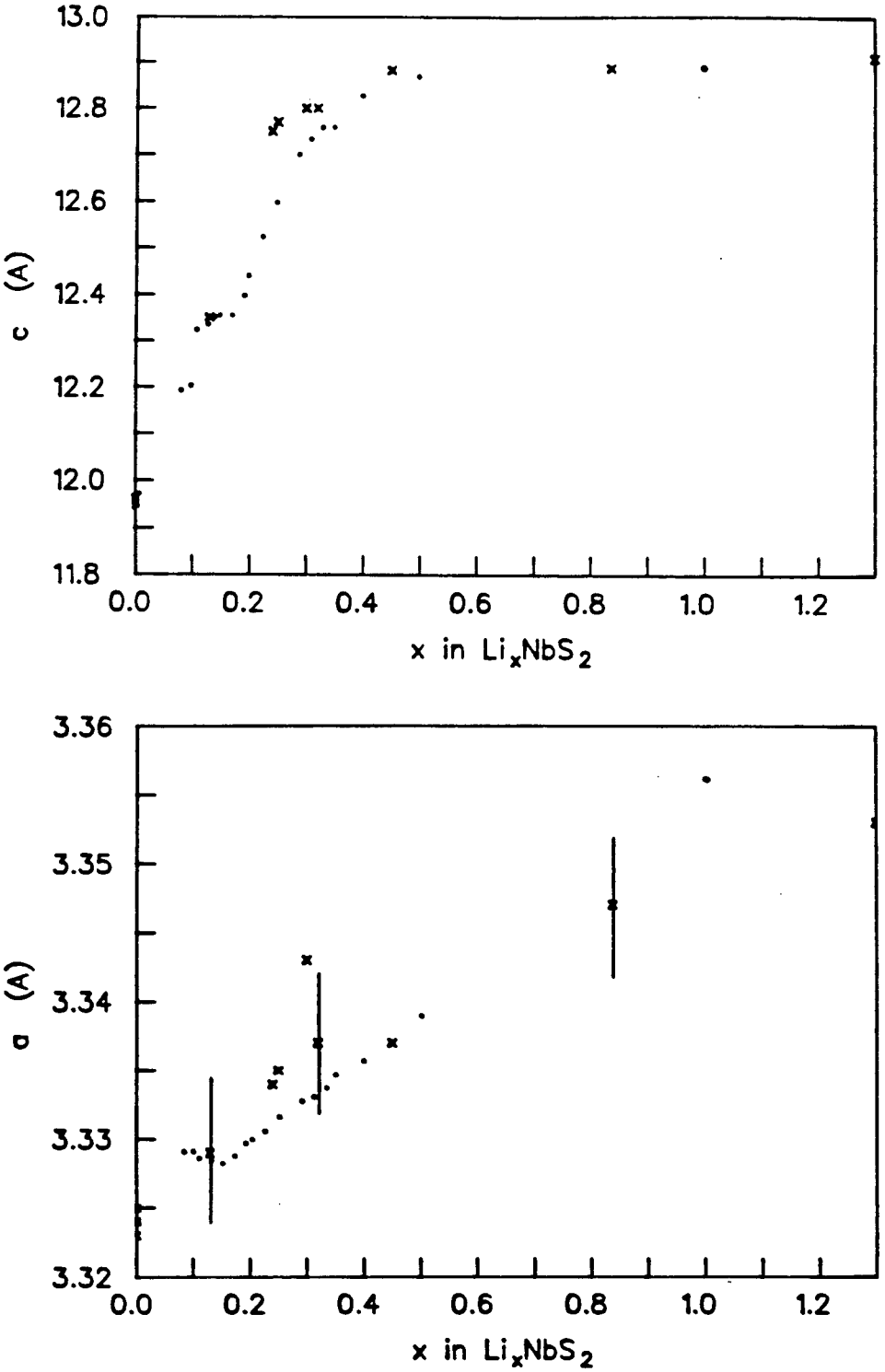

Figure 7: Hexagonal lattice parameters a and c for Li_xNbS_2. The crosses represent data from this work, and the points are from McEwan (1983).

not be obtained for the stage 3 phase, since it has so far only been observed as an intermediate state during intercalation from NbS_2 to stage 2. An approximate value for c in the stage 3 phase is 12.2Å.

Also shown in figure 7 are the lattice parameters of McEwan and Sienko's high temperature prepared Li_xNbS_2. The precision of the data is good because Li_xNbS_2 prepared at high temperature has very sharp Bragg peaks, indicating fewer stacking faults than in Li_xNbS_2 prepared by room temperature intercalation. Only those samples which were 2H, or where 2H was the major component of a 2H-3R phase mixture, are included. Plateaus at the stage 3 and stage 2 compositions can be seen in the c-axis data. Note that the c values for $x>.2$ are lower than the results from this work. McEwan and Sienko prepared their samples by reaction in evacuated quartz tubes, and some of the lithium was lost due to reaction with the quartz.[11] The amount of tube attack increased as a function of lithium concentration (McEwan 1983). As a result, the x values quoted by McEwan and Sienko are too high, and the error in x increases as a function of x. Comparison of the c data shows, for example, that McEwan and Sienko's 'x=.33' sample actually had a composition near x=.25.

---

[11] Similar tube attack by lithium has been observed in the course of high temerature compound preparation in this laboratory (J.R.Dahn and P.J.Mulhern, unpublished).

Further information on the phase transitions in Li_xNbS_2 was obtained from electrochemical measurements. As mentioned in chapter 1, the voltage of a Li/Li_xNbS_2 cell can be used to study the thermodynamics of the intercalation compound, since

$$V(x)=(\mu_a-\mu_c(x))/e$$

where μ_a and μ_c are the chemical potentials of lithium in lithium metal and in the intercalation compound, respectively. Only a brief discussion of the interpretation of electrochemical measurements will be required here; for more complete discussions see Johnson (1982) or J.R.Dahn and McKinnon (1984a). As the value of x in a cell cathode is increased by intercalation, the cathode is sometimes observed to undergo a first order phase transition between two compositions, say x_1 and x_2. During the transition the average composition x is given by

$$x=f_1x_1+(1-f_1)x_2 \qquad (2-3)$$

where f_1 and $(1-f_1)$ are the fractions of the sample in the x_1 and x_2 phases, respectively. Regions of constant voltage V in a cell's V(x) curve are the signatures of such phase transitions, since as long as the sample is a phase mixture μ_c is constant and therefore V is constant. These features in V(x) curves may be detected more easily by numerically calculating the inverse time derivative dt/dV during a slow constant current charge or discharge of the cell. This is because (ignoring kinetic effects due to lithium diffusion gradients in the cathode and the internal impedence of the

cell)

$$dt/dV = (Q_1/i)(dx/dV) \qquad (2\text{-}4)$$

where i is the cell current (positive on discharge) and Q_1 is the amount of charge corresponding to a change in x of 1. Phase transitions will therefore produce sharp peaks in dt/dV. The peaks are not infinitely high because of the lithium diffusion gradients mentioned above.

V(x) data for Li/Li_xNbS_2 are shown in figure 8. Because of incomplete cathode utilization (91% utilization) in the small flange cell used, the data have been scaled so that x=1 occurs at 1.90V. Also included are the V(x) data from specific heat sample preparations. The results are in agreement with less accurate previous measurements (Holleck et al. 1975, DiPietro et al. 1982). Using a microcomputer based instrument which calculates dt/dV during a constant current discharge or charge, dt/dV measurements were made on several cells. Typical results are shown in figure 9. The data are shown in terms of -dx/dV (equation 2-4) The staging phase transitions are clearly seen. The higher peak at about 2.74V is due to the stage 2 to stage 1 transition. A smaller broader peak at about 2.78V is seen on the first recharge and second discharge. This is believed to be due to the stage 2 to stage 3 transition. As can be seen from figure 8, Li/Li_xNbS_2 cells cannot be recharged all the way back to x=0 in the Li_xNbS_2 cathode. This is the reason that the first discharge curve in figure 9 is different than the other two. The area under the -dx/dV curve at voltages above the stage

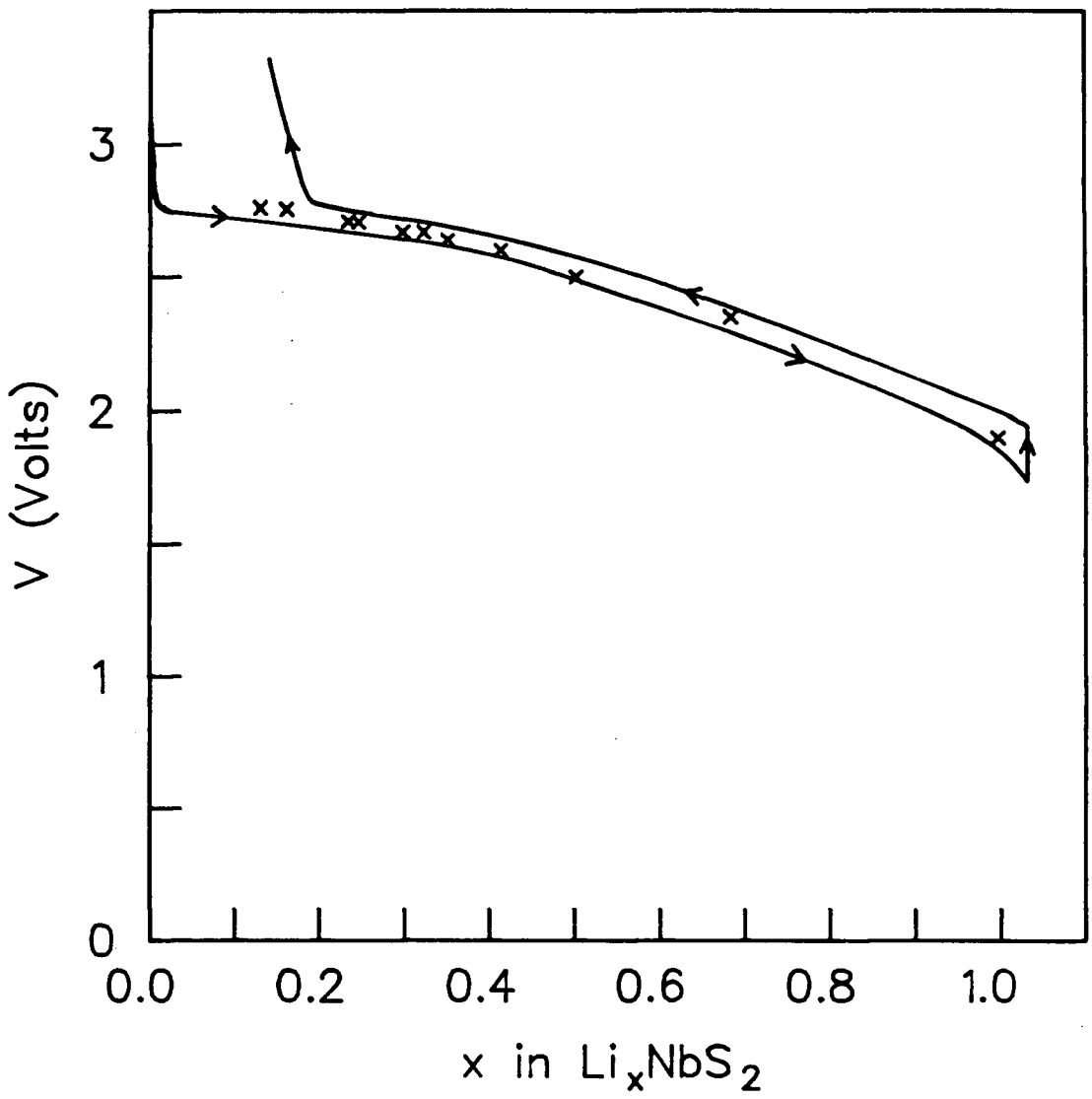

Figure 8: Cell voltage as a function of x for Li_xNbS_2. The lines show the first discharge and the subsequent first charge of cell DD65. The discharge and charge were both at a rate of $\Delta x=1$ in 60 hours. Also shown (x) are the V(x) values of the specific heat samples.

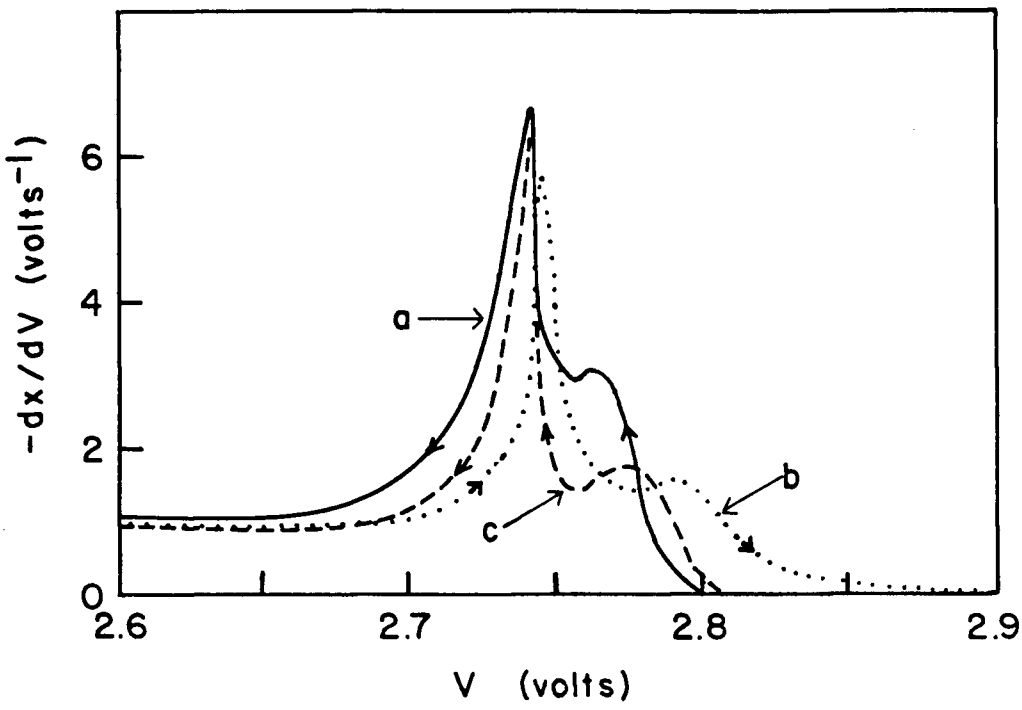

Figure 9: -dx/dV data for Li/Li$_x$NbS$_2$ cell DD45, showing the staging transitions.

a- First discharge

b- First recharge

c- Second discharge.

2 - stage 1 peak is larger for the first discharge than for subsequent charges or discharges. (The area under a -dx/dV curve between two voltages is the change in x between those voltages.) This presumably happens because of some kinetic barrier which prevents de-intercalation of the stage 3 phase. Similar behavior has been observed in the Li_xNbSe_2 system, where the presence of residual lithium in fully charged cathodes has also been verified directly by x-ray diffraction (D.C.Dahn and Haering 1982), as well as in the intercalated graphite 'residue compounds'. There is also apparently some kinetic or nucleation barrier at the very beginning of the intercalation process. Since the x-ray results clearly show a succession of three transitions (NbS_2 to stage 3, stage 3 to stage 2, and stage 2 to stage 1), there should, in principle, be three peaks in -dx/dV on the first discharge. There are, however, only two. For some reason, the first intercalation can only proceed (at a rate of $\Delta x=1$ in about 200 hours in this case) when the cell voltage has already dropped into the stage 2 region. The kinetics of the staging transitions in Li_xNbS_2, Li_xNbSe_2, and related materials might be an interesting topic for more detailed study in the future.

An additional feature in -dx/dV was observed in two cells made using freshly prepared NbS_2 from batch DD12. Two small peaks near 2.67V ($x\simeq.3$) could be seen (figure 10). The cells which showed this feature were assembled 14 days and 28 days after batch DD12 was prepared and ground. Also shown

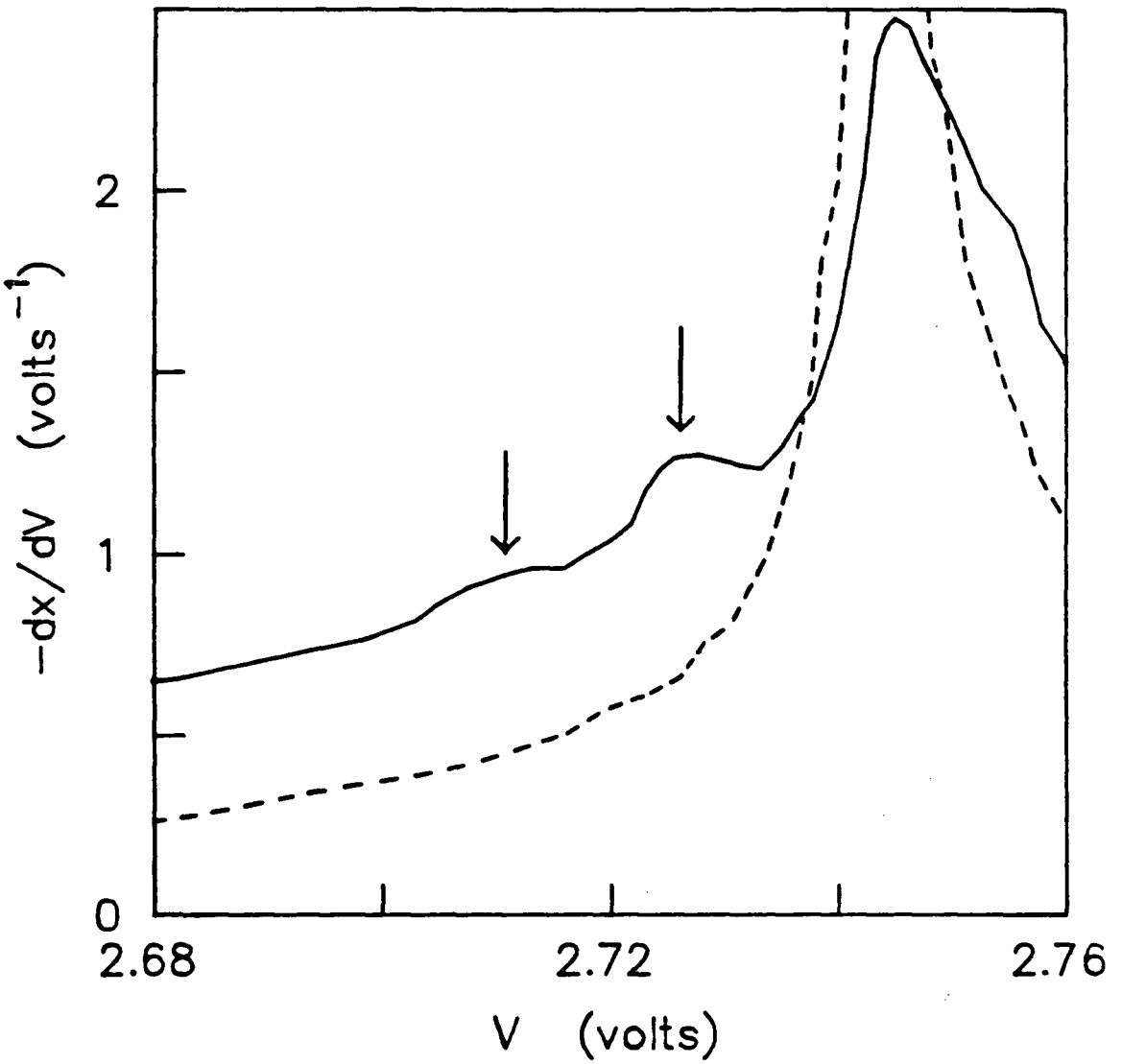

Figure 10: -dx/dV data on Li/Li$_x$NbS$_2$ cells, showing the aging effect. The solid line is data from a cell made with freshly prepared NbS$_2$ from batch DD12, and the dashed line with aged NbS$_2$ from the same batch. The dashed line has been displaced downward by .5 V^{-1} for clarity. The arrows indicate the extra peaks mentioned in the text.

in the figure is data from a cell after it was made from DD12 NbS_2 which had been stored in a closed vial for 177 days. The extra peaks are not seen in this data. The extra peaks in -dx/dV were never observed in the other batches of NbS_2; however, dx/dV runs were not made on these batches until they were a few months old.

The extra peaks are similar to those due to lithium ordering on a $\sqrt{3}a$ triangular superlattice at x=1/3 in Li_xTaS_2 (J.R.Dahn and McKinnon 1984). The same type of lithium ordering may be involved here.

A possible reason for the disappearance of the extra peaks in 'old' material is loss of sulfur. There is evidence that NbS_2 slowly gives off sulfur; it smells faintly of H_2S when it is in air, and smells very strongly when being ground[12]. The smell presumably comes from sulfur lost by the NbS_2, which then reacts with moisture in the air. Aging effects have also been observed by Dutcher(1985) in TaS_2. He found that the intensities of x-ray Bragg peaks due to the charge density wave changed as a function of time and storage conditions, and also believes that sulfur loss is the cause.

If sulfur is lost from NbS_2, we are left with excess Nb, which would intercalate into the interlayer gaps. The presence of randomly placed niobium in the gaps could serve

---

[12] Loss of sulfur during grinding is not the explanation for the extra peaks in -dx/dV, since all the cells were made using ground material.

to inhibit lithium ordering. The amount of sulfur lost is not known, but it must be rather small since no significant changes in the lattice parameters were observed. Crystallographic data on $2H\text{-}Nb_{1+y}S_2$ for small y are not available, but Huisman et al. (1970) have measured the lattice parameters of $2H\text{-}Nb_{1+y}Se_2$. If the behavior of $2H\text{-}Nb_{1+y}S_2$ is similar, the fact that no changes in the lattice parameters were observed means that changes in y were about .01 or less.

3. THE LOW TEMPERATURE SPECIFIC HEAT EXPERIMENT

3.1 INTRODUCTION

This chapter begins with a brief review of the various experimental methods used for specific heat measurements at low temperatures. The reasons for choosing the relaxation time method for this work are given. There follows a discussion of the cryostat used, the measurement and control of the reference block temperature, and the sample temperature. The measurement cycle and data analysis are then discussed in detail.

3.2 TECHNIQUES FOR LOW TEMPERATURE SPECIFIC HEAT MEASUREMENTS

3.2.1 ADIABATIC CALORIMETERS

Although some low temperature calorimetry on solids was done late in the last century, it was not until the work of Nernst, Eucken, and their collaborators beginning in 1909 that satisfactory results over a wide range of low temperatures were obtained. (For a review of early work see Partington 1952.) The 'adiabatic calorimeter' first used by Nernst is, with improvements, still in wide use today. In its simplest form, an abiabatic calorimeter consists of a vacuum chamber immersed in a low temperature bath and containing the sample, which is suspended on supports having very low

thermal conductance . A thermometer and resistance heater are mounted on the sample; here again care is taken to minimize the thermal link between the sample and the bath through the leads. To make a measurement the sample is first cooled by the introduction of exchange gas. This is then pumped out, leaving the sample (approximately) thermally isolated. A pulse of heat Q is then applied to the heater, causing the temperature of the sample to rise by an amount ΔT. The heat capacity of the sample, thermometer, and heater assembly is then given by

$$C=Q/\Delta T \qquad (3-1)$$

The pulsed heating is then repeated, providing measurements of C at successively higher temperatures.

Improvements since Nernst's day (Gmelin 1979, for example) include better thermometry, the introduction of a temperature-regulated radiation shield around the sample, and computer data aquisition. Since large amounts of exchange gas can be adsorbed on the sample, especially if it is powdered or porous, and since the removal of exchange gas typically requires several hours of pumping, many modern adiabatic calorimeters are equipped with a mechanical heat switch for cooling the sample.

Abiabatic and related methods still provide the most accurate results on large samples (mass a few grams) at temperatures above 1K. The absolute accuracy

can be better than 0.5% (Gmelin 1979). The large samples are required so that the inevitable heat leaks along thermometer leads, etc, have an acceptably small effect on the sample temperature. Below 1K, frictional heating by the heat switch is a serious problem.

A variation on the adiabatic method is the quasi-adiabatic heat pulse method. Here the thermal link between the sample and the regulated radiation shield or reference block is made large enough so that after a heat pulse the sample cools again in a reasonable time, typically a few minutes. This eliminates the need for a thermal switch or exchange gas. As long as the cooling time is very long compared to the duration of the heat pulse, the maximum ΔT after a heat pulse will still be given to high accuracy by (3-1). In some cases, corrections must be made to account for the heat lost down the thermal link during the heating pulse (Sellers and Anderson 1974, Fagaly and Bohn 1977). When the sample's thermal conductivity is low, the sample may not be isothermal immediately after the pulse. As long as the internal relaxation time of the sample is short compared to the sample to reference block cooling time, internal relaxation effects may also be corrected for (Lasjaunias et al. 1977).

3.2.2 THE AC TEMPERATURE METHOD

Sullivan and Seidel (1968) introduced a new method of low temperature heat capacity measurement. In this method, the sample is connected to a temperature regulated block by a thermal link of thermal conductance k. A heater and thermometer are attached to the sample. An AC heater current at frequency $\omega/2$ is applied to the heater, and produces an AC temperature in the sample at frequency ω. In the simplest case, the AC temperature is given by

$$\Delta T_{ac}=P_{ac}/2\omega C \qquad (3\text{-}2)$$

where P_{ac} is the heater power and C is the total heat capacity of the sample and its addenda (heater, thermometer, supports, etc.) For (3-2) to be valid, the internal thermal response times τ_{int} of the thermometer and heater must be very short compared to $1/\omega$, the sample-to-block thermal relaxation time $\tau=C/k$ must be much longer than $1/\omega$, and the sample's thermal conductivity must be sufficiently high. If these conditions are not met, the analysis becomes more complicated (Sullivan and Seidel 1968), but in principle the method can still be applied. The greatest difficulties arise when the sample has a low thermal conductivity. In this case (assuming again that $\tau_{int}<<1/\omega<<\tau$), we have, for heater and thermometer on

opposite sides of the sample

$$\Delta T_{ac} = \frac{P_{ac}}{2\omega C} (1+2k/3k_s) \qquad (3\text{-}3)$$

where k_s is the thermal conductance across the sample. The frequency independent correction factor in (3-3) means that in order to make measurements of high absolute accuracy, we need either to have k/k_s small, or to make an accurate independent measurement of k and k_s. It is therefore difficult to make accurate measurements using the AC method, on samples with low thermal conductivity. The Li_xNbS_2 samples used in this work were pellets of compacted powder and were very poor conductors of heat.

The main advantages of the AC method are that it can be used with very small samples (<1mg mass) and that it can be used to give a continuous readout of C (via a lock-in amplifier) as the temperature and other parameters such as magnetic field are varied. The continuous nature of the measurement makes it the method of choice in studies were high precision but not necessarily high absolute accuracy is needed.

3.2.3 THE RELAXATION TIME METHOD

The relaxation time method was introduced by Bachmann et al. (1973), and is also discussed in the review by Stewart (1983). A simplified apparatus is shown in figure 11. The sample is attached to a platform

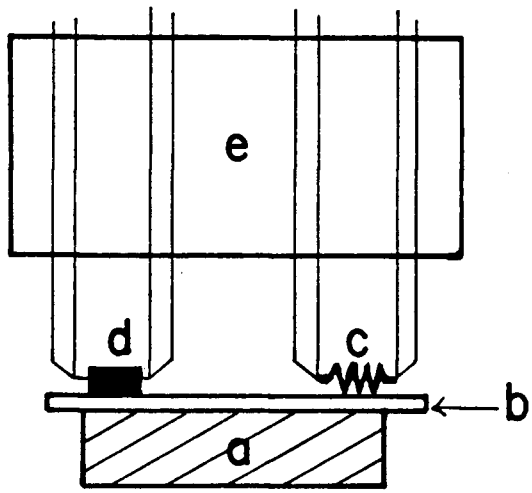

Figure 11: Schematic diagram of an apparatus for relaxation time heat capacity measurements.

a- Sample

b- Sample platform

c- Heater

d- Thermometer

e- Temperature regulated block.

The platform is supported by the heater and thermometer wires, which make thermal contact to the block.

such as a sapphire slide, to which are connected a heater and thermometer. The sample platform is suspended from a temperature regulated reference block by means of the heater and thermometer leads. These wires are thermally anchored to the block, and provide a thermal conductance k_w between the platform and the block.

A measurement begins with the sample and platform at the block temperature T_0. A DC current is then applied to the heater, producing power P. The temperature difference θ between the sample and block then rises, eventually reaching a constant maximum value θ_0 given by

$$\theta_0 = P/k_w \tag{3-4}$$

The heater current is then turned off. Assuming the sample's thermal conductivity is high and there is no thermal resistance at the boundary between the sample and the platform, the sample and platform will have a uniform temperature T_s as they cool. This will relax back to T_0 according to

$$k_w(T_s - T_0) = -C(dT_s/dt) \tag{3-5}$$

or;

$$T_s - T_0 = \theta_0 e^{-t/\tau} \tag{3-6}$$

where C is the total heat capacity of the sample and platform and $\tau = C/k_w$ is the relaxation time. Measurement of τ, θ_0, and P is sufficient to determine C, since

$$C = \tau k_w = \tau P/\theta_0 \tag{3-7}$$

When the sample's thermal conductance k_s is not infinite, the sample is not isothermal during cooling and (3-5) to (3-7) no longer hold. It is, however, possible to determine k_s from the decay data. A fairly straightforward calculation then determines C. The data analysis in the presence of a finite k_s is discussed in Bachmann et al. (1973), and later in this thesis (section 3.4 and Appendix 2). The specific heat can be determined with reasonable accuracy when k_s is of order k_w or greater. This condition is much less restrictive than the corresponding one for the AC temperature method, making the relaxation time method more suitable for samples of low thermal conductivity.

To avoid confusion, it should be pointed out that some authors (for example Fagaly and Bohn 1977) use the term 'relaxation time method' to describe a form of the quasi-adiabatic method discussed in section 3.2.1. A measurement of the exponential relaxation time after a short heat pulse can be used to extrapolate the sample temperature back to the time of the pulse. A relaxation time measurement, as the term is used by Bachmann et al. and in this thesis, should involve a measurement of both τ and k_w.

3.2.4 DISCUSSION

For the specific heat measurements described in this thesis, the relaxation time method was used, since

it allows accurate measurements on small samples of low thermal conductivity. Since the Li_xNbS_2 samples were pellets of pressed powder, their thermal conductivity was quite small (see section 3.4.2). As we have seen, the AC temperature method is not suitable for such samples. Samples of about 150mg mass can easily be prepared in electrochemical cells. Although samples of this size are quite adequate for a relaxation time measurement, it would be difficult to reduce the heat leaks through the heater and thermometer leads enough to allow adiabatic or heat-pulse method measurements, at least at temperatures below about 10K.

At higher temperatures, such as 15K and above, the relaxation times become much longer, typically of order 100s with the present cryostat and sample sizes. At 4K, decay times are typically 10s. This happens because the sample's heat capacity increases rapidly as the temperature is raised, as does k_s, the sample's thermal conductivity. Because of this, the present system could be run in a quasi-adiabatic heat pulse mode at higher temperatures. If it is ever desirable to make extensive measurements at temperatures above 15K, a slight modification of the computer software controlling the experiment would allow this, and permit measurements to be made more quickly than with the present relaxation time method. The present method is rather slow at high T, since one must wait several relaxation times with the

sample heater on in order to get a stable maximum sample temperature.

3.3 THE SPECIFIC HEAT CRYOSTAT

3.3.1 GENERAL FEATURES

The specific heat cryostat is of standard design, except for provisions to allow the mounting of air-sensitive samples. Figure 12 is a simplified drawing of the cryostat, showing its important features. The vacuum can is supported inside a ^{4}He bath by its pumping line. Inside the can is a copper temperature regulated block which supports the sample platform. The cryostat is designed to allow samples to be mounted inside an argon filled glovebox. Since the airlock used to tranfer articles in and out of the glovebox cannot accomodate the entire cryostat, the vacuum can may be detached from the pumping line. Samples are mounted in the glovebox, and the vacuum can is closed. A brass plug with two o-rings is used to seal the port in the top flange of the can. At this point the vacuum can, full of argon and containimg a sample, can be removed from the glovebox and joined to the rest of the cryostat by means of a indium seal. The electrical leads pass out of the vacuum can into the liquid helium space through epoxy feedthroughs and are joined to wiring leading to the top flange of the cryostat by means of Amphenol multi-pin

Figure 12: (facing page)

Simplified diagram of the low temperature specific heat cryostat (not to scale).

a- Pumping line for vacuum can.

b- Liquid helium fill port.

c- Glass liquid helium Dewar.

d- Pumping line (3/4 inch thin wall stainless steel tubing).

e- Joint with indium seal.

f- Electrical feedthrough.

g- Vacuum can.

h- Temperature regulated block and sample holder assembly. For details of this area see figures 13 and 14.

i- Socket for pumping line plug.

j- Pumping line plug.

k- Control rod.

l- Radiation shields.

m- Pumping port for Dewar.

n- Control rod feedthrough.

The distance from the top of the Dewar to the bottom of the vacuum can is 35 inches.

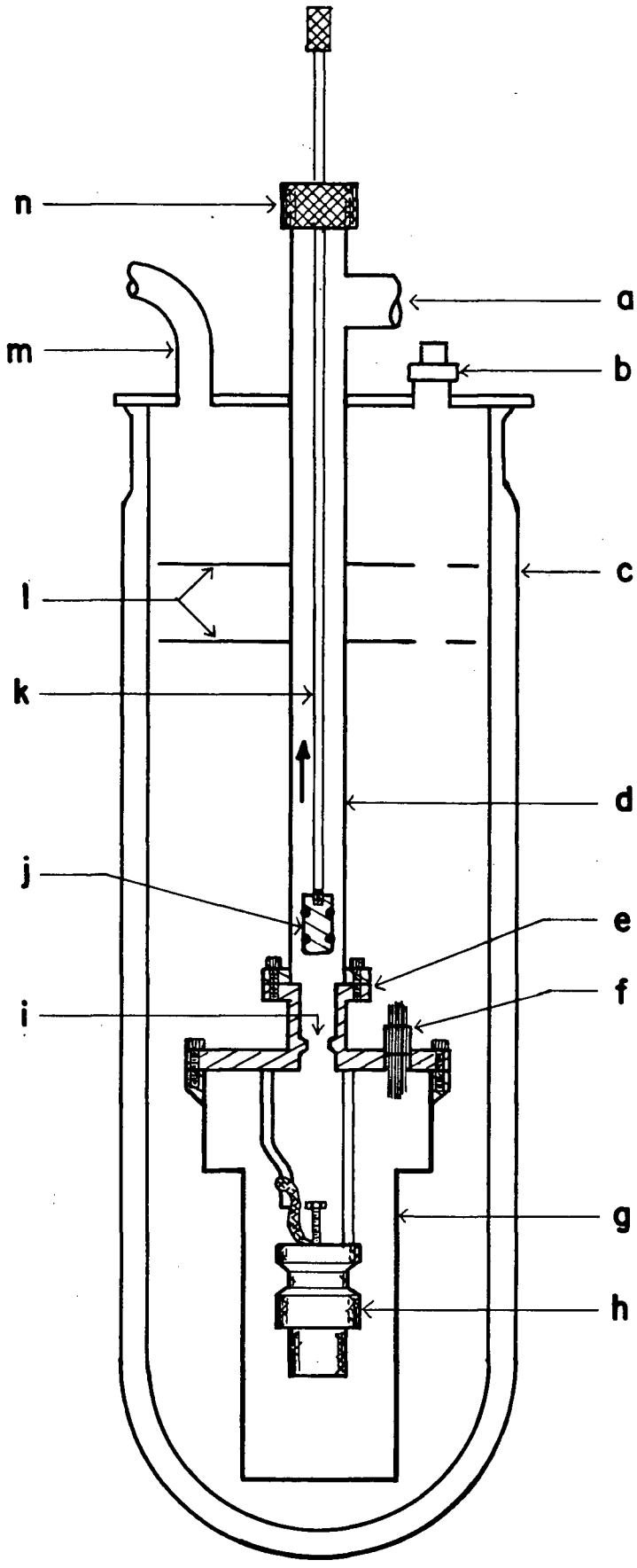
n
a
m
b
c
l
k
d
j
e
f
i
g
h

connectors.

Once the cryostat has been assembled and installed in a liquid heliun dewar, the pumping line is evacuated. A rod is then lowered down the center of the pumping line and threaded into the brass plug. By raising the rod, the plug is removed to a chamber at the top of the cryostat, and the argon is pumped out of the vacuum can. The sample is never exposed to air. After the can is evacuated, the system is precooled to liquid nitrogen temperature, and then liquid helium is transferred into the dewar in the usual way. If necessary, at the end of a measurement when the system is again at room temperature the plug may be replaced, sealing the sample in vacuum. The vacuum can may then be removed from the cryostat and brought back into the glovebox for inspection or removal of the sample.

The copper reference block inside the vacuum can is shown in detail in figure 13. It is supported on three thin wall stainless steel tubes. To allow cooling of the block, a thermal link to the bath is made by means of a brass rod and a length of copper braid. This arrangement gives a block to bath thermal conductance of 0.8mW/K at 4.2K, which allows the block to be regulated above the bath temperature without excessive amounts of power. The block cools from 80K to 4.2K in about 90 minutes.

The sample platform (figure 14) is a sapphire chip 6mm square and .1mm thick. On the side facing the copper

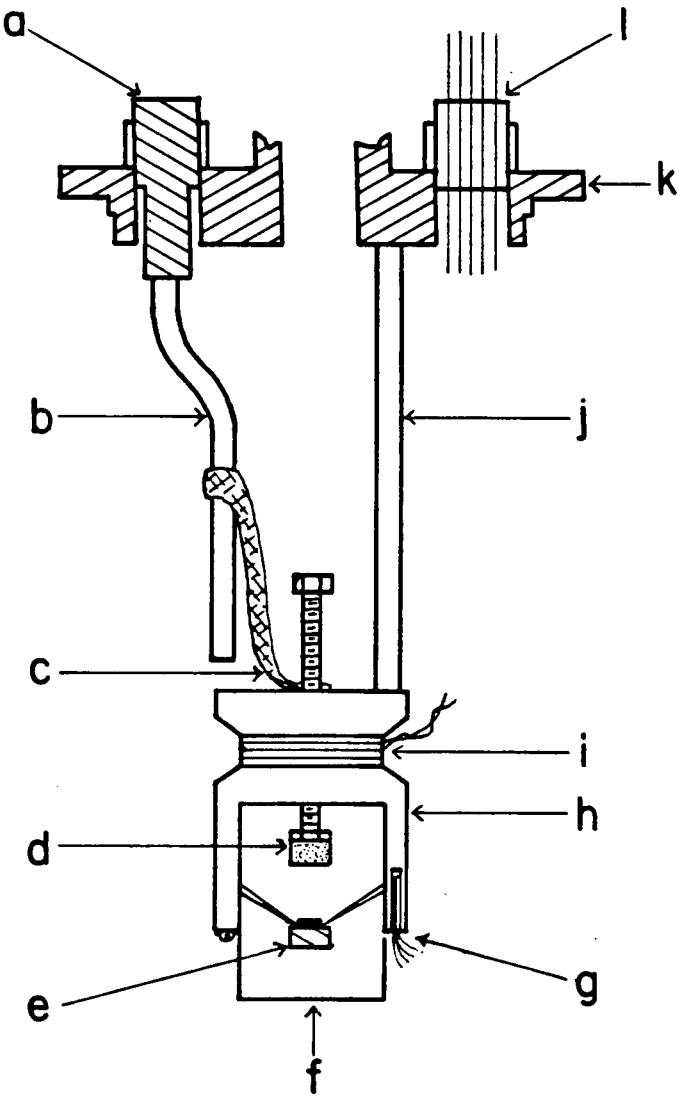

Figure 13: Detail of the vacuum can interior.

a- Copper plug
b- Brass rod (3/16 inch solid)
c- Copper braid. This and the brass rod form the block to bath heat link.
d- Support used in sample mounting.
e- Sample (see figure 14).
f- Radiation shield.
g- Germanium resistance thermometer.
h- Copper reference block.
i- Block heater.
j- Support (thin wall stainless steel tubing- one of three).
k- Top flange of vacuum can (stainless steel).
l- 8-lead electrical feedthrough (one of three).

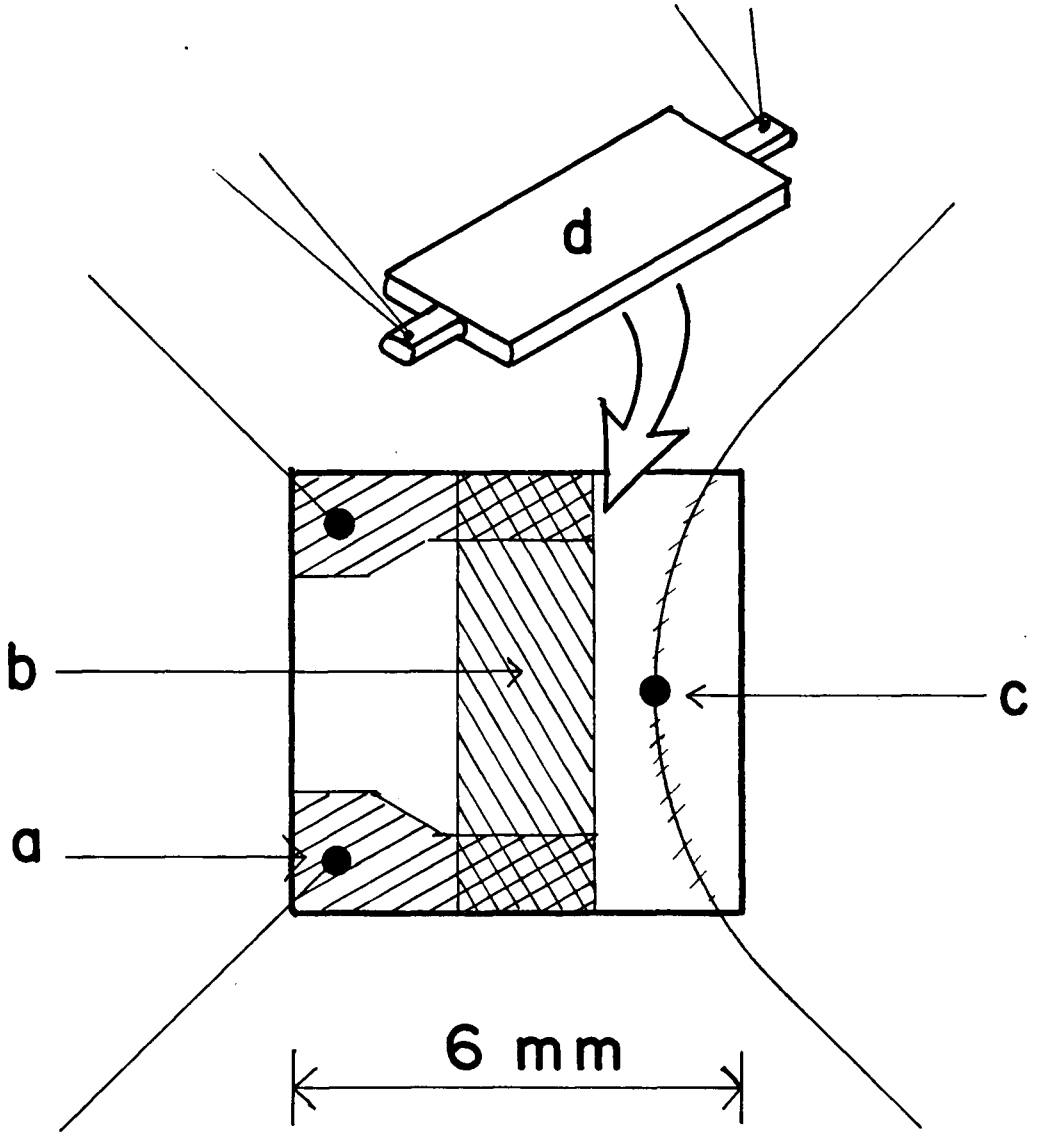

Figure 14: Detail of the top side of the sample platform (the side away from the sample).

a- Gold contact pad.

b- Nichrome film heater.

c- Au+.07%Fe vs chromel thermocouple.

d- Carbon resistor slice. This is glued on top of the heater.

block (the upper side) there is an evaporated thin film nichrome heater. The two contact pads were made first. They consist of about 1μm of gold, underlaid by a very thin layer of chromium to provide good adhesion. The chromium and gold were evaporated in a standard vacuum deposition unit, using electrically heated 'boat' sources and a copper foil mask. A nichrome layer about 15nm thick was then deposited through a different mask using an electron beam gun source. The resistance of this film is about 600Ω and is nearly temperature independent. The leads to the heater are .003 inch diameter brass wires and are soldered to the gold contact pads with about 1mg of pure indium. Two sample thermometers were used. The first was a Au+.07%Fe *vs* chromel thermocouple (Sparks and Powell 1972, Rosenbaum 1968) in a differential configuration with on junction on the block and the other on the sample platform. The second sample thermometer is a small slice of an Allen-Bradley carbon composition resistor which is glued on top of the sample heater. Both the resistor and thermocouple were bonded to the sample platform using Emmerson and Cummings Stycast 2850 high thermal conductivity epoxy. Sample thermometry will be discussed in more detail in section 3.3.3.

Samples are attached to the platform using a few milligrams of Cry-Con[13], a high thermal conductivity grease. Sample mounting is facilitated by a small foam cushioned support which holds the platform while the sample is pressed onto it. The specific heat of Cry-Con has been measured (Torikachvili et al. 1983) and the grease heat capacity can therefore be subtracted from the data, as will be discussed in section 3.4.2. Samples can be removed by very carefully sliding them sideways off the platform, or by dissolving the grease in cyclohexane.

3.3.2 MEASUREMENT AND CONTROL OF THE REFERENCE BLOCK TEMPERATURE

The temperature of the reference block is measured by means of two encapsulated doped germanium resistance thermometers. These were purchased from Lakeshore Cryotronics[14]. Lakeshore also supplied calibrations covering the temperature range 1.4 to 100K. One thermometer is used in a feedback loop to control the block temperature, the other is used as a backup and a check on the stability of the calibration. The resistances of the thermometers are measured with a low

---

[13] Air Products and Chemicals, Inc., Allentown, PA

[14] Westerville, Ohio, models GR-200B-1500 and GR-200B-1000

power automatic resistance bridge.[15] This instrument makes a four terminal AC resistance measurement, using 30Hz excitation, phase sensitive detection, and a typical power dissipation in the thermometer of 1nW at 4K.

The temperatures derived from the two thermometers agreed within about ±3mK below 10K and ±10mK above. The differences were random, and correspond roughly to the accuracy with which the resistances were measured.

Lakeshore's calibration of one of the thermometers was checked between 2K and 20K by S. Steel and W.N.Hardy. The standards used were ^4He and H_2 vapour pressure and the susceptibility of the paramagnetic salt $Gd_2(SO_4)_3 \cdot 8H_2O$. The salt was used to interpolate the temperature scale between the regions where vapour pressure could be used. The Lakeshore calibration gave temperatures which were consistently about 10 to 15mK higher than the vapour pressure-salt temperature. Unfortunately, the existence of temperature gradients of this magnitude between the vapour pressure cell and the Ge thermometer in the calibration cryostat could not be ruled out. The Lakeshore calibration was therefore used without any adjustments.

The accuracy of the block thermometry is now summarized. Block temperatures were measured with a

---

[15]AVS-45 from R.V.Elektroniika, Finland, or similar.

precision of ±3mK below 10K and about 10mK above 10K. The two thermometers agree with each other, if the manufacturer's calibrations are used. Any systematic errors in the temperature scale are believed to be less than about 15mK, because of the calibration check. Thermometry of this accuracy is more than adequate for this experiment.

As previously mentioned, one of the Ge resistors was used in a feedback loop to control the block temperature. The automatic resistance bridge has an adjustable internal reference resistance, and a voltage output which is proportional to the difference in resistance between the thermometer being measured and the reference. Using this as an error signal, it is a simple matter to regulate the block temperature. The stability of the block temperature during the time required for a specific heat measurement was ±0.1mK or better, which is sufficient.

3.3.3 SAMPLE THERMOMETRY

The first sample thermometer installed was a differential thermocouple with one junction on the sample platform and the other on the reference block. The materials were Au+.07%Fe for the block to platform leg and chromel (also known as KP) for the others. This thermocouple pair was chosen because of its unusually high sensitivity at low temperatures, for example 13μV/K

at 4.2K and 9μV/K at 2K (Sparks and Powell 1972, Rosenbaum 1968). The thermocouple voltage was measured with a Keithley 148 nanovoltmeter.

The advantages of the thermocouple include its small size and low heat capacity, and that it directly measures the sample to block temperature difference θ. However, the thermocouple proved unsatisfactory for several reasons. First, the total noise was about $\pm.02\mu$V at the nanovoltmeter input, corresponding to a temperature noise of ±2mK at 4K. This should be compared to a typical value of θ_0, the maximum temperature difference during a measurement, which is 50mK. (One tries to keep $\theta_0<.02T$ - see section 3.4) The noise situation is even worse at lower temperatures, since smaller θ_0s must be used and the sensitivity of the thermocouple decreases. Another problem was the lack of an absolute calibration of the thermocouple; thermocouples made from different samples of Au-Fe wire may have sensitivities which differ by 5% or more. Standard tables can only be used for these thermocouples if one is prepared to accept these possible systematic errors.

Although the problems with the thermocouple could, in principle, have been solved by calibrating our batch of wire and signal averaging to reduce the noise, a simpler solution was to add a small resistance thermometer to the sample platform. This is a .5mm thick

slice cut from the centre of an Allen-Bradley 15Ω, .1W carbon resistor. Its mass is 10mg. Small portions of the original resistor leads remain, and two .003 inch diameter brass wires were soldered to each of these to allow for a four terminal resistance measurement. Brass was chosen because its thermal conductivity is low enough that wires of reasonable mechanical strength can be used without creating too large a sample to block heat link. One side of the resistor slice was covered with a 6μm mylar sheet. This was then glued to the sample platform, directly on top of the thin film heater. The mylar served to prevent electrical contact. The adhesive was Stycast 2850 epoxy.

Since the response time of the automatic resistance bridge used for the block thermometers is too long to allow it to follow the thermal decays of the sample, the sample resistor was measured with the AC 'bridge' circuit shown in figure 15. It is similar to one described by White (1979). In the diagram, A1 and A2 are OP-07 low noise operational amplifiers, R_s is the sample thermometer, and r represents the resistances of the leads (the lead resistances need not be equal). R_b is a resistance box, and the other resistors are 1% metal film types.

The circuit makes a four terminal AC measurement. A1 is a non-inverting follower, which forces the voltage at point P to be equal to V_1. A2 is a constant current

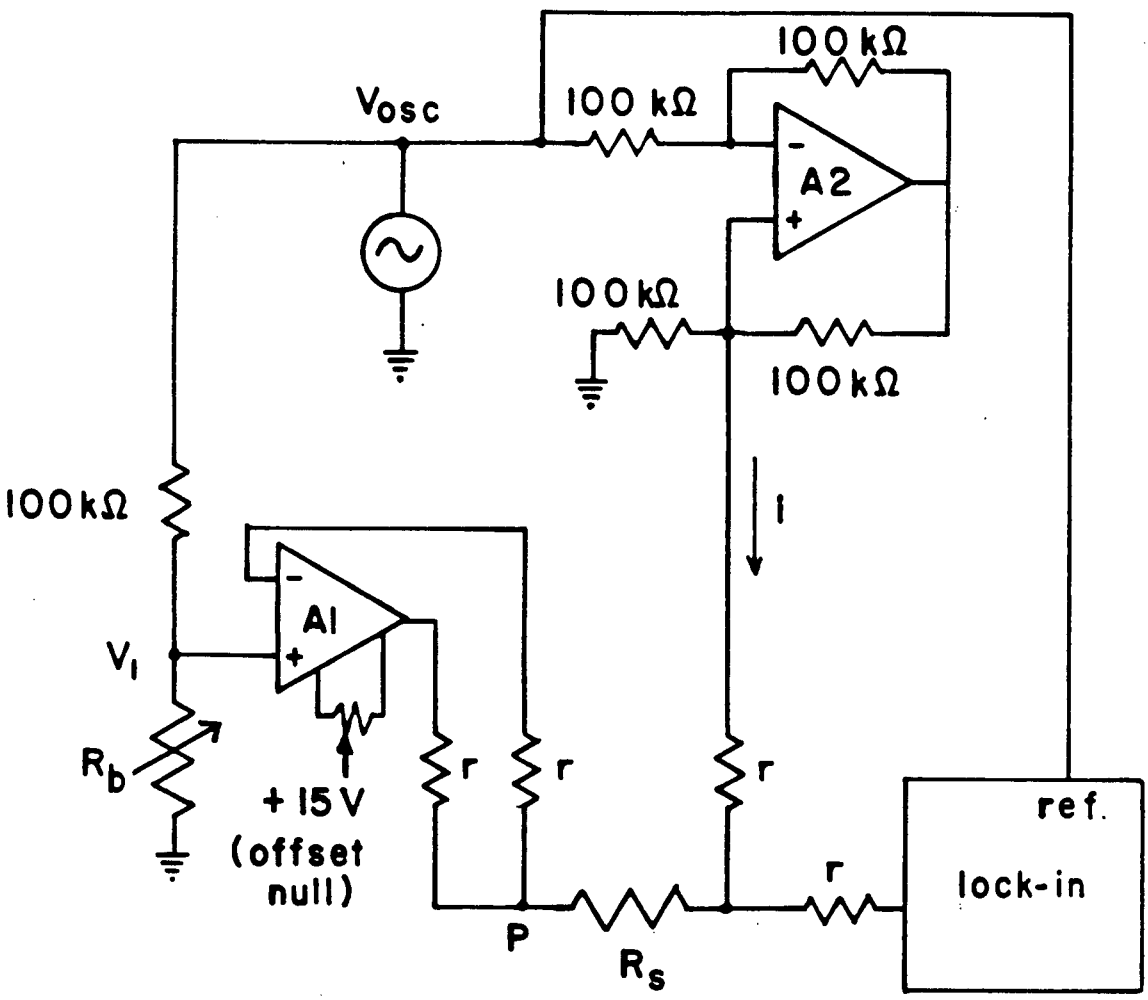

Figure 15: Circuit diagram of the AC bridge used to measure R_s. Its operation is described in the text.

source which delivers an AC current $i=V_{osc}/100k\Omega$ through R_s. The detector is a Princeton Applied Research HR-8 lock-in amplifier referenced to the oscillator which drives the circuit. The bridge is balanced by adjusting R_b to give zero signal at the lock-in. In this case we have

$$iR_s=V_{osc}R_s/100k\Omega=V_1=V_{osc}R_b/(100k\Omega+R_b)$$

$$R_s=R_b/(1+R_b/100k\Omega) \qquad (3-8)$$

Since $R_s \leq 1400\Omega$ in the temperature range used, this effectively is $R_s=R_b$. When the bridge is out of balance, the detector voltage is $(R_b-R_s)V_{osc}/100k\Omega$. This linear response is one advantage of using a bridge with active components.

When using the bridge, the oscillator level must be kept low enough to avoid significant heating of the sample platform. The levels used were 800mV rms above 8K, 400mV from 4 to 8K, and 200mV below 4K. The power dissipation in the resistor is, for example, 5nW at 4.2K. Considering that the thermal conductance between the sample platform and the block is about $6\mu W/K$ at this temperature, this is acceptably small.

At 4.2K, $dR_s/dT=108\Omega/K$, so the temperature sensitivity of the bridge is $430\mu V/K$. The lock-in is normally operated on a $20\mu V$ full scale range. The frequency used was 394Hz. Quadrature signals were 5% of full scale or less when the bridge output in phase with V_{osc} was zeroed. Total noise at the lock-in input is

about ±1mV peak-to-peak, although of course the lock-in is insensitive to most of this. With a time constant of .1s, the noise at the lock-in output corresponds to ±0.2μV at its input, or ±0.5mK at 4.2K. This is much better than the thermocouple. Although the noise can be reduced further by increasing the lock-in time constant, this was not done because it is also important to keep the time constant much shorter than the sample's thermal relaxation time.

Using the calibrated germanium thermometers, it is easy to make an accurate calibration of the sample thermometer. With the sample heater off, the sample is at the same temperature as the reference block. During each experimental run, values of the sample thermometer resistance and the germanium thermometer temperature T were recorded. About 25 temperatures were used in a fit to an equation of the form (White 1979)

$$\ln T = \sum_{n=1}^{N} P_n \ln R \qquad (3\text{-}9)$$

The fits were made using an orthogonal polynomial least squares method[1.6]. The program determines the best polynomial order N by increasing it untill the improvement in the fit is no longer statistically significant. N was always 5,6, or 7. Residual deviations

---

[1.6] UBC subroutine DOLSF (Moore 1981)

between the data and the fit were typically ±2mK.

A new calibration had to be made for each run. The calibration changed each time the cryostat was warmed up to room temperature for sample replacement. Typical calibration changes corresponded to temperature errors of about 50mK. It is possible the calibration changes are related to the procedure used to remove most of the samples. This involves immersion of the entire sample platform, including the resistor, in cyclohexane, which dissolves the grease holding the sample on.

As an example of one of these calibrations, figure 16 shows the data and fit obtained during the run on a $Li_{.30}NbS_2$ sample. The data are shown as small crosses. Note that, as might be expected, the fit breaks down rapidly outside the temperature range covered by the calibration points. For this reason, the derivative dR_s/dT of the fit is not expected to be valid at the endpoint temperatures. Since an accurate dR_s/dT is required for specific heat data analysis, specific heat data were not taken at the endpoints. The other calibration points are, for the most part, the same temperatures at which the specific heat was measured.

3.3.4 COMPUTER DATA AQUISITION SYSTEM

The thermal decays used to determine the heat capacity are recorded using a microcomputer, which also controls the sample heater. The computer is based on a

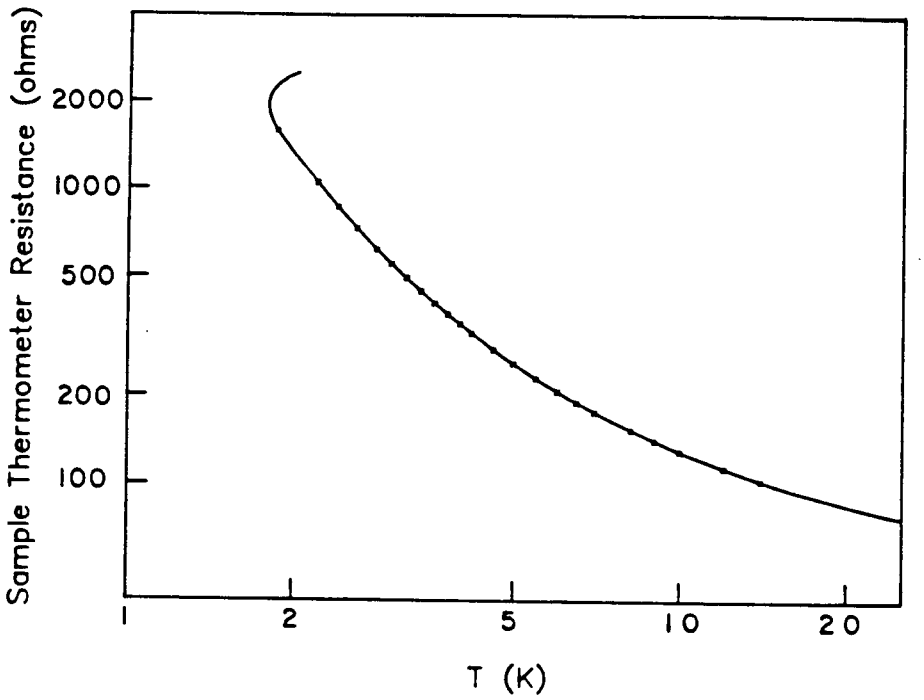

Figure 16: Sample thermometer resistance as a function of temperature. The line is a fit using equation (3-9).

Z80 microprocessor. It was assembled by the Physics Dept. Electronics Shop, using, for the most part, commercially available S100 bus circuit boards. Two 8-inch floppy disk drives and 64 kbytes of memory are used.

A department standard interface system (PHYS44), designed and built by the Physics Electronics Shop, is used for data aquisition and control of the experiment. A number of input and output devices are available in the PHYS44 system. Those used for the specific heat measurements are 8, 12, and 16 bit analog to digital converters, and a computer controlled relay used to switch the sample heater on and off. The 16 bit converter is a dual slope device[17] with a conversion time of about one second. This was used when the sample's relaxation time was greater than about 30s. For typical samples, this occurred at temperatures above about 8K. At lower temperatures, the relaxation time is shorter, and a shorter conversion time is required in order to get a sufficient number of data points during a thermal decay. For the first few runs of the system, the only fast A/D converter available was an 8 bit device[18]. This did not have sufficient resolution, and was replaced by

---

[17] Intersil ICL 8068/ICL 7104

[18] National ADC 0801

a 12 bit successive approximation converter[19].

A multiplexer in the PHYS44 system allows up to 8 different analog voltage inputs to be connected to either of the A/D converters. Inputs from the specific heat experiment were the sample heater voltage, and the recorder outputs of two automatic resistance bridges (Ge thermometers), the nanovoltmeter (sample thermocouple), and the lock-in amplifier in the sample resistance thermometer bridge.

3.4 MEASUREMENT PROCEDURE AND DATA ANALYSIS

3.4.1 MEASUREMENT PROCEDURE

The general principles of the relaxation time method have been discussed in section 3.1. The experimental procedure used will now be described in more detail. The measurement cycle is shown in figure 17. It begins with the reference block and sample at a common temperature T set by the block temperature regulator. The calibrated resistance thermometers on the block are read at this time, and the AC bridge measuring R_s is balanced. The microcomputer then switches on the sample heater. The sample heater current comes from a regulated DC power supply and passes through a relay controlled by the computer. The voltage across the

---

[19]Analog Devices AD572

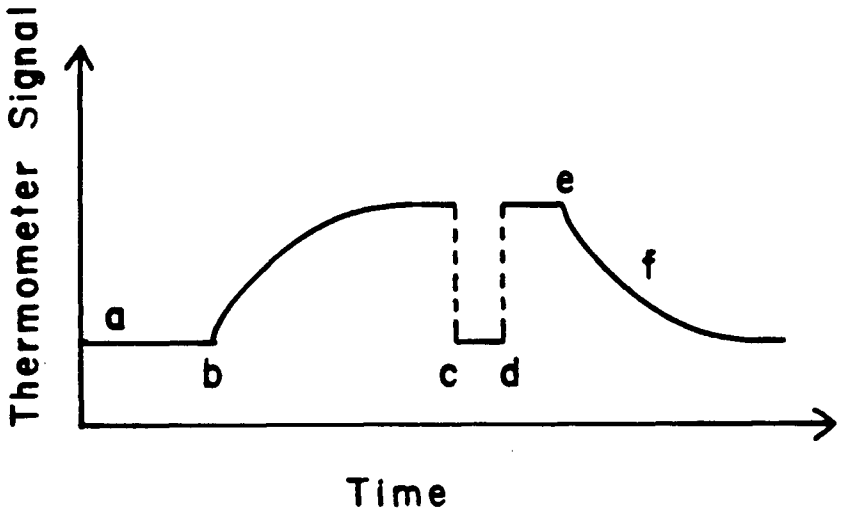

Figure 17: Specific heat measurement cycle.

The major steps in the cycle are:

a- Balance sample thermometer bridge

b- Sample heater on

c- Balance sample thermometer bridge to measure θ_0.

d- Reset bridge.

e- Sample heater off

f- Computer monitors the thermal decay.

sample heater is read using a different pair of leads and a Keithley 177 digital multimeter. After the heater is turned on, the temperature difference θ between the sample and block rises, eventually reaching a maximum value θ_0 whick is typically about 50mK. This causes the R_S bridge to go out of balance. The R_S bridge is nulled again, providing a measurement of θ_0 which is independent of the gain of the bridge cicuit. The resistance box is then set back to its original value.

The next step is to prepare the microcomputer to collect data. While the heater is still on, the experimenter gives it a sampling rate and a sampling duration. The duration of the measurement was usually chosen to be about four times the expected thermal relaxation time τ. The sampling rate was then chosen to give 90 to 100 samples during the measurement. The operator also chooses which analog to digital converter is to be used. In early runs, the 8 bit converter was used for sampling rates greater than 1 sample/s, otherwise the the 16 bit converter was used. After the 12 bit converter was installed, it was used in place of the 8 bit device.

Once all this information has been entered, the microcomputer reads the sample thermometer voltage, which at this time corresponds to θ_0. It then shuts off the sample heater by opening the relay, and repeats the thermometer reading at the preset sampling rate. The

timing is done with a quartz oscillator counter/timer which is part of the microcomputer system. At the end of the measurement, the microcomputer stores the values of sample thermometer voltage and time on a floppy disk for later analysis. If desired, several thermal decays can be made at the same block temperature T, and the results averaged to reduce the noise. Signal averaging was usually performed when the thermocouple sample thermometer was being used, but was not normally necessary when using the carbon resistor sample thermometer.

The thermal relaxation time τ is a function of temperature. It is therefore important to have θ_0 small enough that τ does not change significantly during the thermal decay. Sample heater powers were chosen so that $\theta_0/T<0.02$, which ensures τ is constant to about 2% or better for typical samples.

To get the specific heat as a function of temperature, the thermal relaxation measurements are repeated for different block temperatures. Typically about 25 temperatures covering the range 2.6 to 25K were used.

Data analysis is done on the UBC Computing Centre's Amdahl V/8, since the calculation speed of the microcomputer is too low. The data are transferred to the Computing Centre over a high speed data line.

3.4.2 COMPUTATION OF THE SPECIFIC HEAT

The analysis begins with the data in the Amdahl in the form $t_n, V(t_n)$ (n=1 to N), where $V(t_n)$ is the sample thermometer voltage at time t_n, N is the number of samples, and, since the sampling was carried out at a fixed rate $1/t_s$, $t_n=nt_s$. Since the maximum temperature difference θ_0 is small, V is proportional to θ even for the resistor sample thermometer, and V itself can be fit to an exponential decay without converting each voltage to a temperature. So, V is fit to an equation of the form

$$V(t)=V_1 e^{-t/\tau_1}+V_{os} \qquad (3\text{-}10)$$

where V_{os} is a possible small voltage offset. ($V=V_{os}$ when $\theta=0$.) V_1, τ_1, and V_{os} are all parameters determined by the fit. The fitting is done by minimizing the reduced chi-squared parameter

$$\chi_r^2 = \frac{1}{(N-3)\delta V^2} \sum_{n=1}^{N} (V(t_n)-(V_1 e^{-t/\tau_1}+V_{os}))^2 \qquad (3\text{-}11)$$

where N-3 is the number of degrees of freedom, and δV is the standard deviation of each of the $V(t_n)$, or, equivalently, the noise at the sample thermometer voltage output.

To illustrate the data fitting and analysis, the data on a $Li_{.30}NbS_2$ sample at T=4.60K will be used (figure 18). The resistor sample thermometer was used for this measurement. The noise at the lock-in amplifier

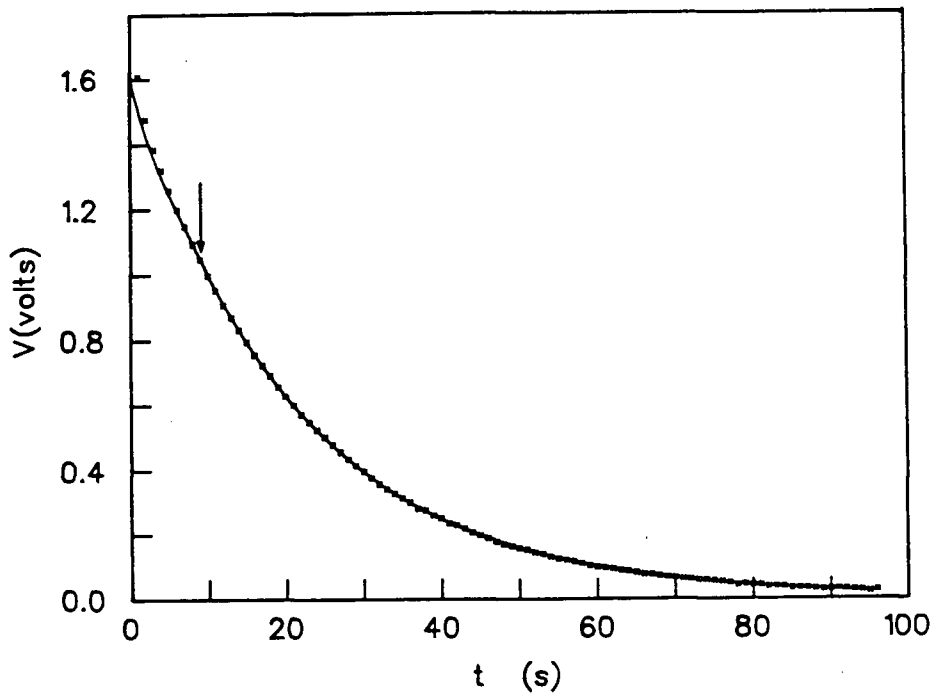

Figure 18: Data for a typical thermal decay. The figure shows the voltage at the lock-in output as a function of time, as recorded by the microcomputer. The line is a fit to equation (3-10). The arrow marks the beginning of the data used in the fit.

output was about ±.002V, so for the fit δV was taken to be .002V. It should be pointed out that the parameter values which minimize χ_r^2 are independent of δV, so that only a rough estimate is needed. When all of the data are used in the fit, the best fit value of χ_r^2 is 17.2. This is unacceptably high, since for a good fit we expect $\chi_r^2 \simeq 1$.

The reason for the large value is clear on examination of figure 18; the thermal decay was not truly a single exponential. This happened because the sample's thermal conductivity was low enough that it was not isothermal during the decay. A solution of the heat flow problem for this case (Appendix 2) shows that the temperature at the sample platform decays according to the infinite sum of exponentials

$$\theta(t) = \sum_{n=1}^{\infty} \theta_n e^{-t/\tau_n} \qquad (3\text{-}12)$$

where

$$\frac{\theta_1}{\theta_0} = \frac{2k_w\tau_1}{\mu_1 l(\cot \mu_1 l + \tan \mu_1 l)(k_w\tau_1 - C_{pl}) + k_w\tau_1 + C_{pl}} \qquad (3\text{-}13)$$

and

$$C_s = (k_w\tau_1 - C_{pl})\ \mu_1 l\ /\ \tan \mu_1 l \qquad (3\text{-}14)$$

Here C_s and C_{pl} are the heat capacities of the sample and sample platform, respectively, k_w is the platform to block thermal conductance, and $\mu_1 l$ is an eigenvalue defined in appendix 2. One finds that $\tau_n << \tau_1$ for $n>1$, so

that after dropping the first few data points the rest of the data fit a single exponential very well, allowing us to determine θ_1 and τ_1 from the fit.

In the example, the first eight points are dropped, resulting in a best fit with χ_r^2=.83. χ_r^2 does not decrease significantly if more points are dropped. The fit determines values of τ_1, V_1 (the voltage corresponding to θ_1), and V_{os}. In the example, these are 21.36s, 1.588V, and .005V, respectively. The ratio θ_1/θ_0 is given by

$$\theta_1/\theta_0=V_1/(V(t=0)-V_{os})=1.588/(1.771-.005)=.899$$

To determine C_s, we also need k_w. With the sample heater off, the thermometer resistance R_s was 285.39Ω, corresponding to T=4.5981K using the fitting function (3-9). At the maximum sample temperature, R_s was 281.08Ω, corresponding to $T+\theta_0$=4.6512K, or θ_0=53.1mK. The sample heater power P was .371μW, giving

$$k_w=P/\theta_0=6.98\mu W/K.$$

The sample platform heat capacity had been measured previously (see section 4.2), and at this temperature was 29.6μJ/K. To this should be added the heat capacity of the 6mg of Cry-con grease used to mount the sample. (the grease is considered part of the platform rather than part of the sample.) Torikachvili et al. (1983), have measured the specific heat of Cry-con, and give a polynomial fit to their data which is valid between .56 and 20K. Using this fit, the heat capacity of 6mg of

grease at 4.60K is 4.93μJ/K (±7%), which when added to the heat capacity of the bare platform gives a total platform heat capacity of 34.5μJ/K.

The values of θ_1/θ_0, τ_1, k_s, and C_{pl} are now inserted into equation (3-13) which is solved numerically to get $\mu_1 l$=.609. This value is inserted into (3-14) to get

$$C_s=(k_w\tau_1-C_{pl})\mu_1 l/\tan\mu_1 l=.100\text{mJ/K}.$$

Since the sample mass was 117mg and the molecular weight of NbS_2 is 157.1g/mole, the molar specific heat c is .136J/mole-K.

Note that if the non-exponential nature of the decay is not taken into account, we would use simply

$$C_s=k_w\tau_1-C_{pl} \qquad (3\text{-}15)$$

which would result in a 13% error. (In some of the other samples the effect is larger; the worst case was the Li_1NbS_2 sample at 2.73K, which had $\mu_1 l/\tan\mu_1 l$=.15.) The value of $\mu_1 l$ is related to the thermal conductivity K_s of the sample. From (A2-10),

$$(\mu_1 l)^2=C_s l/K_s A\tau_1 \qquad (3\text{-}16)$$

where l is the thickness of the sample and A its cross-sectional area. Taking approximate values l=3mm and A=π(3mm)^2 gives K_s=.029W/m-K for the $Li_{.30}NbS_2$ sample at 4.6K. For comparison, commercial copper has a thermal conductivity of about 500W/m-K at the same

temperature, and nylon has about .01W/m-K (White 1979). Since the sample is a pressed powder, the value for K_s is not characteristic of undivided $Li_{.30}NbS_2$, which should have a considerably higher thermal conductivity.

3.4.3 ACCURACY OF THE SPECIFIC HEAT

Most of the specific heat data is estimated to be accurate to a few percent. In cases where the 8 bit analog to digital converter and thermocouple sample thermometer were used, or where the sample thermal conductivity was unusually low (Li_1NbS_2), the accuracy is poorer. These cases are pointed out in section 4.4 where the data are presented. In this section, an error estimate of a typical measurement is carried out, in order to show the factors which limit the accuracy of the measurement. The example used is $Li_{.30}NbS_2$ at 4.60K, as in the previous section.

Errors which contribute to the scatter in a plot of c as a function of T for a particular sample will be called random errors and are treated first. Errors which do not contribute to the scatter in a c(T) plot will be called systematic errors. Examples of systematic errors are errors in the temperature scale or the mass of a sample. The reason for making the distinction between random and systematic errors in this way is to allow an understanding of the scatter in the c(T) plots. This understanding aids in distinguishing noise from genuine

fine structure in the specific heat.

The final step in data analysis is the calulation of C_s starting from k_w, C_{pl}, τ_1, V_1, and V_{os}. The uncertainties in τ_1, V_1, and V_{os} are correlated, since all these are determined from the same fit. The uncertainty in V_{os} is so small that it makes an insignificant contribution to the uncertainty in the final result. Using this fact, and treating only random errors at this point, we have

$$(\delta c_s)^2 = (\delta k_w \frac{\partial c_s}{\partial k_w})^2 + (\delta \tau_1 \frac{\partial c_s}{\partial \tau_1})^2 + (\delta V_1 \frac{\partial c_s}{\partial V_1})^2 + 2\sigma_{\tau_1 V_1} (\delta \tau_1 \frac{\delta c_s}{\delta \tau_1})(\delta V_1 \frac{\delta c_s}{\delta V_1}) \quad (3\text{-}17)$$

where δ in front of a quantity indicates the uncertainty in that quantity, and $\sigma_{\tau_1 V_1}$ is the correlation coefficient between $\delta\tau_1$ and δV_1. The correlation coefficient is determined by the fitting program. The uncertainties $\delta\tau_1$ and δV_1 can also be determined from the fit, but not without some ambiguity.

According to standard statistical theory (Bevington 1969, for example), if the errors in each data point are random, then the uncertainty in a parameter determined from a non-linear least squares fit is the amount by which that parameter must be changed in order to increase χ^2 by one from its minimum (best fit) value. As the parameter in question is varied, χ^2 must remain minimized with respect to all the other parameters. Here

(cf. 3-11),

$$\chi^2 = \frac{1}{(\delta V)^2} \sum_{n=1}^{N} (V(t_n) - (V_1 e^{t_n/\tau_1} - V_{os}))^2 = (N-3)\chi_r^2 \quad (3\text{-}18)$$

If the errors in the different samples $V(t_n)$ are correlated, for example if there is a significant amount of low frequency noise in the data, then the criterion above can lead to parameter errors that are too small. Roughly speaking, some of the 'averaging out' which one has expected has not taken place. Some low frequency noise is present in the thermal relaxation data, and it is therefore safer to determine the uncertainties in the fitted parameters using a different criterion. This is that the uncertainty in a parameter is the amount by which it has to be changed in order to <u>double</u> χ^2.

When this is done for our example, the results are $\delta\tau_1$=.4s, δV_1=.02V, and δV_{os}=.005V. A comparison of the last two of these justifies the earlier statement that δV_{os} is not important. The correlation coefficient between τ_1 and V_1 is -.80. Percentage errors are 2% in τ_1 and 1% in V_1.

The thermal conductance of the wire is given by $k_w = P/\theta_o$. P is known with an uncertainty of 0.1%, which is insignificant. θ_o is determined from two resistance values, say R_1 and R_2, both of which are determined with a precision of 0.01Ω. Assuming no significant error in the calibration, the result for the example is

$$\delta k_w/k_w=\delta\theta_o/\theta_o=\delta(R_1-R_2)/(R_1-R_2)=\sqrt{2}(.01\Omega)/4.31\Omega=0.3\%$$

The various terms in (3-17) can be evaluated using finite differences, giving (recall C_s=.100mJ/K)

$$\delta k_w(\partial C_s/\partial k_w)=+.0003\text{mJ/K}$$

$$\delta\tau_1(\partial C_s/\partial\tau_1)=+.0023\text{mJ/K}$$

$$\delta V_1(\partial C_s/\partial V_1)=+.0013\text{mJ/K}$$

Combining these using (3-17) gives

$$\delta C_s=.0015\text{mJ/K}$$

or a percentage error in C_s of 1.4%.

Total random errors of about this size (1 or 2 percent) are typical, and are consistent with the scatter in the c(T) plots for most of the samples. In most cases, the largest contribution to the uncertainty in the specific heat comes from $\delta\tau_1$ and δV_1. Measurements made with the thermocouple sample thermometer have a larger uncertainty, because of the noisier temperature signal.

It is also necessary to consider systematic errors in the results. As discussed in section 3.3.2, systematic errors in the temperature scale derived from the germanium thermometer are believed to be 15mK or less and are insignificant Since the resistor sample thermometer is calibrated against the germanium thermometer, it too should contribute little error (section 3.3.3). The thermocouple sample thermometer will be assumed to measure temperature differences with an accuracy of ±5%. The sample masses were measured with

an accuracy of ±1mg or about ±1%. As discussed in section 4.2, the sample platform heat capacity C_{pl} was measured with an accuracy of about ±3%. It is typically about 20% of the total heat capacity. Since the effect of the data analysis is (approximately) to subtract C_{pl} from the total to get the sample heat capacity C_s, we can take $dC_s/dC_{pl}=-1$. This implies that the uncertainty in C_{pl} contributes about ±1% to the error in C_s. The grease heat capacity is known with an accuracy of about ±15%, due mostly to uncertainties in the grease mass. Since the grease heat capacity is typically only about 4% of the total, this is insignificant.

Combining the errors mentioned so far, yields a total possible systematic error of about ±2% or less (roughly ±6% with the thermocouple). Another possible source of error is residual gas in the vacuum can. An upper limit on the magnitude of this effect will now be estimated.

During measurements, the can was pumped continually with a diffusion pump. The pressure measured at room temperature with an ionization gauge near the pump was about $2 \cdot 10^{-7}$ torr in most cases, which is the lowest pressure obtainable with the pumping system used. In some of the experimental runs, however a small superleak was present somewhere in the vacuum can. No leak could be detected as long as the temperature of the helium bath was above its superfluid transition. When the bath

was cooled below the transition, the pressure inside the cryostat rose. By comparing two heat capacity measurements made at the same reference block temperature, one with the superleak present and the other with the bath above the superfluid transition, we can determine how sensitive C_s is to the residual gas pressure.

Such a pair of measurements was made on the $Li_{0.16}NbS_2$ sample at a block temperature of 2.73K. The first was made with the bath at 2.3K and not superfluid, the second with a superfluid bath at 1.4K. The vacuum system pressures at the ionization gauge were $1.7 \cdot 10^{-7}$ and $4.2 \cdot 10^{-7}$ torr, respectively. Thermal relaxation measurements gave a sample to block thermal conductance k_w=3.89μW/K and heat capacity C_s=47.6μJ/K with the normal bath, and k_w=6.80μJ/K and C_s=52.0μJ/K with the superfluid bath. The large difference in thermal conductance is due to conduction of heat through the gas. At these low pressures, the thermal conduction through the gas is proportional to the pressure in the cryostat, which in equilibrium is proportional to the pressure at the gauge[20] (White 1979, p130).

The relative difference in C_s between the two measurements is much smaller than the difference in k_w.

---

[20] The pressures in the gauge and the cryostat are not equal even in equilibrium, because of thermomolecular effects.

This is because of the way the measured thermal conductance is used in the calculation of the specific heat (section 3.4.2). The only reason that C_s is different for the two measurements is that the residual gas distorts the heat flow pattern in the sample. The equations used for data analysis assume that all the heat leaves the sample through the platform. When there is a significant amount of gas around the sample there is also heat loss through its free face and sides.

Most data were taken with the bath above the superfluid point, and the error due to residual gas should be small. We can roughly estimate the size of this error by assuming measured C_s values deviate from the true value by an amount which is proportional to the pressure at the ionization gauge. The error to be obtained from this assumption is really an upper limit, since high pressures mean there is flow out of the cryostat. From the two measurements described above, the proportionality constant can be obtained, and is

$$dC_s/dP=18 \text{ J/K-torr.}$$

At the lower pressure of $1.7 \cdot 10^{-7}$torr this gives a deviation from the true C_s of 3μJ/K or 6%.

Measurements at higher temperatures are affected less by residual gas, since both k_w and the sample thermal conductivity increase with increasing temperature. The $Li_{.16}NbS_2$ sample discussed above had a fairly typical thermal conductivity and size, so the

effect residual gas had on it should be typical of most samples.

In summary, then, systematic errors due to causes other than residual gas are believed to be about ±2% for typical measurements (±6% with the thermocouple sample thermometer). The error due to residual gas is difficult to estimate accurately, but is believed to be about +6% or less near 3K for typical samples. The effect of residual gas should decrease rapidly with increasing temperature.

3.4.4 DETERMINATION OF THE LINEAR AND CUBIC TERMS IN THE SPECIFIC HEAT

Specific heat data are often presented in the form of plots of c/T against T^2. This is because the specific heat of a normal metal at sufficiently low temperatures has the form (see equation 1-4)

$$c=\gamma T+\beta T^3$$

where γ and β are constants. The linear and cubic terms are due to electrons and phonons, respectively. When c/T is plotted as a function of T^2, data satisfying this equation lie on a straight line with slope β and intercept γ.

Such a plot for the $Li_{.30}NbS_2$ sample between 1.8 and 10K is shown in figure 19. The data lie on a straight line for temperatures between 2.8 and 6K. Above 6K, the phonon specific heat begins to deviate from

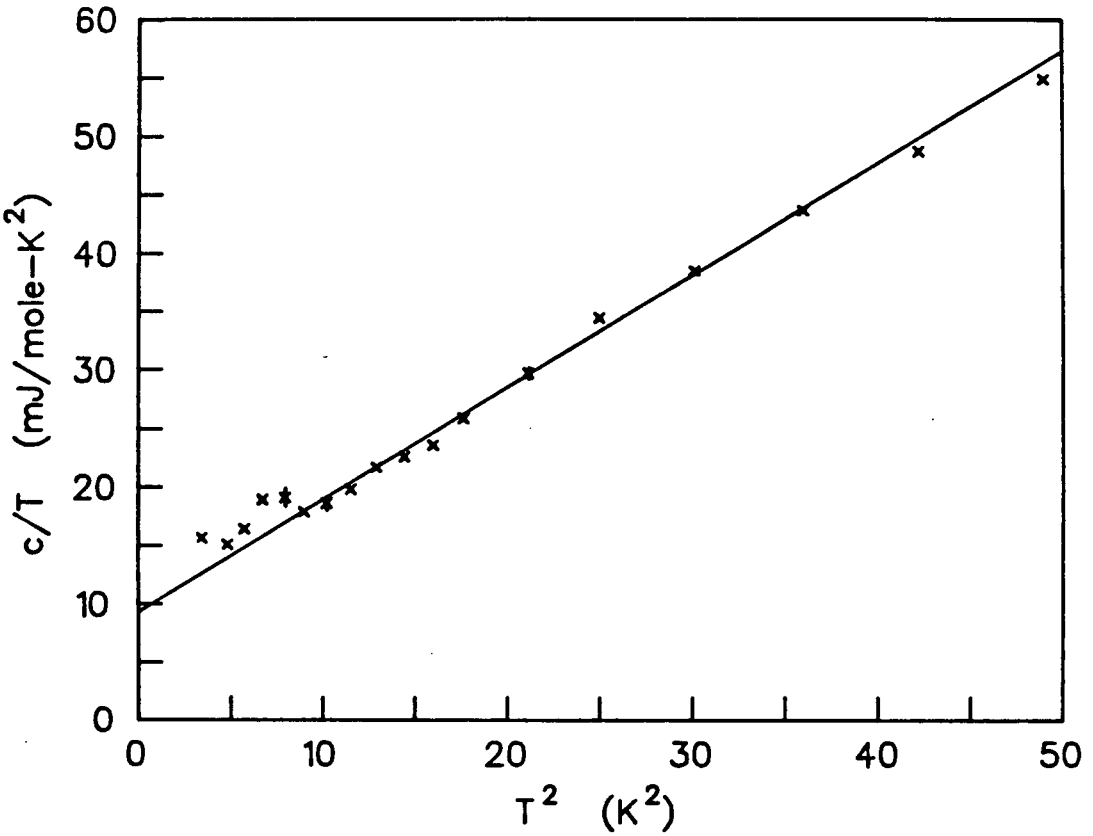

Figure 19: Specific heat of $Li_{.30}NbS_2$ as a function of temperature. The line is the fit described in the text.

cubic behavior. (This is to be expected - see section 6.5.) To reach temperatures below 2.8K, the bath temperature had to be taken below the superfluid point. The small superleak in the vacuum can caused a high helium gas pressure in the can and a large positive systematic error in the specific heat (see the previous section). Because of this, the deviation from the line of the points between 1.8 and 2.8K is not significant.

Error bars are shown on some of the points. These are the results of error calculations similar to those in the preceding section, and include random errors only. The scatter of the points around the line is consistent with the calculated random error.

The values of the constants γ and β were determined using a standard linear least squares fit to the straight line region between 2.8 and 6K. The results are $\gamma=9.4\pm.6$mJ/mole-K^2 and $\beta=.96\pm.03$mJ/mole-K^4. The errors quoted here are due to the random errors in the data only. In addition, we saw in the previous section that there was a possible residual gas effect of 6% or less near 3K, as well as possible systematic errors due to other causes of about 2%. Since the effect of residual gas should decrease rapidly with temperature, the maximum possible effect of residual gas on γ and β can be estimated by assuming +6% error at 3K and no error at 6K. Deviations in γ and β due to this can be easily estimated graphically, and when these are combined with

the other errors the error bounds are

$$\gamma = 9.4\left(^{+0.6}_{-1.6}\right) \text{ mJ/mole-K}^2$$

$$\beta = .96\left(^{+.06}_{-.04}\right) \text{ mJ/mole-K}^4$$

Analyses similar to this were performed on all the Li_xNbS_2 samples.

4. RESULTS OF THE SPECIFIC HEAT MEASUREMENTS

4.1 INTRODUCTION

In this chapter, the results of the low temperature specific heat measurements are presented. Section 4.2 describes a measurement of the heat capacity of the sample platform. Section 4.3 contains results on NbS_2, and section 4.4 on Li_xNbS_2 samples. A table at the end of the chapter summarizes the data. The interpretation of these results is discussed in chapters 5, 6, and 7.

4.2 SAMPLE PLATFORM HEAT CAPACITY

In order to extract the heat capacity of a sample from the raw data, the heat capacity of the sample platform must be known. This was measured as a function of temperature on two occasions, once before the carbon resistor sample thermometer was installed, and again after. Since most of the measurements on Li_xNbS_2 were performed with the carbon resistor in place, the sample platform results with the resistor will be presented first and in more detail.

The measurements were made as described in section 3.4.1. Recall that in the case where a sample was present, the thermal decays could not be fit with a single exponential (section 3.4.2). With no sample attached, the decays were single exponentials and the heat capacity C_{pl} could be calculated directly from

$$C_{pl}=\tau k_w \qquad (4-1)$$

where τ is the relaxation time and k_w is the thermal conductance of the wires (see equation 3-7). The results are shown in figure 20 in the form of C_{pl}/T as a function of T^2.

To avoid introducing extraneous scatter into the Li_xNbS_2 data, the sample platform heat capacity data were smoothed. The data below 5.5K were fit to an equation of the form

$$C_{pl}=aT+bT^3 \qquad (4-2)$$

using the linear least squares method. Since normal solids are expected to obey an equation of this form at sufficiently low temperatures, (4-2) is the best equation to use for the extrapolation of the platform heat capacity to temperatures below 2.74K, the lowest temperature at which it was measured. The fit parameters are $a=.42357\mu J/K^2$ and $b=.28365\mu J/K^4$.

At higher temperatures, the data deviate from (4-2), and so the smoothing was done using a least squares fit to a fourth order polynomial of the form

$$C_{pl} = aT + bT^3 + \sum_{n=2}^{4} p_n(T-5.5K)^n \qquad (4-3)$$

In (4-3), a and b have the same values as in (4-2). This ensures that at 5.5K, where the transition from (4-2) to (4-3) is made, both $C_{pl}(T)$ and its derivative are continuous. The parameters p_n are determined from a fit to all data between 5.5 and 20K, and are $p_2=-.31569\mu J/K^3$, $p_3=1.1635nJ/K^4$, and $p_4=-.13494nJ/K^5$. When the platform heat

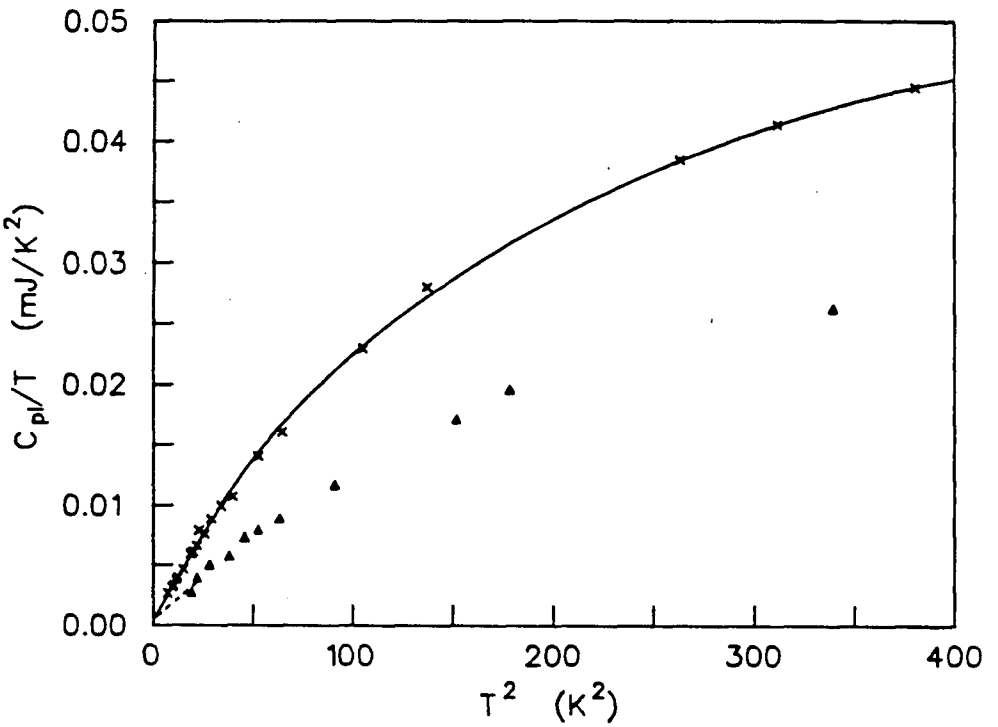

Figure 20: Sample platform heat capacity. Shown is the heat capacity of the sample platform with the resistance thermometer (x), and without it (Δ). The line is the fit described in the text.

capacity is needed for analysis of data on Li_xNbS_2 samples, (4-2) is used below 5.5K and (4-3) from 5.5 to 20K.

The data deviate from the smooth curve of (4-2) and (4-3) by ±3% or less in all but 2 cases, and this is believed to be approximately the accuracy with which the smoothed curve represents the actual platform heat capacity. The possible systematic error due to residual gas, discussed in section 3.4.3, should not be present in this measurement, because the thermal conductivities of the platform components are much higher than those of the samples.

For the first several runs of the specific heat cryostat, the carbon resistor was not in place. The heat capacity of the sample platform in this condition was also measured and is shown as the triangular points in figure 20. Because of the poor accuracy of both C_{pl} and C_s in these early runs where the thermocouple sample thermometer and 8-bit D/A converter were used, it was not considered worthwhile to smooth the data. Instead, C_{pl} values for data analysis were obtained simply by linear interpolation in C_{pl} against T^2 between the measured points. Below 4.4K, the straight line extrapolation shown in figure 20 was used.

4.3 THE SPECIFIC HEAT OF NbS_2

Figure 21 shows the specific heat of a sample of NbS_2 from batch DD9. The most significant feature is the specific heat anomaly at the superconducting transition temperature T_c. The transition takes place between 5.5 and 6.0K, and is 50%

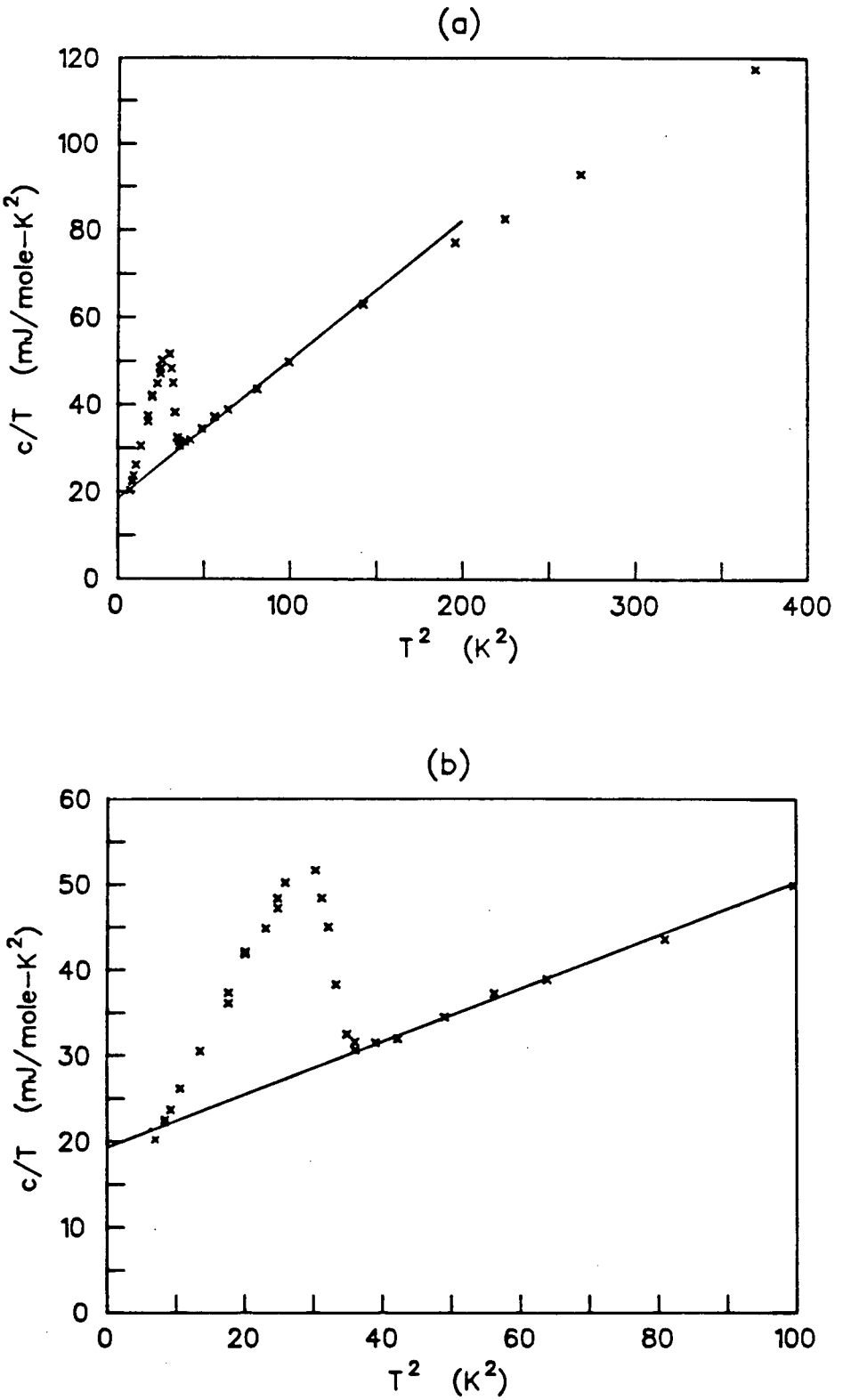

Figure 21: a- The specific heat of NbS_2.
b- Detail below 7.1 K.

The line is the fit to the normal state specific heat described in the text.

complete at 5.7K. In the normal state, at low enough temperatures, the specific heat is expected to satisfy[21]

$$c_N = \gamma T + \beta T^3 \qquad (4\text{-}4)$$

It is difficult to assign accurate values to γ and β using the normal state data alone, because of the very limited temperature range (about 6 to 8K) over which (4-4) is valid. It is possible, however, to derive an additional constraint on the fit from the superconducting data.

Because the superconducting transition is second order, the entropy in the superconducting and normal states must be equal at T_c. Thus,

$$\int_0^{T_c} (c_S/T)dT = \int_0^{T_c} (c_N/T)dT \qquad (4\text{-}5)$$

By substituting (4-4) in (4-5), we get

$$\int_0^{T_c} (c_S/T)dT = \gamma T_c + (1/3)\beta T_c^3 \qquad (4\text{-}6)$$

By evaluating the left-hand side of (4-5) a constraint on γ and β can be obtained (Schwall, et al 1976). To do this, it is necessary to extrapolate the superconducting state data to T=0. Since the electronic specific heat of a

---

[21] This equation is essentially (1-4). In this section c_N is used for the normal state specific heat, c_S for the superconducting state specific heat, and c for the measured specific heat.

superconductor is appoximately exponential well below T_c, (Tinkham 1975, p8), the extrapolation is done by assuming

$$c=c_S=Ae^{-b/T}+\beta T^3 \qquad (4-7)$$

at temperatures below the range covered by the data. The constants A and b in (4-7) were determined by plotting the measured specific heat c in the form of $\ln(c-\beta T^3)$ against T. On such plots, the four data points below 3.2K lie on a reasonably straight line. For several values of β between .3 and .4mJ/mole-K^4, plots were made, and A and b were determined. The lowest temperature at which data was taken was 2.645K. The integral in (4-6) was therefore split into two parts, covering the temperature ranges 0 to 2.645K and 2.645K to T_c, respectively. The low temperature part is determined from the extrapolation (4-7) and is described by

$$\int_0^{2.645K} (c_S/T)dT = 14.0\text{mJ/mole-K} + (1.5K^3)\beta \qquad (4-8)$$

The weak dependence on β comes about because the values of A and b determined from the plot depend on the value of β used for the plot.

The other part of the integral was determined by numerical integration of the data. Because of the broad transition, it was decided to take T_c to be 5.7K (the midpoint of the transition), but to include in the integral

the excess specific heat between 5.7 and 6.0K. That is,

$$\int_{2.645K}^{T_c} (c_s/T)dT = \int_{2.645K}^{6.0K} (c/T)dT - \int_{5.7K}^{6.0K} ((\gamma T+\beta T^3)/T)dT \qquad (4\text{-}9)$$

When this is calculated and added to the low temperature part of the integral, the result is

$$\int_0^{T_c} (c_s/T)dT = (137\pm5)\text{mJ/mole-K} - (.3K)\gamma + (8.8K^3)\beta \qquad (4\text{-}10)$$

Using (4-10) and T_c=5.7K in (4-6) gives

$$(6.0K)\gamma+(70.5K^3)\beta = (137\pm5)\text{mJ/mole-K} \qquad (4\text{-}11)$$

Requiring γ and β to satisfy (4-11) and to fit the data between 6 and 7K yields

$$\gamma=19.3\pm1.5 \text{ mJ/mole-K}^2$$

$$\beta=0.31\pm.04 \text{ mJ/mole-K}^4.$$

These values are in agreement with those of Aoki, et al (1983), which are γ=18.2mJ/mole-K^2 and β=0.33mJ/mole-K^4.

Another quantity of interest is the size of the specific heat jump Δc at T_c. For NbS_2, the ratio $\Delta c/\gamma T_c$ is 1.3, compared to 2.14 in $NbSe_2$ (Schwall, et al 1976), and 1.43 in the BCS theory (Tinkham 1975, p36). It is also possible to use the data to calculate the thermodynamic critical field $H_c(0)$ from

$$\int_0^{T_c}(c_s-c_N)dT = (V/8\pi)\ H_c^2(0) \qquad \text{(cgs units)} \qquad (4\text{-}12)$$

(Zemansky 1957) where V is the molar volume. Evaluating the integral using the exponential extrapolation (4-7) gives $H_c(0)$=1.0kG, compared with 1.28kG in $NbSe_2$ (Schwall, et al 1976).

4.4 THE SPECIFIC HEAT OF Li_xNbS_2

This section presents specific heat data for eleven Li_xNbS_2 samples. The data are given in order of increasing x. Unless stated otherwise, the data were measured using the resistor sample thermometer, 12 bit A/D converter, and the method of section 3.4. The specific heat of each sample is plotted as c/T as a function of T^2 in figures 22 to 33. The error bars on some of the data represent error calculations similar to those of section 3.4.3, and include random errors only. The coefficients of the linear (γ) and cubic (β) terms in (1-4) were determined by least squares fits as described in section 3.4.4. The results are summarized at the end of the section in table II.

Comments on the individual samples.

x=.13

This was a stage 2 sample. There is a slightly larger than usual uncertainty in the value of x for this sample (x=.13±.01). This is because of a problem during the discharge of the cell. For a time of about 1 day near the end of the discharge, the coulometer was not connected and the cell current was not integrated. The x

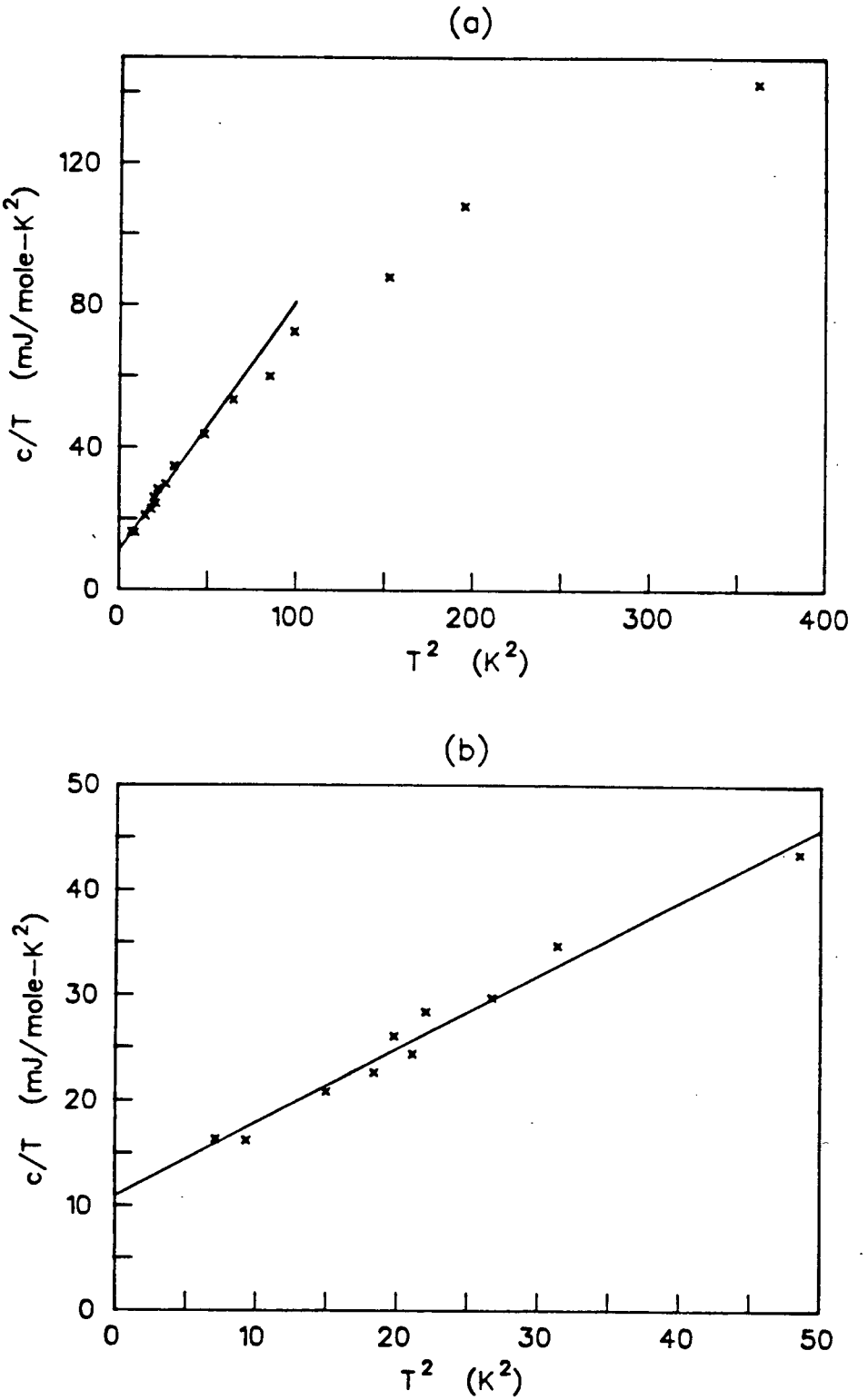

Figure 22: a- Specific heat of $Li_{.13}NbS_2$.
b- Detail below 7.1 K.
The line is the fit described in the text.

value was obtained, with the accuracy stated above, by estimating the lost charge. This same x value is obtained in other cells discharged to the same voltage. The specific heat (figure 22) was measured using the thermocouple sample thermometer and 8 bit A/D, which is the reason for the large scatter in the data. The least squares fit to determine γ and β uses the data between 2.67 and 7K.

x=.16

This sample was also stage 2. Note the large slope of the c/T vs T^2 plot, and the relatively low temperature ($\simeq$7K) at which the specific heat begins to deviate from its cubic behavior (figure 23). The small superleak mentioned in section 3.4.3 was present in this run. The four points at lowest temperature were taken with the bath superfluid, and therefore with a high residual gas pressure in the cryostat. Because of this, they contain a large positive systematic error, and their deviation from the line is not considered significant. They were not used in the fit made to determine γ and β, which extends from 2.73 to 7K.

x=.23

This and all remaining samples are stage 1. The specific heat jump at 3.1K is due to a superconducting transition (figure 24). A fit from 3.2 to 7K was used to determine γ and β.

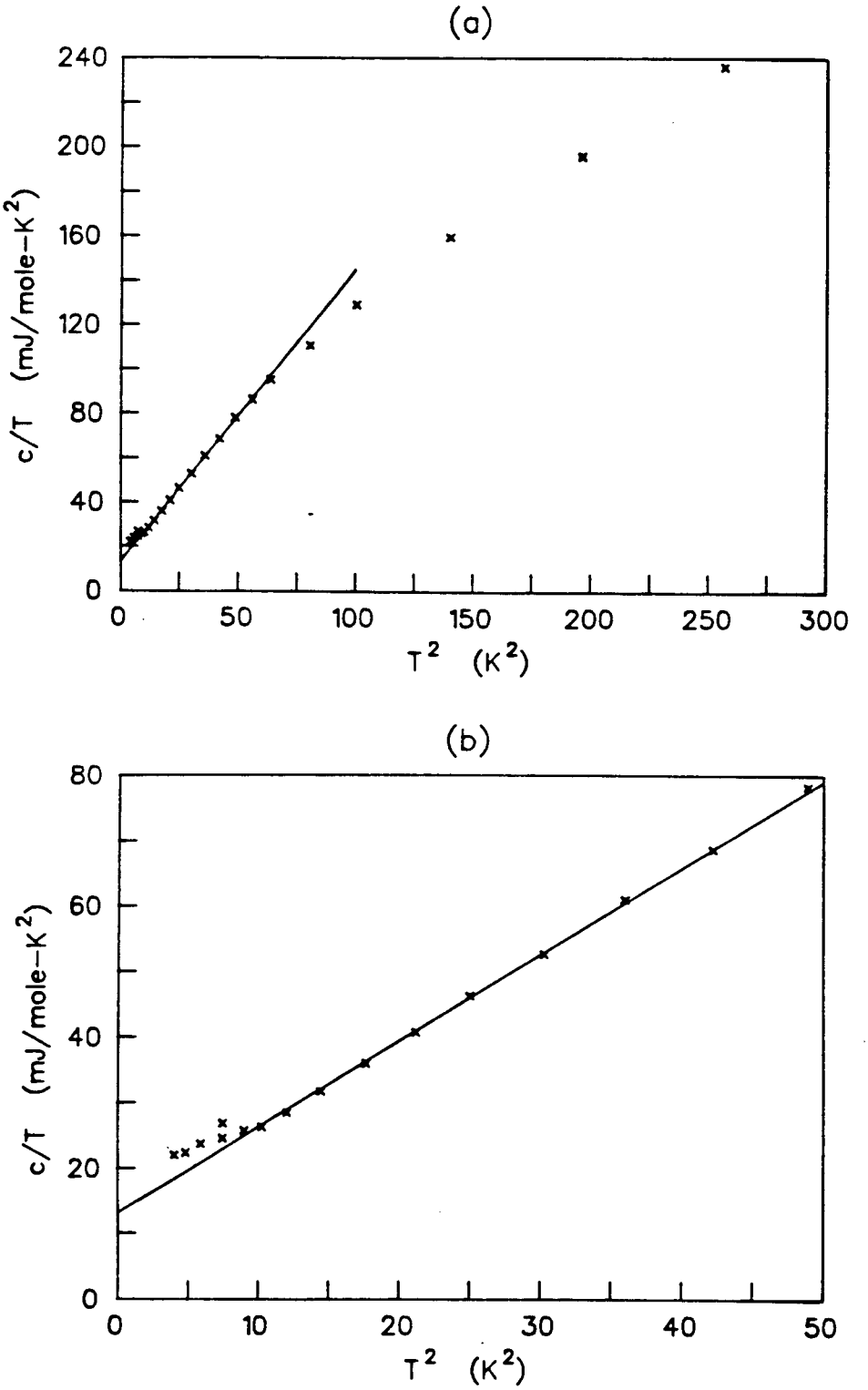

Figure 23: a- Specific heat of $Li_{.16}NbS_2$.
b- Detail below 7.1 K.

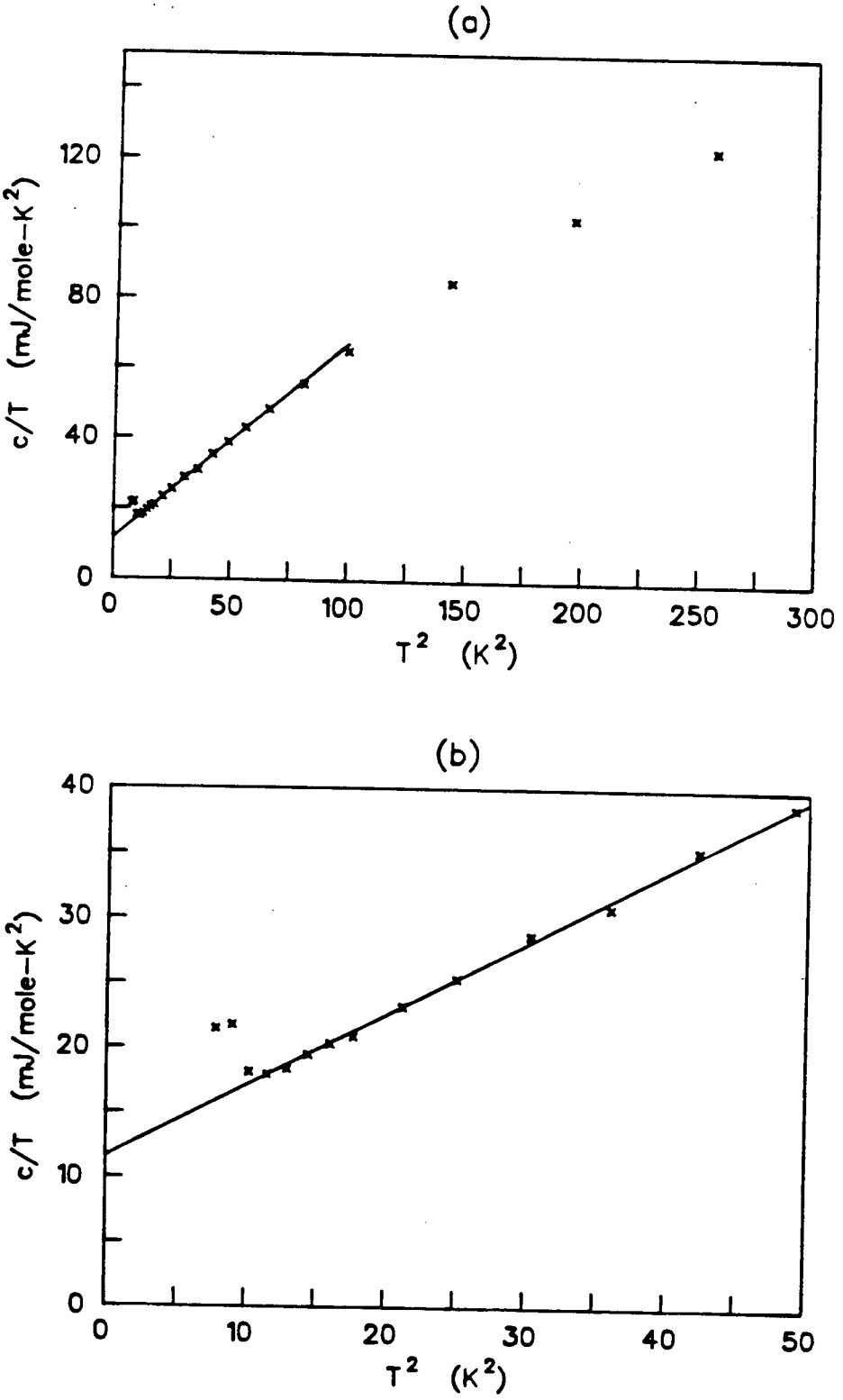

Figure 24: a- Specific heat of $Li_{.23}NbS_2$.
b- Detail below 7.1 K.
A superconducting transition is seen at 3.1 K.

x=.25

This sample was measured using the thermocouple and 8 bit converter, and the data is therefore of rather poor quality (figure 25). There is a superconducting transition at 3.1K. That the specific heat anomaly is truly due to superconductivity was confirmed by a magnetic susceptibility measurement to be described in chapter 7. This was performed on a small piece of the specific heat sample, which was broken off (in the glovebox) after the specific heat measurement.

x=.30

Here again the 4 lowest temperature points were taken with the superleak present. The apparent rise in specific heat below 2.8K (figure 26) is not significant. γ and β were determined from a fit between 2.8 and 6K. This sample has an unusually high β value. The discharge of the cell used to prepare this sample was unusual. It was held at 2.730V (in the stage 2 voltage range) for 3 days, then the voltage was lowered to 2.670V and final equilibration took place.

x=.32

This was intended as a repeat of the x=.30 run. The x=.30 and .32 samples were both prepared by discharging cells to the same voltage (2.670V). The reason for the 8% difference in x is not completely clear. It is possible that it is related to the unusual mode of discharge of the x=.30 cell. If part of the cathode

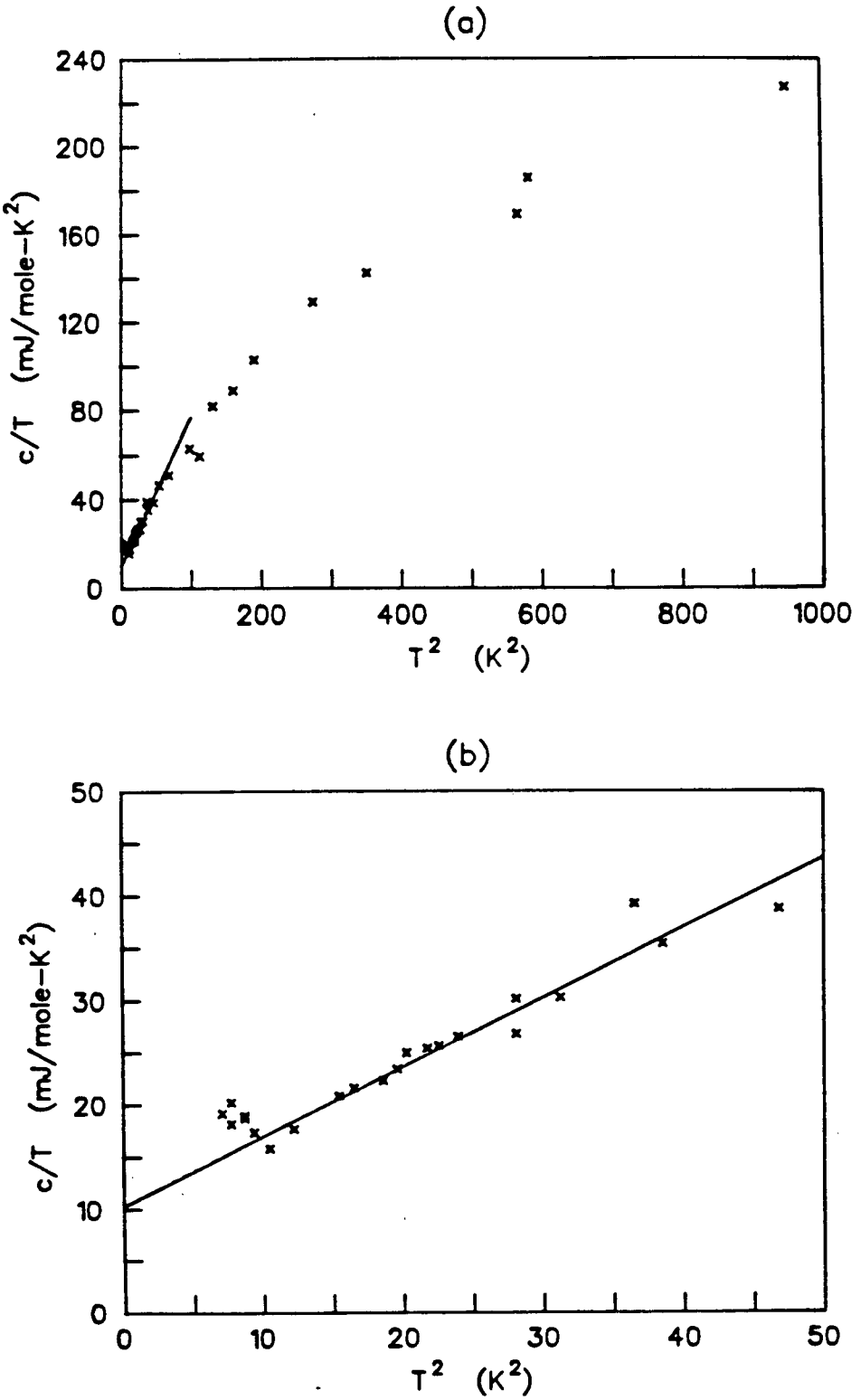

Figure 25: a- Specific heat of $Li_{.25}NbS_2$.
b- Detail below 7.1 K.
There is a superconducting transition at 3.1 K.

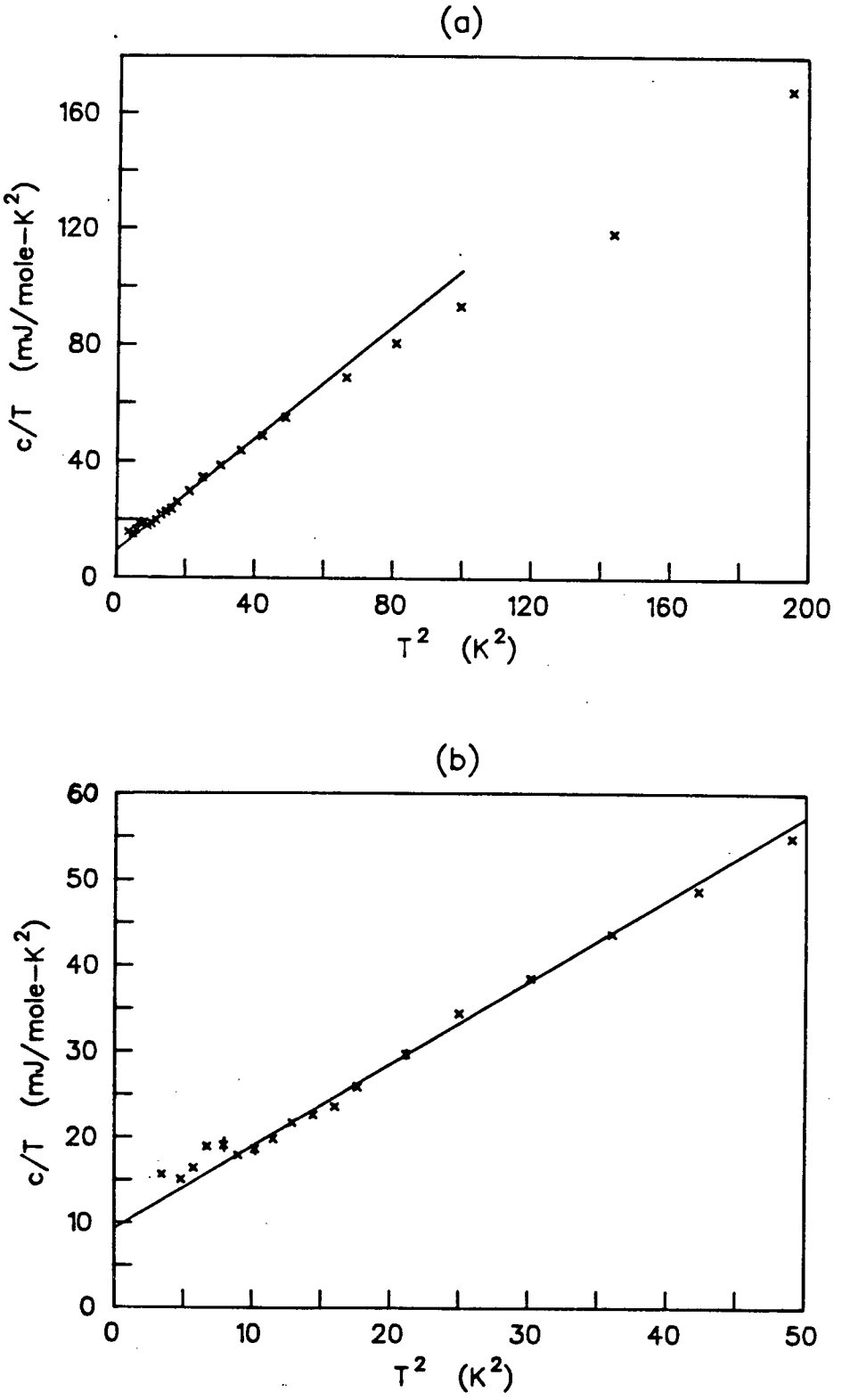

Figure 26: a- Specific heat of $Li_{.30}NbS_2$.
b- Detail below 7.1 K.

material became disconnected while the cell was at 2.730V, it would have been 'left behind' in the stage 2 phase, resulting in the lower overall x value. X-ray diffraction measurements were performed on both the x=.30 and .32 samples, however, and neither one shows any stage 2 Li_xNbS_2, or NbS_2 Bragg peaks. If the x=.30 sample contains more than a few percent of stage 2, it must be either highly disordered or in the form of very fine particles (≃100A or less). Another possible reason for the different x values is the difference in electrochemical behavior in this region between 'fresh and 'aged' NbS_2 (section 2.3).

The specific heat results for the x=.32 sample are shown in figure 27. A fit from 2.8 to 7K was used to determine γ and β.

x=.35

This sample was prepared and measured by D.Li using the author's apparatus. Good specific heat data are available only between 2.8 and 7K (figure 28). All of the data were fit to determine γ and β.

x=.41

This was the first sample measured using the resistor sample thermometer. Rather than the 4 terminal bridge of section 3.3.3, a simple 2 terminal AC Wheatstone bridge was used to measure the thermometer resistance. The detector was a PAR 129 lockin amplifier. This arrangement was noisier than the 4 terminal bridge used

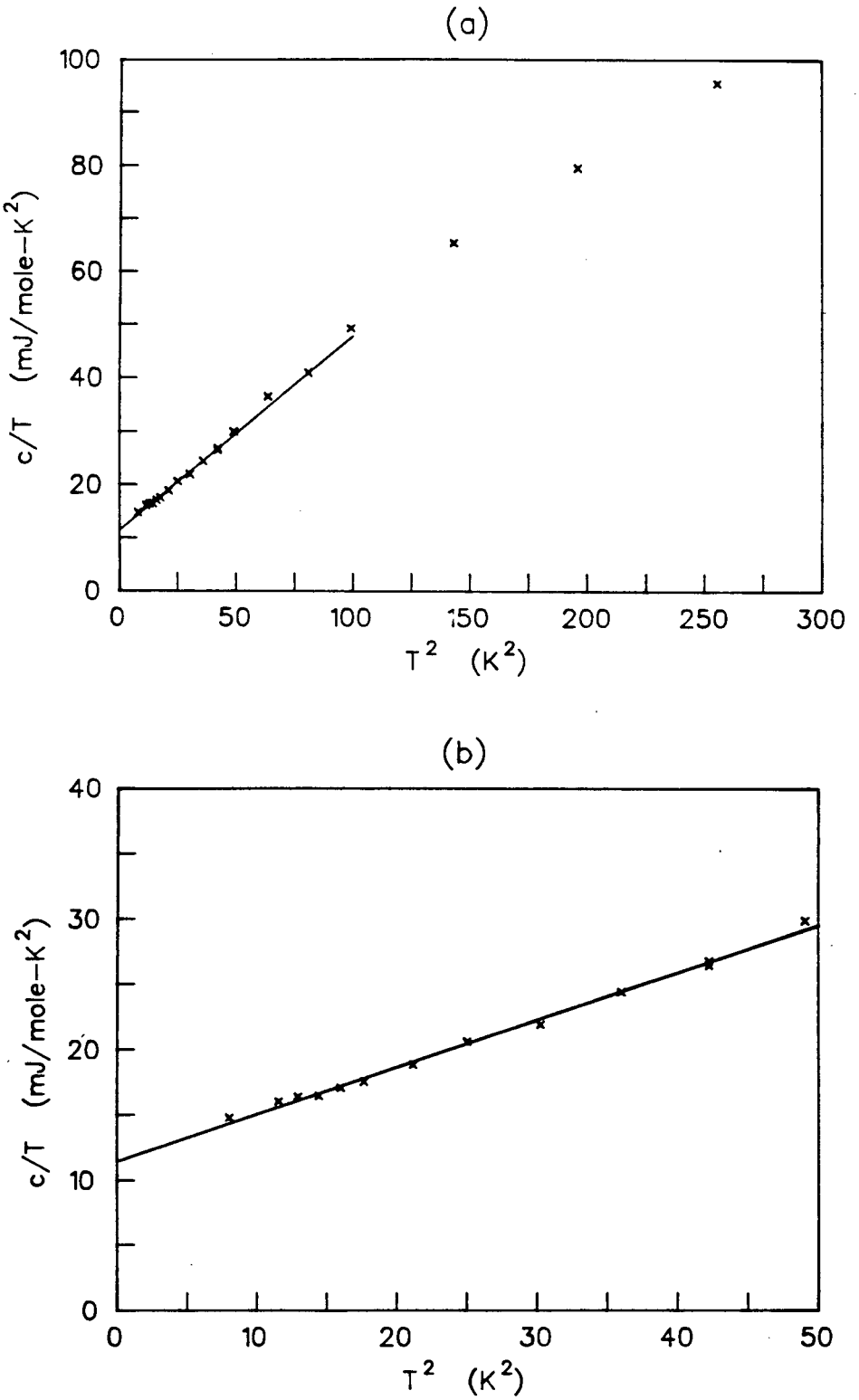

Figure 27: a- Specific heat of $Li_{.32}NbS_2$.
b- Detail below 7.1 K.

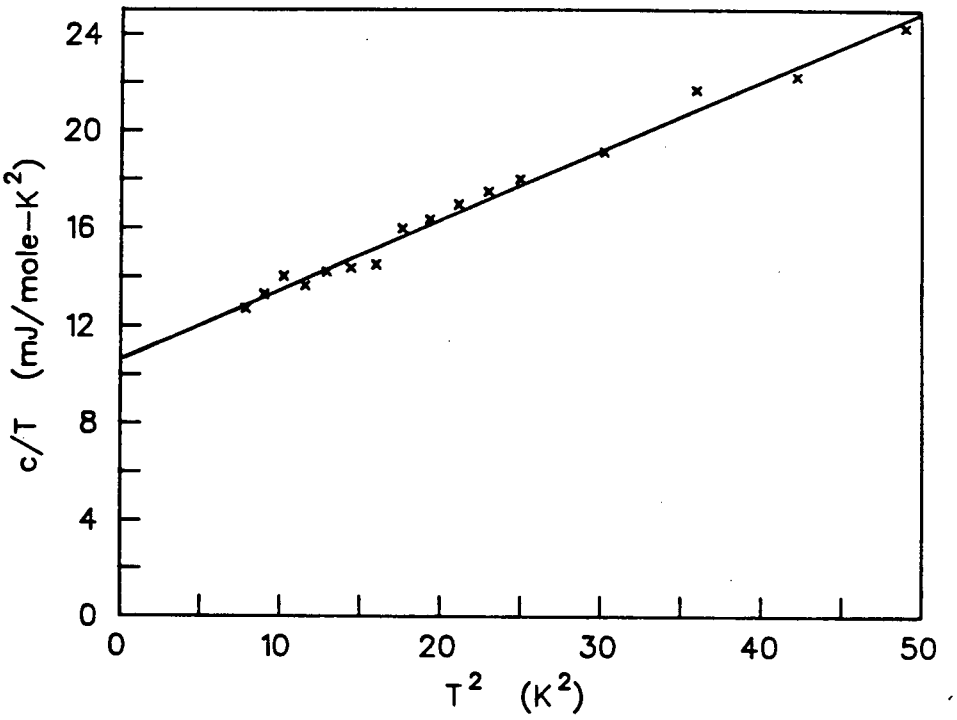

Figure 28: Specific heat of $Li_{.35}NbS_2$.

in later measurements, and this is reflected in the scatter in the data (figure 29). A fit from 2.6 to 7.5K was used to determine γ and β.

x=.50

The specific heat data are shown in figure 30. A fit between 2.8 and 8K was used to determine γ and β.

x=.68

These data were taken using the thermocouple sample thermometer and 8 bit converter (figure 31). γ and β were found using a fit between 2.8 and 8.2K.

x=1.00

The results are shown in figure 32. The interpretation of these data is complicated by the fact that the sample had a very low thermal conductivity, which resulted in large systematic errors below about 6K. The low conductivity caused the thermal decays to be highly non-exponential, as shown in figure 33 for the 2.73K measurement. As discussed in section 3.4.2, the difference $\theta(t)$ between the sample and reference block temperatures should decay according to

$$\theta(t) = \sum_{n=1}^{\infty} \theta_n e^{-t/\tau_n} \qquad (4\text{-}13)$$

Values of τ_1 and θ_1/θ_0 determined from a fit to the data are used to calculate the specific heat. Since $\tau_{n>1} << \tau_1$, simply dropping the first few data points is sufficient to isolate the n=1 term in (3-12). For this measurement, however, θ_1/θ_0=.13, and by the time the n=1 term is

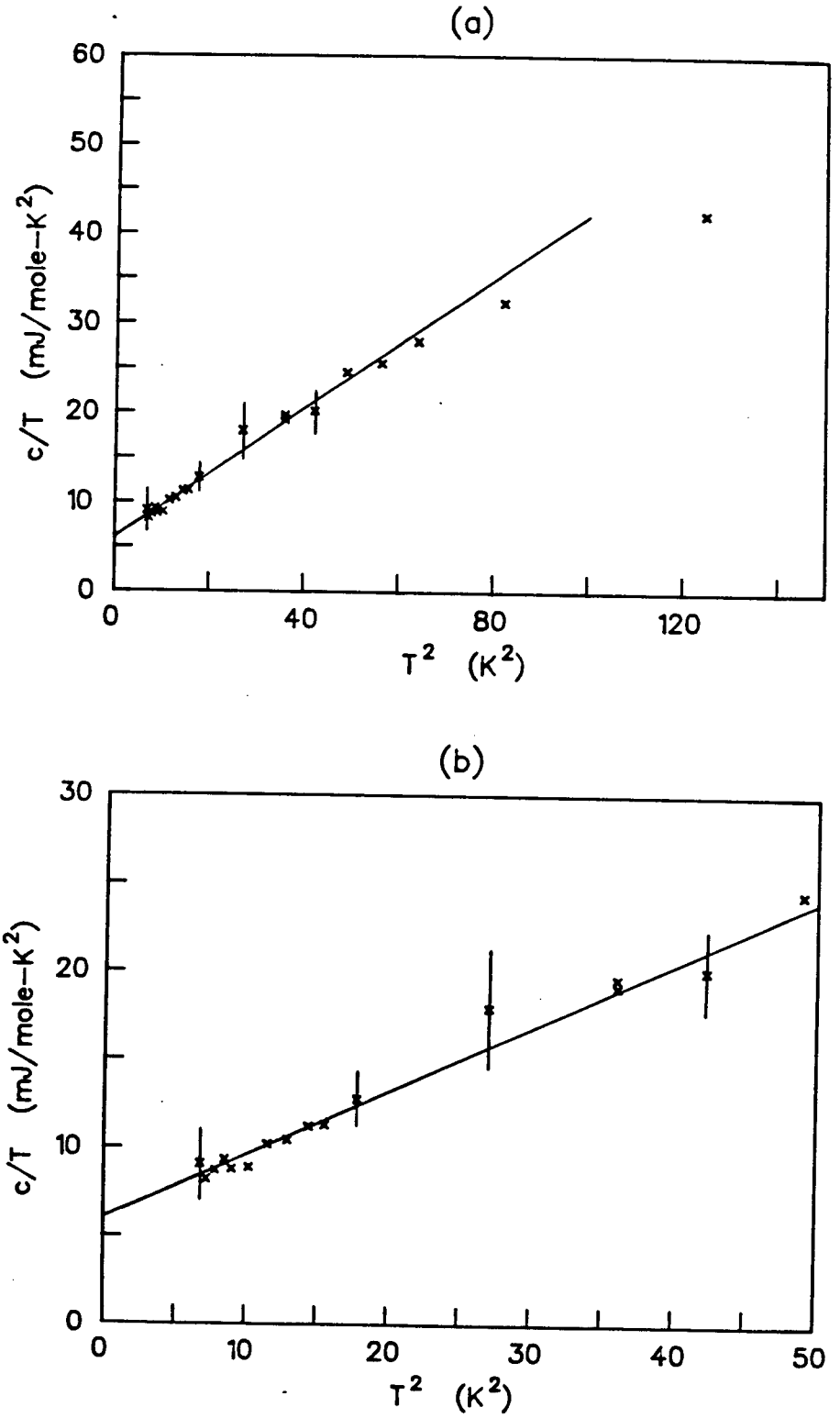

Figure 29: a- Specific heat of $Li_{.41}NbS_2$.
b- Detail below 7.1 K.

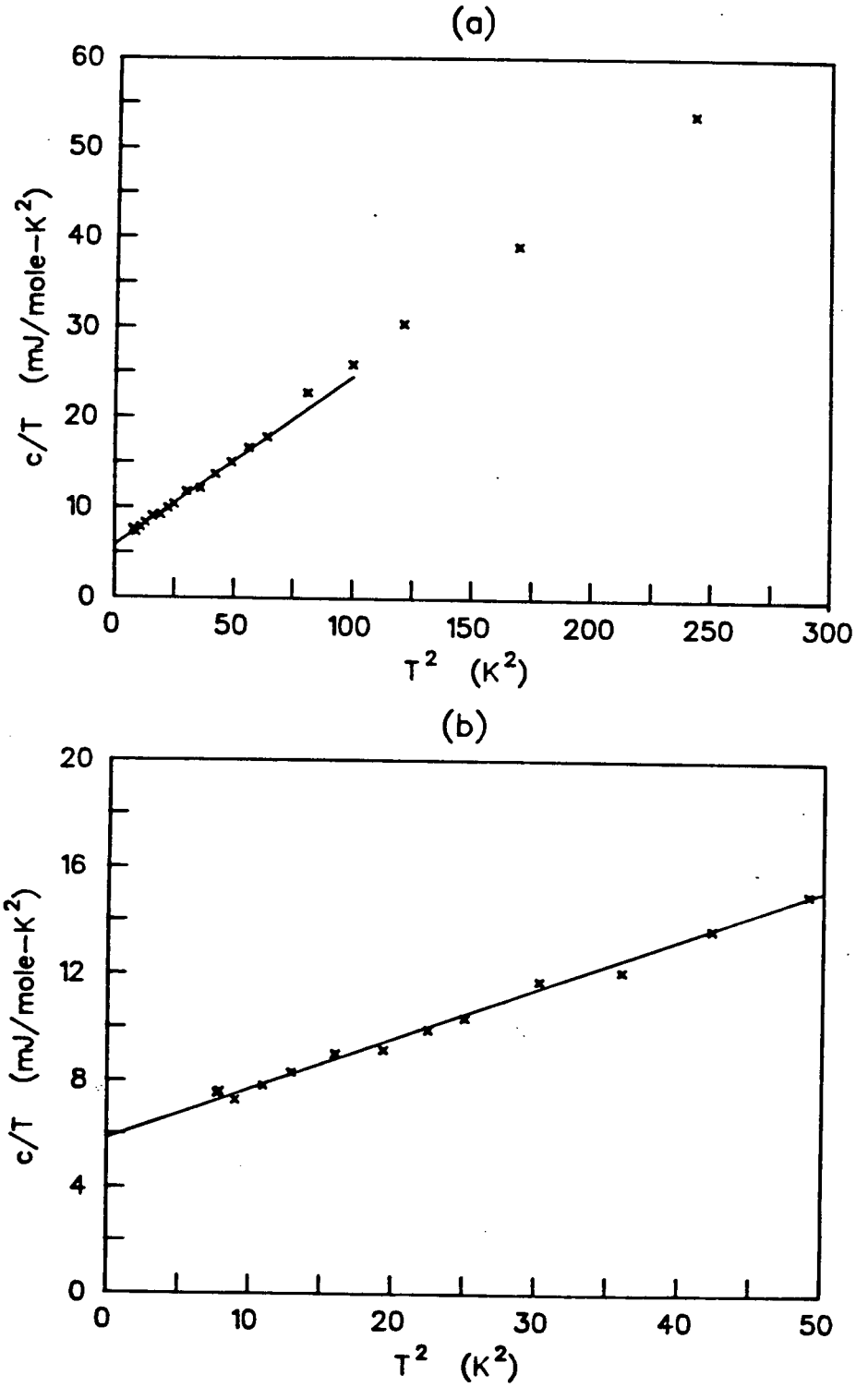

Figure 30: a- Specific heat of $Li_{.50}NbS_2$.
b- Detail below 7.1 K.

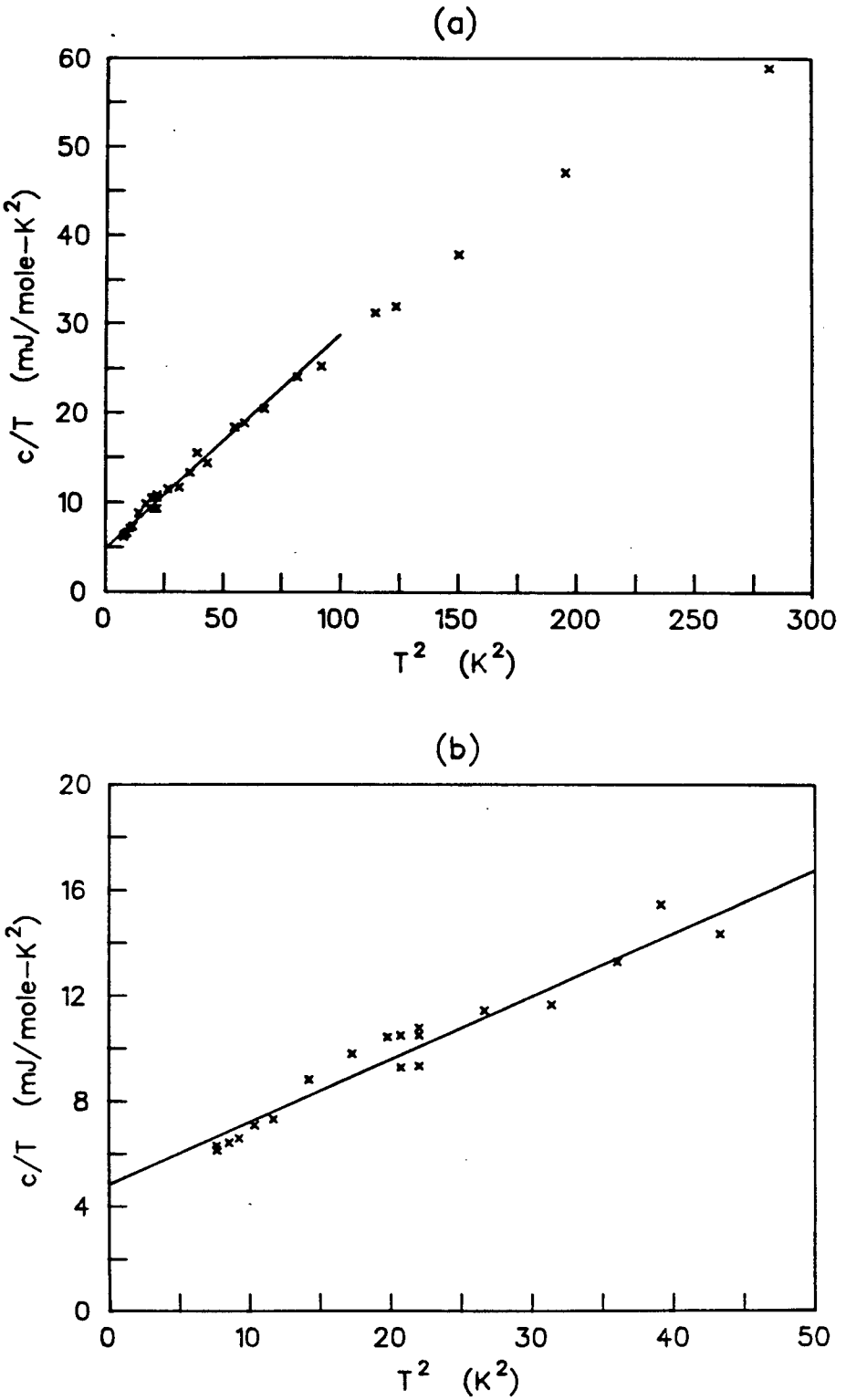

Figure 31: a- Specific heat of $Li_{.68}NbS_2$.
b- Detail below 7.1 K.

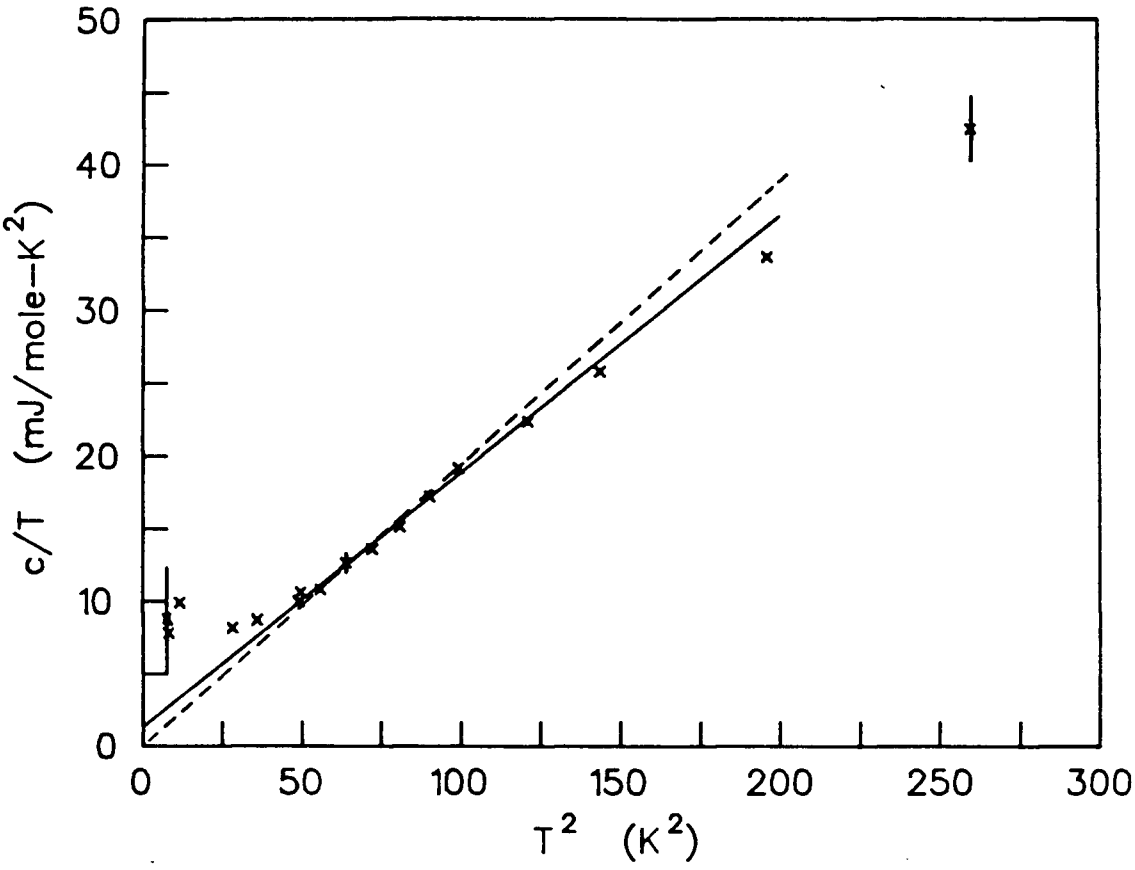

Figure 32: The specific heat of $Li_{1.00}NbS_2$. The solid line is the result of a least squares fit between 7 and 10 K. The dashed line shows that the data are also consistent with $\gamma=0$ (see text). A large, positive systematic error is present at the lower temperatures, due to the unusually low thermal conductivity of this sample.

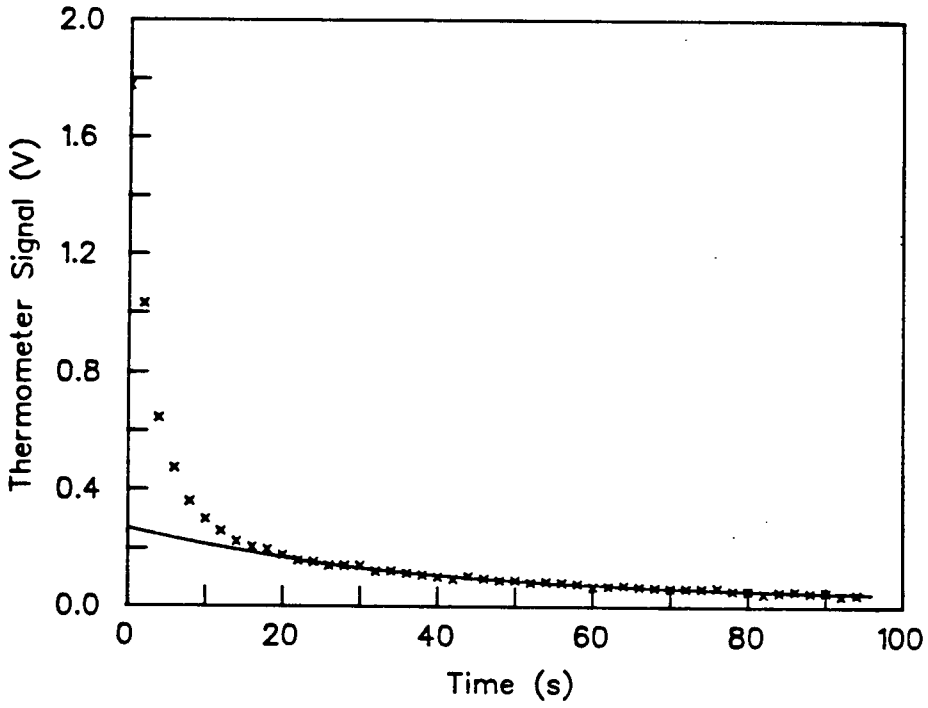

Figure 33: Thermal decay of the $Li_{1.00}NbS_2$ sample at 2.73K (see text). The maximum thermometer signal of 1.8V corresponds to a temperature difference θ_0=19mK.

isolated the signal level is only about 5 times the noise. (Measurements on all other samples had $.5 \leq \theta_1/\theta_0 \leq 1.$) As a result, the uncertainties in the fitted parameters θ_1 and τ_1 are unusually large for this sample, resulting in a large random error in the specific heat (±40%). In addition, a low thermal conductivity sample will enhance the systematic error due to residual gas. Because of this, the apparent upturn in the specific heat below 6K is not believed to be significant. At 7K and above, the sample's thermal conductivity was high enough that accurate specific heat measurements could be made. (For example, at 8K, $\theta_1/\theta_0 = .9$)

The coefficients γ and β as determined from a fit to the data between 7 and 10K, are 1.3mJ/mole-K^2 and .18mJ/mole-K^4, respectively. This fit is shown as the solid line in figure 32. The data are also consistent with $\gamma=0$, and $\beta=.19$mJ/mole-K^4 (the dashed line). The rigid band charge transfer model (section 1.3) predicts $\gamma=0$ for this sample, since the dz^2 band should be full, and the sample should be a semiconductor. The low, strongly temperature dependent thermal conductivity is also consistent with a semiconducting sample.

No superconducting transition or other specific heat anomalies were observed in this sample, although because of the poor quality of the data below 6K, it would have been difficult to observe such an anomaly

even if it did occur. There is no reason to expect Li_1NbS_2 to be a superconductor.

If more accurate measurements of the specific heat of Li_1NbS_2 are ever required, they could perhaps be made by mixing the powder sample with a known amount of a thermal contact agent such as vacuum grease. Because of the high reactivity of the samples, the chemical compatibility of the contact agent with lithium would have to be checked.

The values of γ and β for all the samples are listed in table II. The table also contains details of the sample preparation conditions, the sample masses, and the masses of Cry-Con grease used to attach the samples. γ and β are shown as functions of x in figures 34 and 35, respectively. The interpretation of these results is the subject of the following three chapters.

Table II

Specific Heat results for Li_xNbS_2 samples

The table includes x, the equilibrium voltages of the electrochemical cells used to prepare the samples, the masses of the samples and the grease used to mount them, the specific heat coefficients γ and β, and the superconducting transition temperature, T_c. Where no T_c was observed, T_c is shown as being lower than the lowest temperature at which measurements were made.

x	stage	cell voltage (V)	NbS_2 batch	sample mass (mg)	grease mass (mg)	$\gamma(\frac{mJ}{mole\text{-}K^2})$	$\beta(\frac{mJ}{mole\text{-}K^4})$	T_c (K)
0	-	-	DD9	231	4.8	19.3±1.5	0.31±0.04	5.7
.13±.01	2	2.760	DD9	124	3	$10.9^{+1.0}_{-1.4}$	0.70±0.06	<2.7
.16	2	2.755	DD12	111	5	$13.1^{+0.5}_{-1.5}$	$1.32^{+.05}_{-.02}$	<2.0
.23	1	2.710	DD12	117	3	$11.6^{+0.4}_{-1.0}$	$0.55^{+.03}_{-.01}$	3.1
.25	1	2.707	DD9	106	1.5	$10.3^{+1.0}_{-1.4}$	$0.66^{+.05}_{-.03}$	3.1
.30	1	2.670	DD12	117	6	$9.4^{+0.6}_{-1.6}$	$0.96^{+.06}_{-.04}$	<1.8
.32	1	2.670	DD12	98	7	$11.4^{+0.3}_{-1.0}$	$0.36^{+.03}_{-.01}$	<2.8
.35	1	2.640	DD12	129	7	$10.6^{+0.3}_{-1.0}$	$0.29^{+.03}_{-.01}$	<2.8
.41	1	2.600	DD9	143	6	6.0±0.3	0.36±0.01	<2.6
.50	1	2.500	DD12	103	2	5.8±0.2	0.187±.005	<2.8
.68	1	2.350	DD9	201	2.8	4.8±0.3	0.24±.01	<2.8
1.00	1	1.900	DD9	155	4	$1.3^{+1.0}_{-1.3}$	0.18±.01	none observed

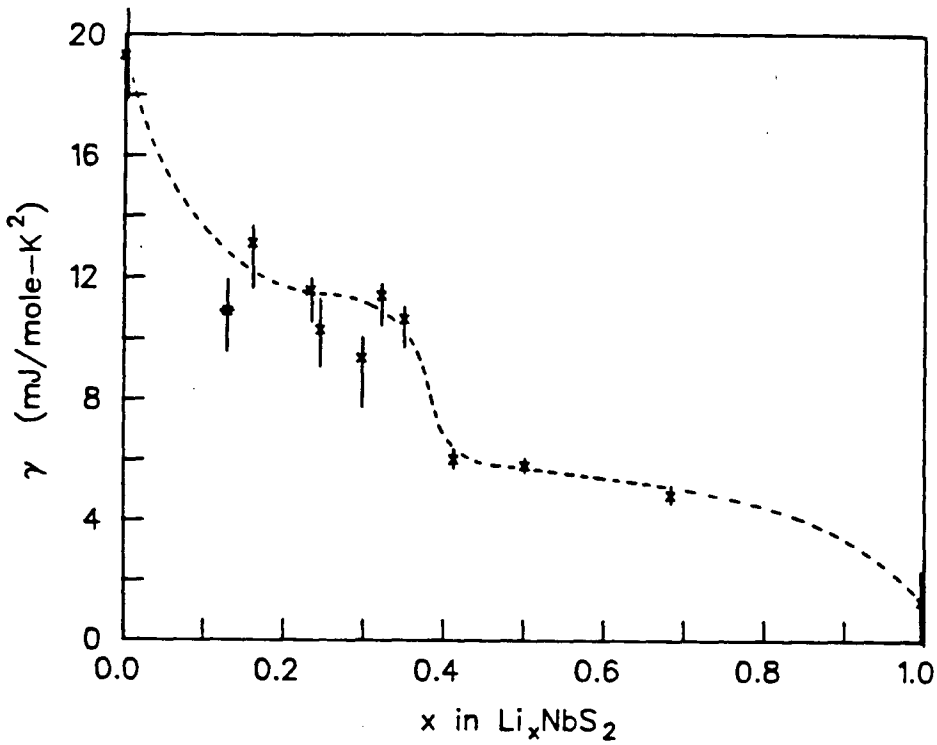

Figure 34: The linear specific heat coefficient γ as a function of x for the Li_xNbS_2 samples. The dashed line is intended only as a guide for the eye.

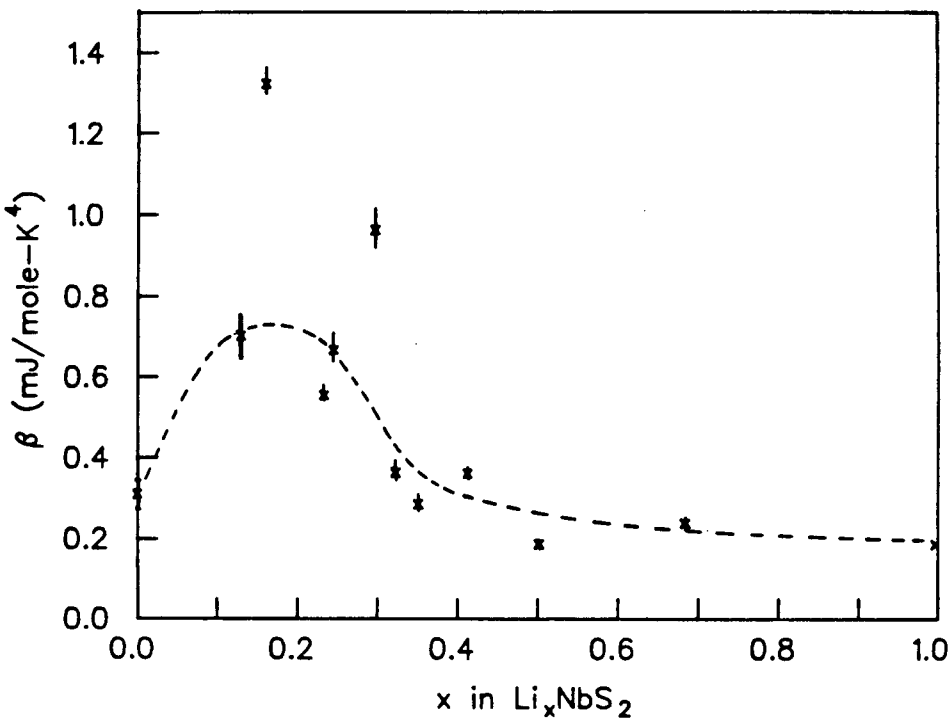

Figure 35: The cubic specific heat coefficient β as a function of x for the Li_xNbS_2 samples. The dashed line is provided only to guide the eye.

5. THE ELECTRONIC SPECIFIC HEAT

5.1 INTRODUCTION

This chapter begins with a short introduction to the theory of the electronic specific heat of metals. In section 5.3, the effect of intercalation on the electronic specific heat is discussed in terms of the rigid band charge transfer model. The electronic density of states calculated by Doran et al. (1978) is used to predict the electronic specific heat of Li_xNbS_2 as a function of x. The theoretical predictions are compared with the data in section 5.4.

In disordered systems, it is possible for there to be a linear term in the low temperature specific heat which is not of electronic origin (Anderson et al. 1972). In a disordered solid such as a glass, some atoms or groups of atoms may be in positions were they have access to two closely separated potential energy minima. A distribution of these 'tunneling states' is responsible for the linear specific heat. The magnitude of this linear term is generally rather small. Typical glasses have linear specific heats which are of order 100 times smaller than the electronic specific heats of metals such as Li_xNbS_2 (Hunklinger et al. 1975, for example). There is disorder in Li_xNbS_2, most significantly that due to the arrangement of the lithium atoms in the interlayer sites. As is discussed further in sections 6.2 and 6.6.1, the lithium is believed to lie on the octahedral sites in the interlayer gaps, and

for most values of x is distributed at random among these sites. The lithium-lithium interaction is believed to be small compared to the energy required for a lithium atom to hop from one site to the next. Therefore, in spite of the disorder, lithium atoms (except perhaps a few near defects, or possibly at phase boundaries or domain walls if these exist) should be in deep, single potential energy minima. The linear specific heat due to lattice disorder is probably much smaller than in glasses, and we can be reasonably sure that the measured linear specific heat is electronic in origin.

5.2 THE ELECTRONIC SPECIFIC HEAT OF A METAL

Consider a system of independent electrons with a density of states in energy given by $N(\epsilon)$. At temperature T, the occupation of these states is given by the Fermi-Dirac distribution

$$f(\varepsilon) = \frac{1}{e^{(\varepsilon-\mu)/k_B T} - 1} \qquad (5\text{-}1)$$

where μ is the chemical potential of the electrons. The total electronic energy at temperature T is therefore given by

$$U = \int_{-\infty}^{\infty} \epsilon N(\epsilon) f(\epsilon) d\epsilon \qquad (5\text{-}2)$$

From this, it is possible to derive the well known expression for the electronic specific heat of a metal (see,

for example, Ashcroft and Mermin 1976, chapter 2).

$$c_{el}=(\partial U/\partial T)_n=(\pi^2/3)k_B{}^2TN(\epsilon_F) \qquad (5\text{-}3)$$

where ϵ_F is the Fermi energy.

In a real metal, this must be corrected for the electron-phonon interaction. Instead of (5-3) we have

$$c_{el}=(1+\lambda)(\pi^2/3)k_B{}^2TN(\epsilon_F) \qquad (5\text{-}4)$$

where λ is the electron-phonon coupling constant[22]. The linear specific heat coefficient γ (see equation 1-3) is

$$\gamma=(1+\lambda)(\pi^2/3)k_B{}^2N(\epsilon_F) \qquad (5\text{-}5)$$

5.3 THE ELECTRONIC SPECIFIC HEAT IN THE RIGID BAND CHARGE TRANSFER MODEL

An introductory discussion of the rigid band charge transfer (RBCT) model has been given in section 1-3. As was mentioned there, the Fermi level in NbS_2 lies in the center of the half-filled dz^2 band. According to RBCT, as x is increased in Li_xNbS_2, the electrons donated by the intercalated lithium progressively fill the band, until it is completely full at x=1. As x increases, ϵ_F moves up through the dz^2 band, and $N(\epsilon_F)$ changes, eventually falling to zero at x=1. Although λ may also change on intercalation, the dominant factor affecting the electronic specific heat is expected to be $N(\epsilon_F)$. The behavior of the electronic specific heat coefficient γ should therefore directly reflect the

---

[22] This is also called the mass enhancement factor.

structure of the dz^2 band density of states. In this section, a calculated density of states is used with RBCT to predict $\gamma(x)$.

Wexler and Wooley (1976) made band structure calculations for NbS_2 and several other layered compounds using the layer method. The results are in reasonable agreement with those calculated for some of the layered compounds (but not for NbS_2) by Mattheis (1973), who used an augmented plane wave method. Doran et al. (1978) made a tight-binding fit to Wexler and Wooley's bands and used this to calculate the density of states of NbS_2. The fit to the bands is shown in figure 36. The labels on the horizontal axis of figure 36 refer to points of high symmetry in the hexagonal Brillouin zone (figure 37). Figure 38 shows the calculated density of states for the dz^2 band. The density of states given by Doran et al., has been multiplied by two to account for electron spin, and the energies have been converted from Rydberg units to electron volts (1 Ryd=13.6eV).

Some comments should be made at this point. The weak splitting of the two dz^2 sub-bands disappears at the top face of the Brillouin zone (the plane containing A,H,and L in figure 37). This is due to the same symmetry of the unit cell which causes the geometrical structure factor of $(00l)$ Bragg peaks to be zero for l odd (section 2.3, appendix 1). Because of this, the Fermi surface can be 'unfolded' into a doubled zone, as is done in figure 37. In stage two Li_xNbS_2

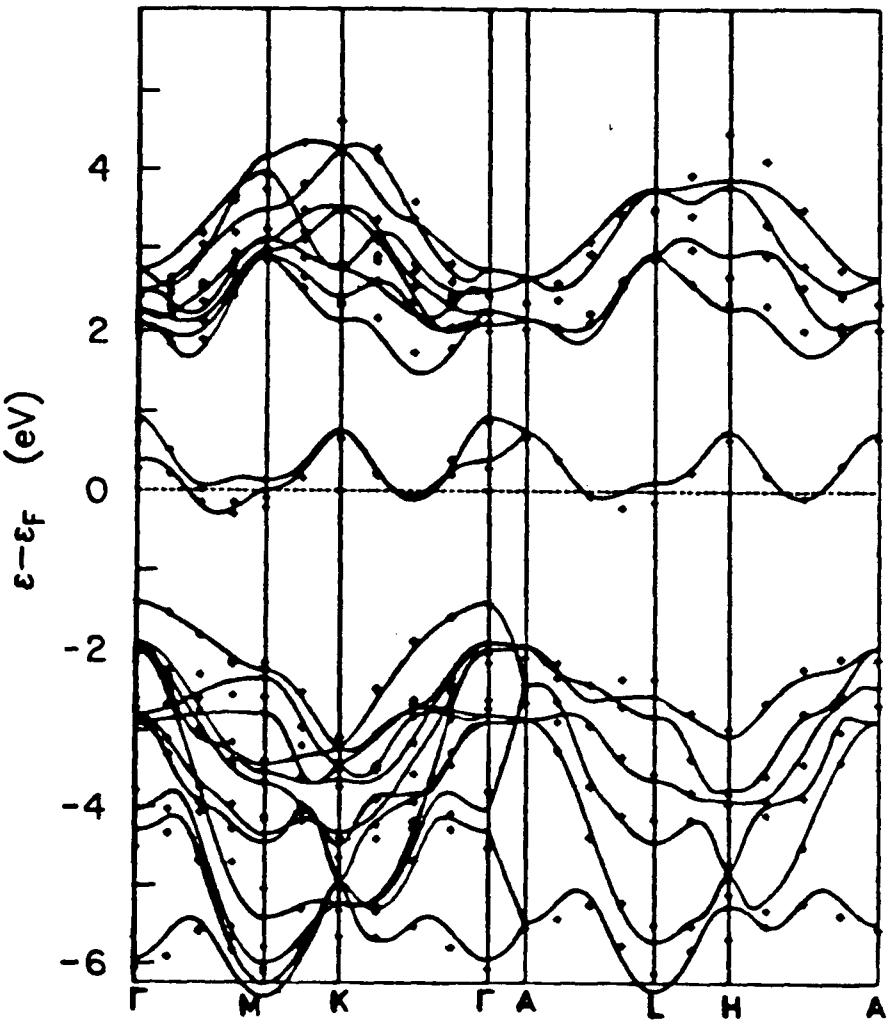

Figure 36: Tight-binding fit (Doran et al.1978) to the layer method band structure of NbS_2. The small crosses represent the layer method results of Wexler and Wooley (1976). A separate fit was used to determine the dz^2 band density of states.

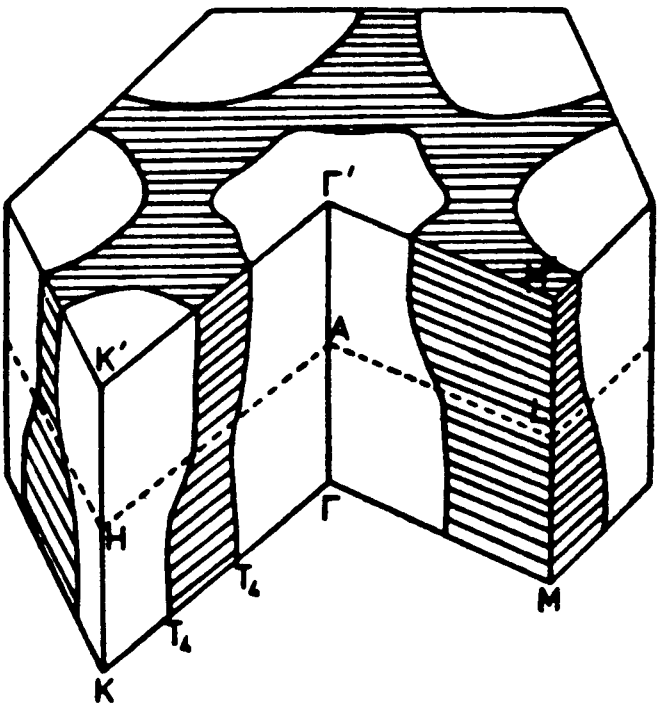

Figure 37: Brillouin zone and Fermi surface of NbS_2. The Fermi surface has been 'unfolded' into a double zone (both Γ and Γ' are the zone center). After Wexler and Wooley (1976).

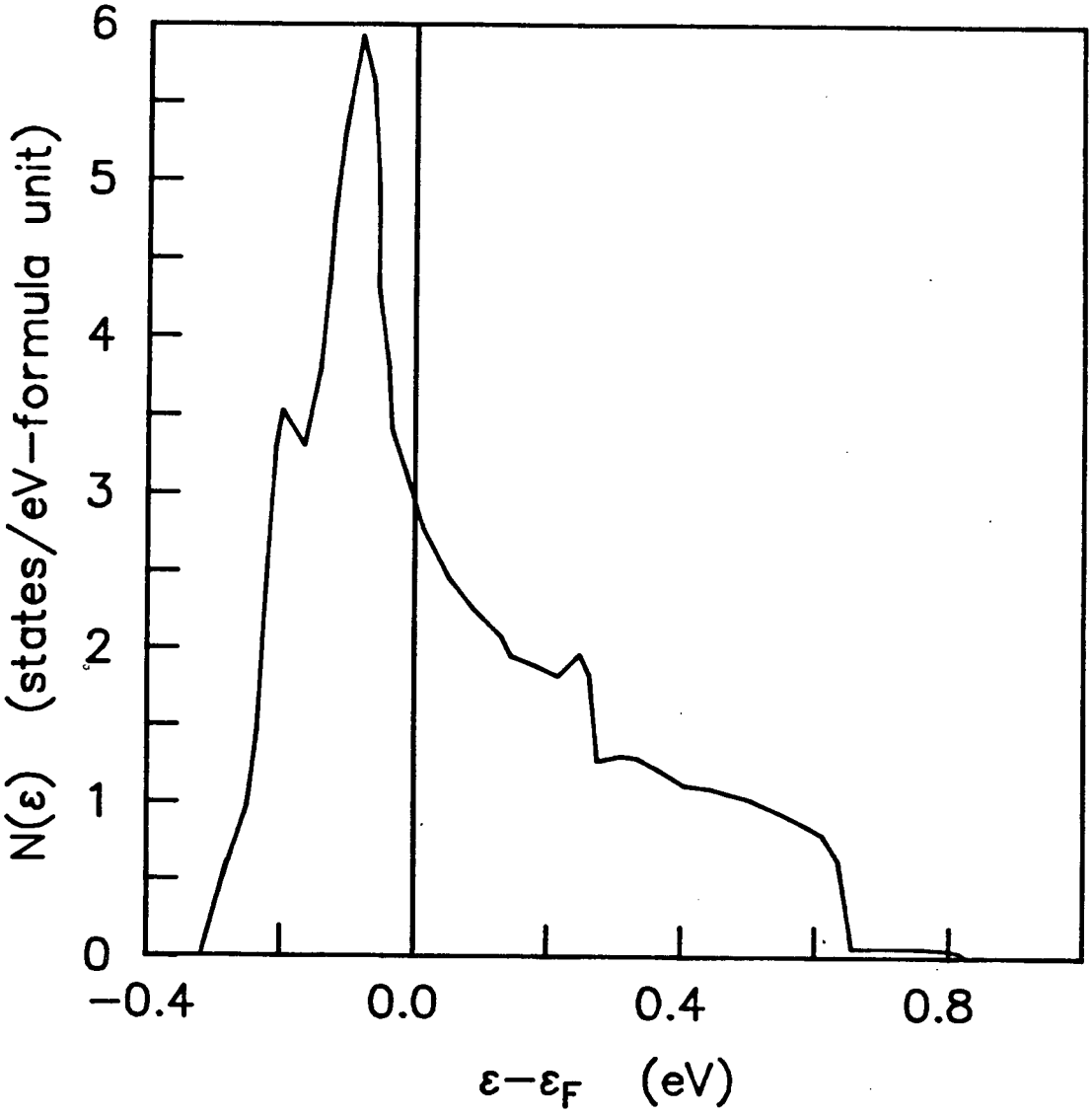

Figure 38: The dz^2 band density of states for NbS_2. (Doran, et al, 1978)

this symmetry disappears, and some sub-band splitting will occur even at the zone boundary. This is the only topological change in the bands to be expected in any of the intercalation compounds, unless lithium ordering occurs. Ordering in the interlayer gaps would result in a larger unit cell and further band splitting, although this splitting would probably be weak. The splitting due to staging is also expected to be weak, since it is due to interlayer interactions, and it should not have a large effect on the density of states.

Another point concerns the shape of the dz^2 band density of states. The Fermi level lies on the side of an extremely sharp peak in the density of states. Because of this, the calculated $N(\epsilon_F)$ should not be considered to be very precise. A slight change in ϵ_F would change $N(\epsilon_F)$ drastically. There is also a 'shoulder' (van Hove singularity) in the density of states at $\epsilon-\epsilon_F$=.27eV. This shoulder is due to the saddle point in the lower sub-band at Γ. Although the exact size and location of the shoulder depend on the details of the calculation, its existence does not.

The next step is to treat Li_xNbS_2 in the RBCT model by adding electrons to the dz^2 band. Consider the Fermi energy to be a function of x. With $N(\epsilon)$ expressed in units of states per unit energy per formula unit, the assumption of complete charge transfer means that

$$x = \int_{\epsilon_F(0)}^{\epsilon_F(x)} N(\epsilon)\, d\epsilon \qquad (5\text{-}6)$$

This integral equation has been used to calculate $N(\epsilon_F(x))$ as a function of x. The results are shown in figure 39. The electronic specific heat coefficient γ is given simply by

$$\gamma(x)=(1+\lambda)(\pi^2/3)k_B{}^2N(\epsilon_F(x)) \qquad (5\text{-}7)$$

5.4 DISCUSSION

To use (5-7) to fit the $\gamma(x)$ data we need, in principle, to know λ as a function of x. Given the lack of any information which would allow the independent determination of λ, we will proceed by making the assumption that it is constant. One way of assigning a numerical value to λ is to use the values of γ and $N(\epsilon_F)$ at x=0. These are 19.3±1.5 mJ/mole-K^2 and 2.94 states/eV-formula unit, respectively, giving λ=1.8 using (5-7). This is in reasonable agreement with the value of 1.94±(10 to 20%) which Aoki et al. (1983) have calculated from NMR relaxation time and specific heat measurements.

The curve obtained by the use of (5-7) and λ=1.8 is shown in figure 40, along with the data. A curve for λ=1.2 is also included. The general features of the data and the calculated curves agree reasonably well. Because of the approximate nature of the band calculations, exact agreement should not be expected anyway. Variations in λ as a function

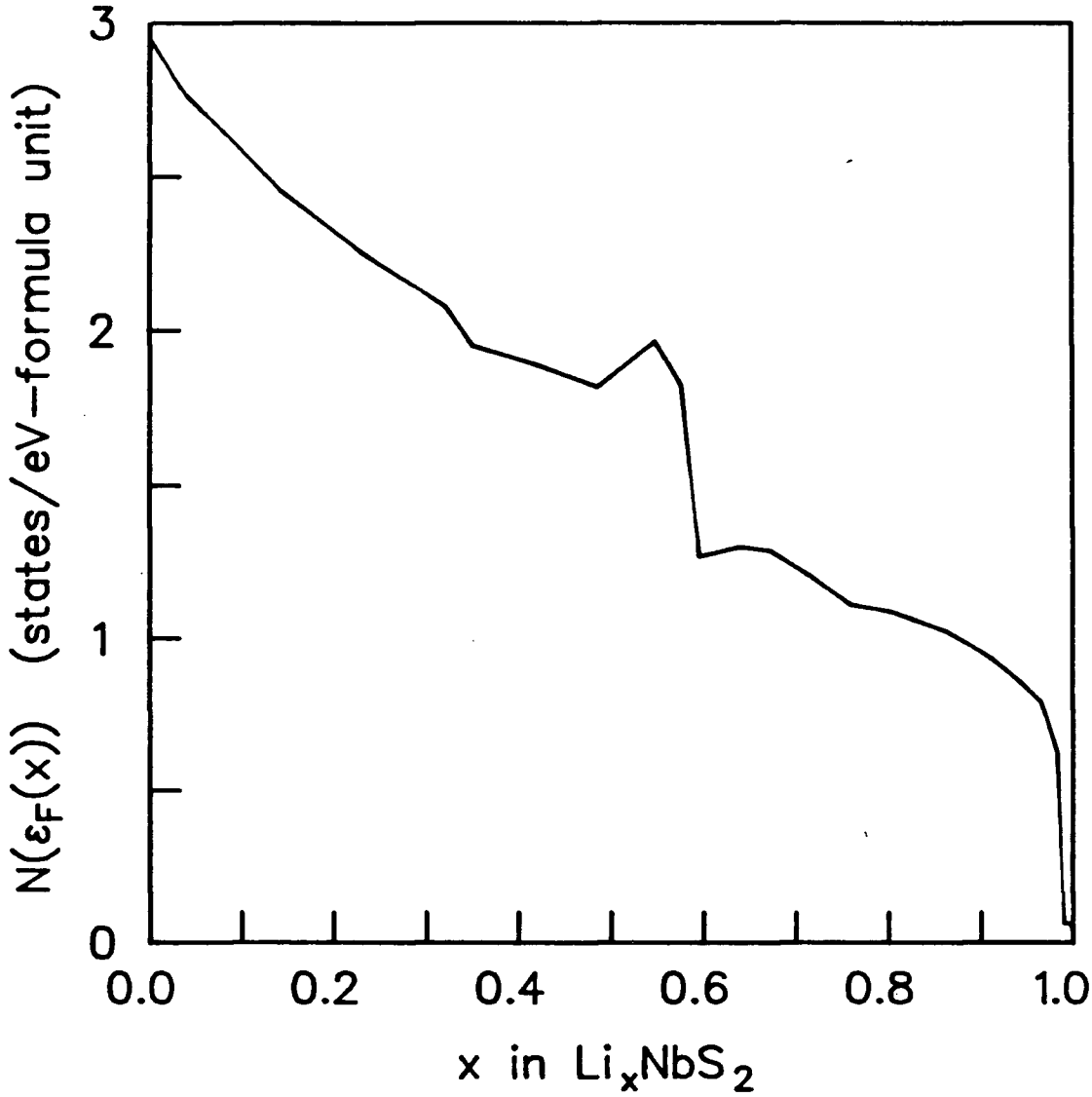

Figure 39: The density of states at the Fermi level of Li_xNbS_2, plotted as a function of x. This curve was calculated using the rigid band charge transfer model and the density of states of Doran et al. (1978).

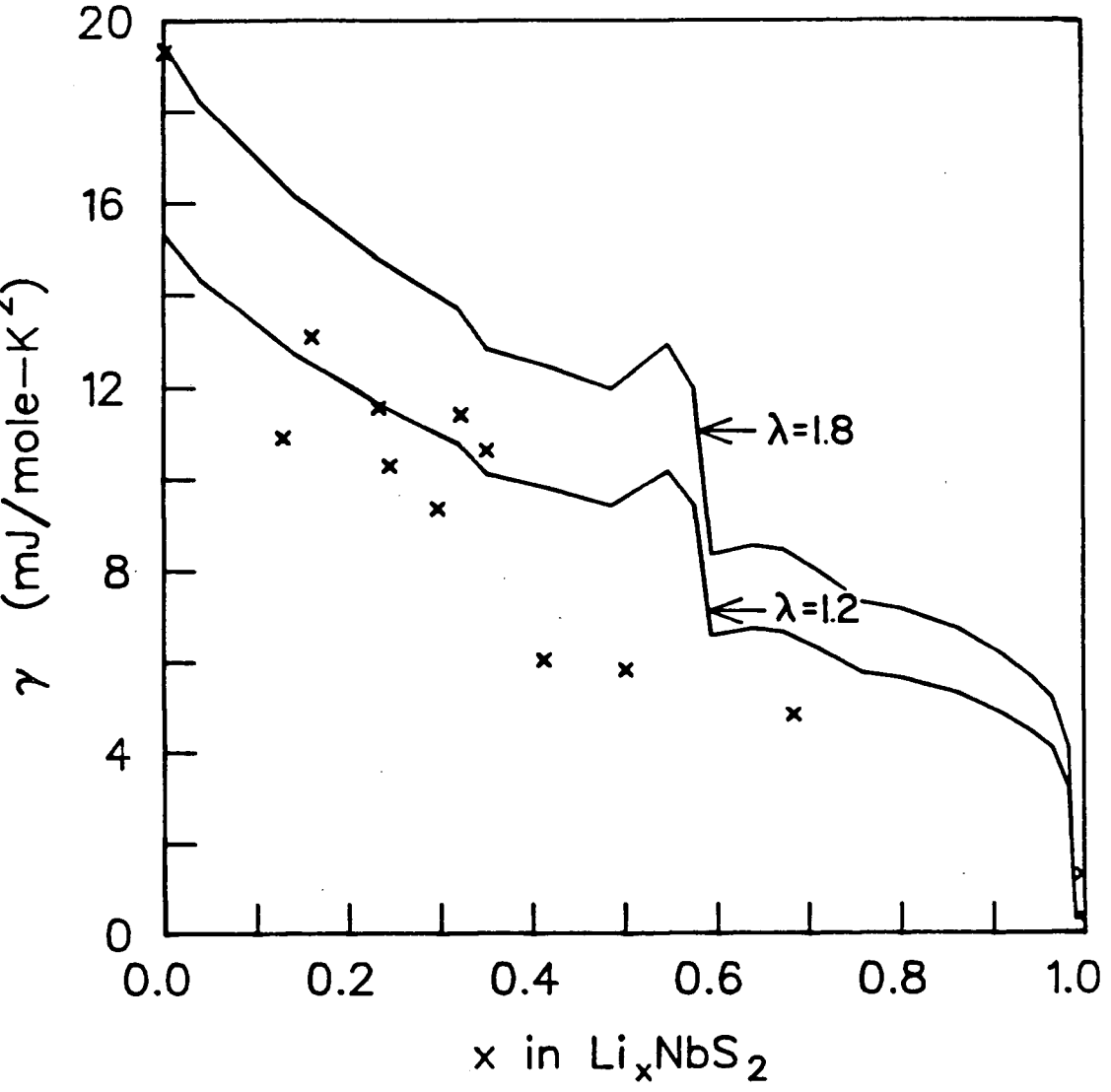

Figure 40: The electronic specific heat coefficient γ as a function of x in Li_xNbS_2. The data are shown (chapter 4), together with the predictions of the rigid band charge transfer calculation for two values of the electron-phonon coupling constant λ (see text).

of x are also possible, and could contribute to the differences between the data and the calculated curves. (As we shall see in Chapter 6, the specific heat data also imply significant changes in the phonon spectra as a function of x.)

Several conclusions can be drawn from the data:

1. γ tends to a value near zero at x=1. This supports the hypothesis of complete charge transfer, that is, each intercalated lithium atom donates one electron to the NbS_2 bands.
2. Use of the dz^2 bands of the NbS_2 host gives reasonable agreement with the Li_xNbS_2 data. There is no evidence that intercalation leads to either major changes in the dz^2 band, or to band overlap in this material.
3. The shoulder in the specific heat data at $x \simeq .4$ indicates that this is the value of x for which the Fermi level of Li_xNbS_2 crosses the saddle point in the Li_xNbS_2 dz^2 band. If we assume a completely rigid band (that is, the Li_xNbS_2 dz^2 band is exactly the same as the NbS_2 dz^2 band), this puts the following constraint on the density of states of NbS_2

$$\int_{\epsilon_F}^{\epsilon_S} N(\epsilon)\, d\epsilon = .4 \text{ states/formula unit.} \qquad (5\text{-}8)$$

Here ϵ_F and ϵ_S are the Fermi energy of NbS_2 and the energy of the saddle point, respectively. Note that this result does not depend on any assumptions concerning λ.

6. THE LATTICE SPECIFIC HEAT

6.1 INTRODUCTION

This chapter is concerned with the specific heat due to lattice vibrations (phonons). The well known fact that the phonon specific heat of a three dimensional solid is proportional to T^3 at sufficiently low temperatures has already been mentioned. The theory which explains this will be briefly reviewed in section 6.3. The T^3 behavior occurs at temperatures so low that only long wavelength acoustic phonons can be thermally excited. Because these are ordinary sound waves, the specific heat can be calculated using continuum elasticity theory. This allows a discussion of the specific heat data in terms of the macroscopic elastic constants of Li_xNbS_2 (section 6.4).

In section 6.5, the question of deviations from T^3 is addressed. The mechanisms which cause these deviations as the temperature is raised are discussed. It is possible to make a rough theoretical estimate of the temperature above which significant deviations from T^3 begin to occur, and this is found to be in agreement with the data.

In section 6.6, we take a different approach which sheds further light on the problem. Simple one dimensional lattice-dynamical models are used to investigate possible effects of lithium intercalation on the elastic behavior. These models are also used to describe the effects of staging. Section 6.7 concludes the chapter.

Before beginning a discussion of the specific heat which includes only vibrational motion, we recall that one of the most important features of Li_xNbS_2 is that, at least near room temperature, the intercalated lithium is highly mobile in the host. The internal energy of the system depends on how the lithium is distributed among the sites in the interlayer gaps, because of lithium-lithium interactions and elastic energy effects (J.R.Dahn, D.C.Dahn, and Haering 1982). The equilibrium configuration of the lithium atoms is, in general, a function of temperature. We might therefore expect a term in the specific heat which is related to the changes in lithium configuration as a function of temperature. The following section (6.2) will show, however, that at the temperatures used in this study, motion of lithium between sites will have essentially stopped. The specific heat at these temperatures is therefore due only to the thermally excited vibrational motion of a crystal in which each lithium is 'frozen' on one particular site.

6.2 MOBILITY OF INTERCALATED LITHIUM

It is clear that lithium is free to move about in the interlayer gaps of intercalated layered compounds at room temperature, since intercalation is not possible otherwise. Neutron diffraction studies of Li_xTiS_2 (J.R.Dahn et al. 1980) show that intercalated lithium spends most of its time localized in the octahedral sites in the interlayer gaps.

Because the local environment of the lithium is very similar, this is also expected to be true in Li_xNbS_2. The accepted point of view of lithium motion between sites involves occasional thermally activated 'hops' over a potential energy barrier. As is well known, the time τ_h between hops in such a situation is given by

$$\tau_h = Ae^{E/k_BT} \qquad (6\text{-}1)$$

where E is the energy barrier and A is a constant. Direct evidence for this picture comes from the NMR measurements on Li_xTiS_2 made by Kleinberg (1982) and Silbernagel (1975). From the temperature dependence of the ^7Li linewidth, Kleinberg was able to evaluate the constants A and E and found $A=1.9\cdot10^{-11}$s and E=.291eV (E/k_B=3370K). Similar values of A and E should occur in Li_xNbS_2.

Using for convenience the approximate values E=.3eV and $A=10^{-11}$ allows a calculation of τ_h as a function of temperature, the results of which are shown in table III. Since the temperature corresponding to a given value of τ_h depends only logarithmically on A, it need not be accurately known. The temperatures do depend strongly on E, however, and since E was measured on Li_xTiS_2, the values in the table must be considered to be only approximate. It is clear that at the temperatures of the specific heat measurements, lithium hopping will be frozen out, and the configurational degrees of freedom will not contribute to the specific heat.

So far it has been shown that at low temperatures the intercalated lithium will be fixed in one particular

Table III

Hopping time as a function of temperature.

τ_h(s)	T(K)
10^{-6}	302
10^{-3}	188
1	137
10^{3}	101
10^{6}	89
10^{9}	76

configuration; nothing has been said about the nature of that configuration. This is an important point, since phase transitions may occur on cooling. As an example, the phase diagram of Li_xNbS_2 is expected to qualitatively resemble one calculated using the 'spring and plate' model (J.R.Dahn, D.C.Dahn, and Haering 1982; see also Safran 1980, and Millman and Kirczenow 1983). This is a lattice gas model which includes in the Hamiltonian the elastic energy associated with the expansion of the host lattice on intercalation. The phase diagram for staging is shown in figure 41. Clearly, if the system remains in thermodynamic equilibrium, there is a possibility that some samples will change stage on cooling. Another possibility is that phase

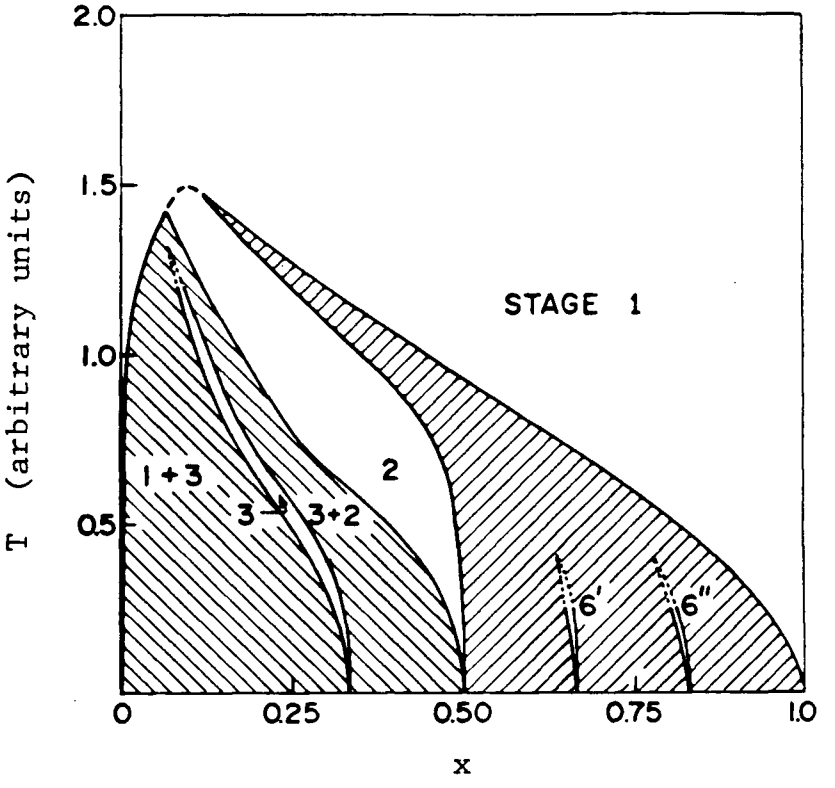

Figure 41: Staging phase diagram for a typical intercalation compound according to the model of Dahn, Dahn, and Haering (1982). The integers represent regions of pure stages; the shaded areas are phase mixtures. The model allows for phases of higher stage, although these are not included in the diagram.

transitions involving in-plane lithium ordering may occur.

The question of what configuration is frozen in as the temperature is lowered can be addressed using a simple theory first used by Bragg and Williams (1934) in their classic paper on atomic ordering in quenched alloys. Consider an intercalation compound at temperature T, in which the lithium atoms happen to be in a configuration which is the equilibrium state at another temperature θ. We assume that the system relaxes to equilibrium at T with a time constant τ, which we assume is of order τ_h. That is, we write

$$d\theta/dt=-(\theta-T)/\tau\simeq-(\theta-T)/\tau_h \qquad (6-2)$$

If we now assume the intercalation compound is being cooled at a constant rate dT/dt=-r,

$$d\theta/dT\simeq(\theta-T)/\tau_h r \qquad (6-3)$$

An analytic expression for the solution of this equation can be easily obtained, but it is rather unwieldy. As pointed out by Bragg and Williams there is a simple approximate solution which is good enough for our purposes. As long as $\tau_h r<<1$, θ-T will be small, and the solution is essentially θ=T. As T is lowered, τ_h begins to increase rapidly. At first, we still have $d\theta/dT\simeq1$, and the solution is

$$\theta\simeq T+r\tau_h \qquad (6-4)$$

At still lower temperatures, $r\tau_h$ becomes large enough that the approximation of (6-4) breaks down, and after this θ

remains essentially constant as T is decreased further. This point where θ 'decouples' from T occurs roughly at the point where $d\theta/dT=0$ in (6-4), that is, when

$$-r\frac{dT_n}{dT} = \frac{rAE}{k_B T^2} e^{E/k_B T} = 1 \qquad (6\text{-}5)$$

Temperatures calculated from (6-5) for various cooling rates are shown in table IV.

The precooling from room temperature to liquid nitrogen temperature before a specific heat experiment takes 3 to 4 hours, so that the cooling rate is about 0.1 K/s. The Li_xNbS_2 samples should therefore end up in a state characteristic of equilibrium at about 120K (assuming E=.3eV). Note that the cooling rate does not have a large effect on this temperature.

This calculation shows that the low temperature staging and ordering phase transitions predicted by equilibrium lattice gas models of intercalation compounds (J.R.Dahn, D.C.Dahn, and Haering 1982, and references therein) will not actually occur at temperatures below about 100K, no matter how slow a cooling rate is used. Since the exact phase diagram and E value for Li_xNbS_2 are not known, these calculations do not provide an unambiguous answer to the question of whether or not some Li_xNbS_2 samples changed stage on cooling. If the samples remained in thermal equilibrium down to T=0, the spring and plate model indicates that <u>all</u> the samples would be phase mixtures of the staged structures at x=1/3,1/2, etc.(figure 41). The

Table IV

Decoupling temperature for various cooling rates.

Cooling Rate (K/s)	Decoupling Temperature (K)
100	154
1	129
0.1	120
0.001	104

arguments of this section do make it clear that this extreme type of phase separation will not occur.

6.3 PHONON SPECIFIC HEAT

In this section the theory of low temperature lattice specific heat will be briefly reviewed. This theory is based on the well known quantum theory of the harmonic lattice (see, for example, Ashcroft and Mermin 1976, chapter 23). The lattice specific heat depends on the dispersion relations $\omega_s(\bar{k})$ of phonon modes. (Here s is a branch index and $\bar{k}$ is the phonon wave vector.) Most rigorously, the specific heat c is given by a sum over the discrete set of phonon modes. In a macroscopic crystal, however, the allowed phonon wavevectors are very close together, and the sum may be replaced by an integral in the usual way. This leads to

the following expression for the specific heat per mole;

$$c = V \frac{\partial}{\partial T} \sum_s \int_{B.Z.} \frac{d\vec{k}}{(2\pi)^3} \frac{\hbar\omega_s(k)}{e^{\hbar\omega_s(\bar{k})/k_BT} - 1} \qquad (6\text{-}6)$$

where V is the molar volume, and the integral is taken over the Brillouin zone.

This general relation can be simplified for low temperatures, since the Bose-Einstein occupation factor

$$(e^{\hbar\omega_s(k)/k_BT} - 1)^{-1}$$

becomes vanishingly small for $\hbar\omega(\bar{k})>>k_BT$. At low enough temperatures in a three dimensional material only the three acoustic phonon branches, for which $\omega(\bar{k})\rightarrow 0$ as $\bar{k}\rightarrow 0$, make a significant contribution to c. The following simplifications in (6-6) may then be made:

1. Optical phonon modes may be ignored.
2. At very low temperatures, only the very long wavelength portion of the acoustic phonon dispersion curves will be important. In this region, the phonon dispersion relation is linear, and we can use

$$\omega_s(\bar{k})=v_s(\hat{k})k \qquad (6\text{-}7)$$

   where k is the magnitude of $\bar{k}$, $\hat{k}$ is a unit vector in the direction of $\bar{k}$, and $v_s(\hat{k})$ is the velocity of sound in that direction.
3. Since the integrand is vanishingly small except near k=0, we may take the integral in (6-6) to be over all of

k-space.

These simplifications lead to

$$c = V \frac{\partial}{\partial T} \sum_s \int \frac{d\vec{k}}{(2\pi)^3} \frac{\hbar v_s(\hat{k})k}{(e^{\hbar v_s(\hat{k})k/k_BT} - 1)} \qquad (6\text{-}8)$$

The integral will be rewritten in spherical coordinates. Taking $d\vec{k}=k^2dkd\Omega$ (Ω is the solid angle);

$$c = V \frac{\partial}{\partial T} \sum_s \int d\Omega \int_0^\infty \frac{dk}{(2\pi)^3} \frac{\hbar v_s(\hat{k})k^3}{(e^{\hbar v_s(\hat{k})k/k_BT} - 1)} \qquad (6\text{-}9)$$

Making the change of variables $y=\hbar v_s(\hat{k})k/k_BT$ in the k integration gives

$$c = V \frac{\partial}{\partial T} \sum_s \int \frac{d\Omega}{(2\pi)^3} \frac{(k_BT)^4}{(\hbar v_s(\hat{k}))^3} \int_0^\infty \frac{y^3\,dy}{e^y - 1} \qquad (6\text{-}10)$$

Since the definite integral over y is just $\pi/15$, carrying out the derivative with respect to T yields

$$c = \frac{\pi k_B V T^3}{30\hbar^3} \sum_s \int \frac{d\Omega}{(v_s(\hat{k}))} \qquad (6\text{-}11)$$

If $1/v^3$ is defined to be the average over mode index s and solid angle of the inverse cubed sound velocity, that is

$$\frac{1}{v^3} = \frac{1}{3} \sum_s \int \frac{d\Omega}{4\pi} \frac{1}{v_s(\hat{k})^3} \qquad (6\text{-}12)$$

then c is given by

$$c = \frac{2\pi^2}{5} k_B V \left(\frac{k_B T}{\hbar v}\right)^3 \qquad (6\text{-}13)$$

The phonon specific heat coefficient β is given by

$$\beta = \frac{c}{T^3} = \frac{2\pi^2}{5} k_B^4 V \left(\frac{1}{\hbar v}\right)^3 \qquad (6\text{-}14)$$

These relations hold at temperatures low enough that the only phonons which have a significant probability of being thermally excited are the long wavelength acoustic phonons which satisfy the linear dipersion relation (6-7).

The well-known Debye formula was devised to describe the specific heat over the entire temperature range from T=0 up. It is often used to fit data at intermediate temperatures where (6-13) fails. However, it fits the data for layered compounds very poorly, primarily because, as we shall see, their phonon dispersion relations are highly anisotropic. In spite of this, specific heat data even on layered compounds are often presented in terms of an effective Debye temperature, and in order to define this it will be useful to briefly review Debye theory. The Debye formula is derived by setting $\omega_s(\bar{k})=vk$ in (6-6) and taking the integration not over the Brillouin zone, but over a sphere in k-space which contains the same number of allowed

phonon wave vectors[23]. This condition on the size of the sphere specifies its radius, the Debye wavenumber k_D. The Debye frequency ω_D and temperature θ_D are given by

$$k_B\theta_D=\hbar\omega_D=\hbar v k_D \tag{6-15}$$

The result for the molar specific heat is

$$c = 9N_A k_B \left(\frac{T}{\theta_D}\right)^3 \int_0^{\theta_D/T} \frac{y^4 e^y \, dy}{(e^y - 1)^2} \tag{6-16}$$

where N_A is Avogadro's number. In the limit $T\to 0$, this becomes

$$c = \frac{12\pi^4}{5} N_A k_B \left(\frac{T}{\theta_D}\right)^3 \tag{6-17}$$

and the coefficient β is

$$\beta = \frac{12\pi^4 N_A k_B}{5\theta_D^3} \tag{6-18}$$

Since the definition (6-15) of θ_D in terms of the Debye sphere does not make sense for layered compounds, effective Debye temperatures for these materials are defined in terms of the low temperature limits (6-17) and (6-18).

---

[23] Note that both the sound velocity and the distance from the origin to the zone boundary are assumed to be isotropic.

6.4 THE PHONON SPECIFIC HEAT OF Li_xNbS_2 IN THE ELASTIC CONTINUUM (T^3) LIMIT

As we have just seen, the cubic specific heat coefficient β can be related to an 'average' sound velocity v and a Debye temperature θ_D by means of equations (6-14) and (6-18), respectively. Using the measured β values (figure 35), v and θ_D have been calculated for the Li_xNbS_2 samples and are shown in figures 42 and 43, respectively. Clearly, there are large changes in the lattice dynamics as a function of x.

In this section, an elastic continuum model will be used to discuss the specific heat in terms of the elastic constants of Li_xNbS_2. To show how β depends on the elastic constants, a value for NbS_2 will be calculated. Materials of hexagonal symmetry have 5 independent elastic stiffness constants, which are, in the standard abbreviated subscript notation, c_{11}, c_{33}, c_{44}, $c_{66}=(c_{11}-c_{12})/2$, and c_{13} (Auld 1973). To the author's knowledge, the elastic constants of NbS_2 have not been measured. McMullen and Irwin (1984) have recently fit Raman spectra for NbS_2 with a simple 4-parameter valence force model. In principle, elastic constants can be calculated from these inter-atomic forces, but because of the simplicity of the model and the limited amount of data used in the fit it is not clear that the values would be reliable.

More extensive data are available for several related compounds, however, and these are listed in table V. The values for all three compounds in the table are similar, and

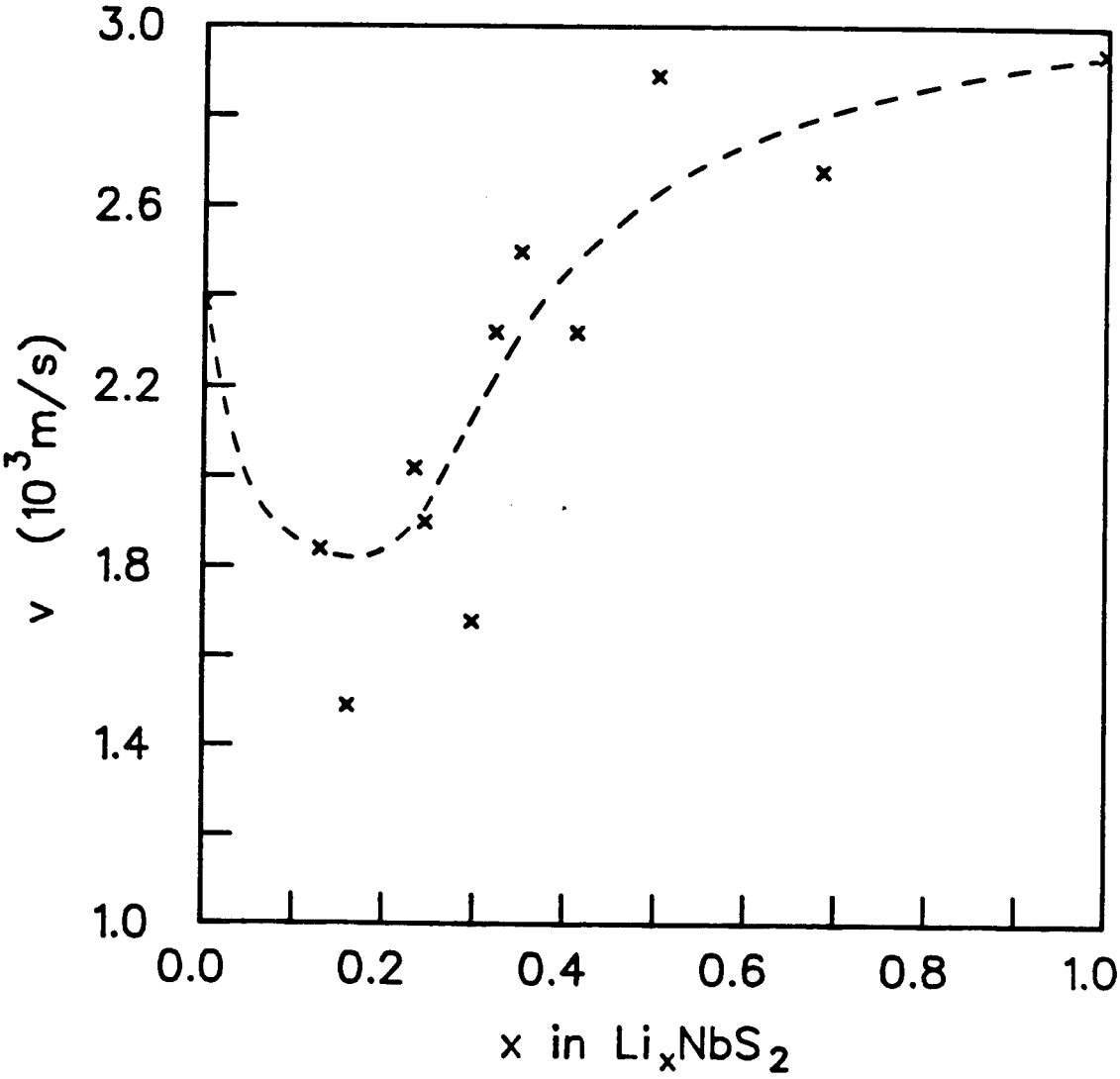

Figure 42: 'Average' sound velocity v (equation 6-14) for the Li_xNbS_2 samples. The dashed line is intended only as a guide for the eye.

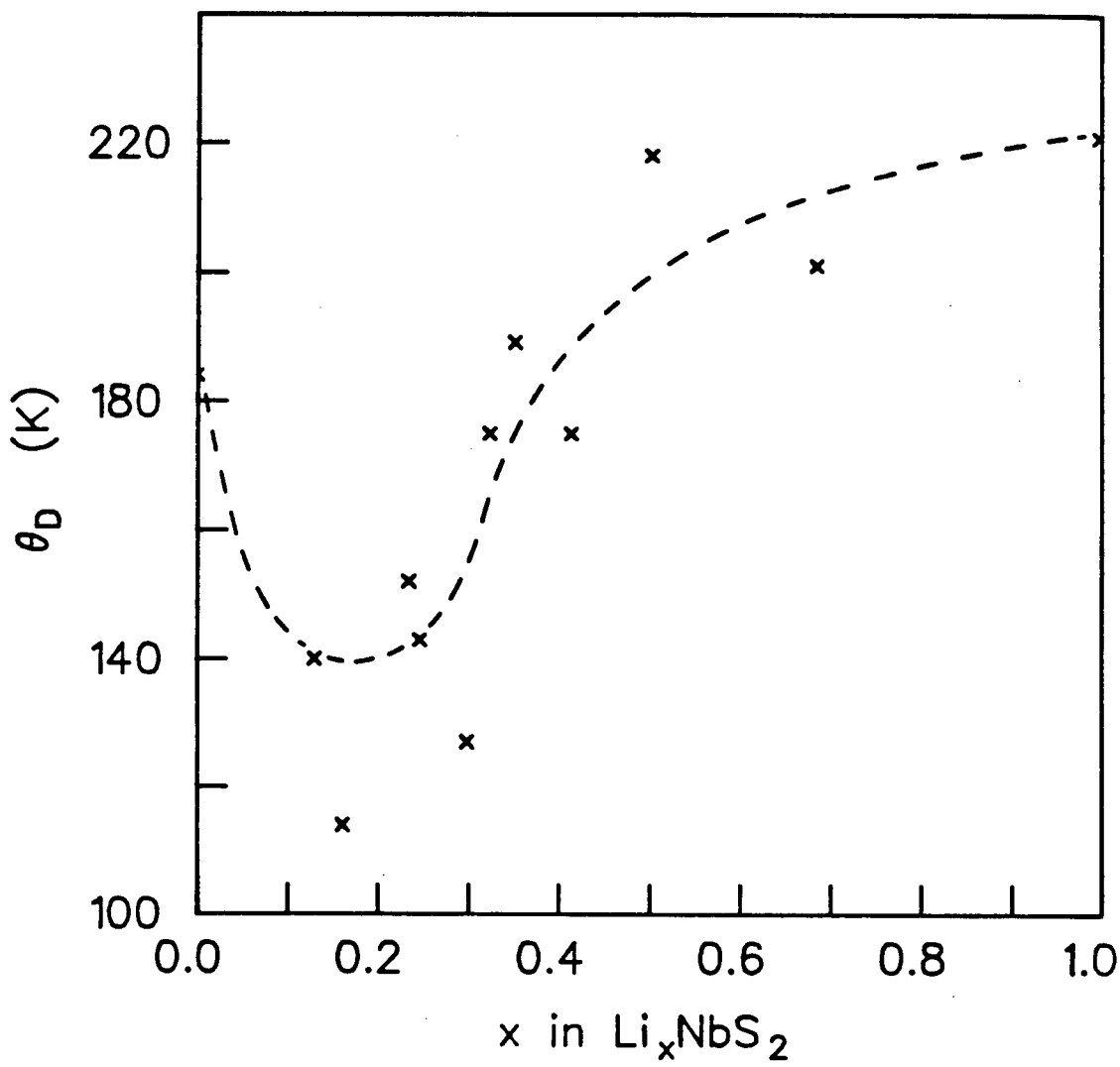

Figure 43: Debye temperatures for the Li_xNbS_2 samples. The dashed line is a guide for the eye.

Table V

Elastic constants for some layered transition metal dichalcogenides with the 2H structure. The values in the table are in units of $10^{10}N/m^2$.

Elastic Constant	Compound $TaSe_2$*	$NbSe_2$†	MoS_2**
c_{11}	19.6 to 12.4	10.8	17.4
c_{33}	5.3	4.6	5.2
c_{44}	1.74	1.9	1.9
c_{66}	5.5 to 5.4	4.6	7.3
c_{13}	1.34 to .76	≃1.	2.3

* Feldman (1982)
† Feldman (1976, 1982); Jericho et al. (1980)
** Feldman (1976, 1982)

the same may be expected of NbS_2. For the purposes of this illustration the elastic constants of $NbSe_2$ will be used. Most of the $NbSe_2$ constants in the table were deduced from inelastic neutron scattering data by Feldman (1976). Jericho et al. have measured c_{11} ultrasonically. In Feldman's 1976 work c_{13} could not be specified very accurately; it was given as between +3.1 and -0.2 in units of $10^{10}N/m^2$. A more sophisticated analysis involving an atomic force model (Feldman 1982) gives c_{13} between 1.34 and 0.76 in the same units, for $TaSe_2$. This result should be approximately

applicable for $NbSe_2$ as well, and so for the following calculations $c_{13}=1.0\cdot10^{10}N/m^2$ will be used.

To calculate β from the elastic constants we first find the sound velocity as a function of the direction of propagation, then calculate the average of the inverse cube of the velocity (equation 6-12). The sound velocities in a hexagonal crystal are functions only of the angle θ between the c-axis and the direction of propagation. The velocities of the three acoustic modes are (Auld 1973)

$$v_1(\theta) = \{ c_{11}\sin^2\theta + c_{33}\cos^2\theta + c_{44} - ((c_{11}-c_{44})\sin^2\theta+(c_{44}-c_{33})\cos^2\theta)^2+(c_{13}+c_{44})^2\sin^2\theta\}^{\frac{1}{2}}/(2\rho)^{\frac{1}{2}}$$

$$v_2(\theta) = \{(c_{66}\sin^2\theta + c_{44}\cos^2\theta)/\rho\}^{\frac{1}{2}} \qquad (6\text{-}19)$$

$$v_3(\theta) = \{ c_{11}\sin^2\theta + c_{33}\cos^2\theta + c_{44} + ((c_{11}-c_{44})\sin^2\theta+(c_{44}-c_{33})\cos^2\theta)^2+(c_{13}+c_{44})^2\sin^2\theta\}^{\frac{1}{2}}/(2\rho)^{\frac{1}{2}}$$

In these equations, ρ is the density ($4.6g/cm^3$ for NbS_2). Polar plots of the inverse sound velocities as a function of θ are given in figure 44. Mode 1 is a quasi-shear wave. At $\theta=0$ it becomes a pure shear (transverse) wave propagating along the c-axis, with atomic displacements in the basal plane. This is an example of what is called a 'rigid layer' shear mode. Since intralayer bonding forces are much

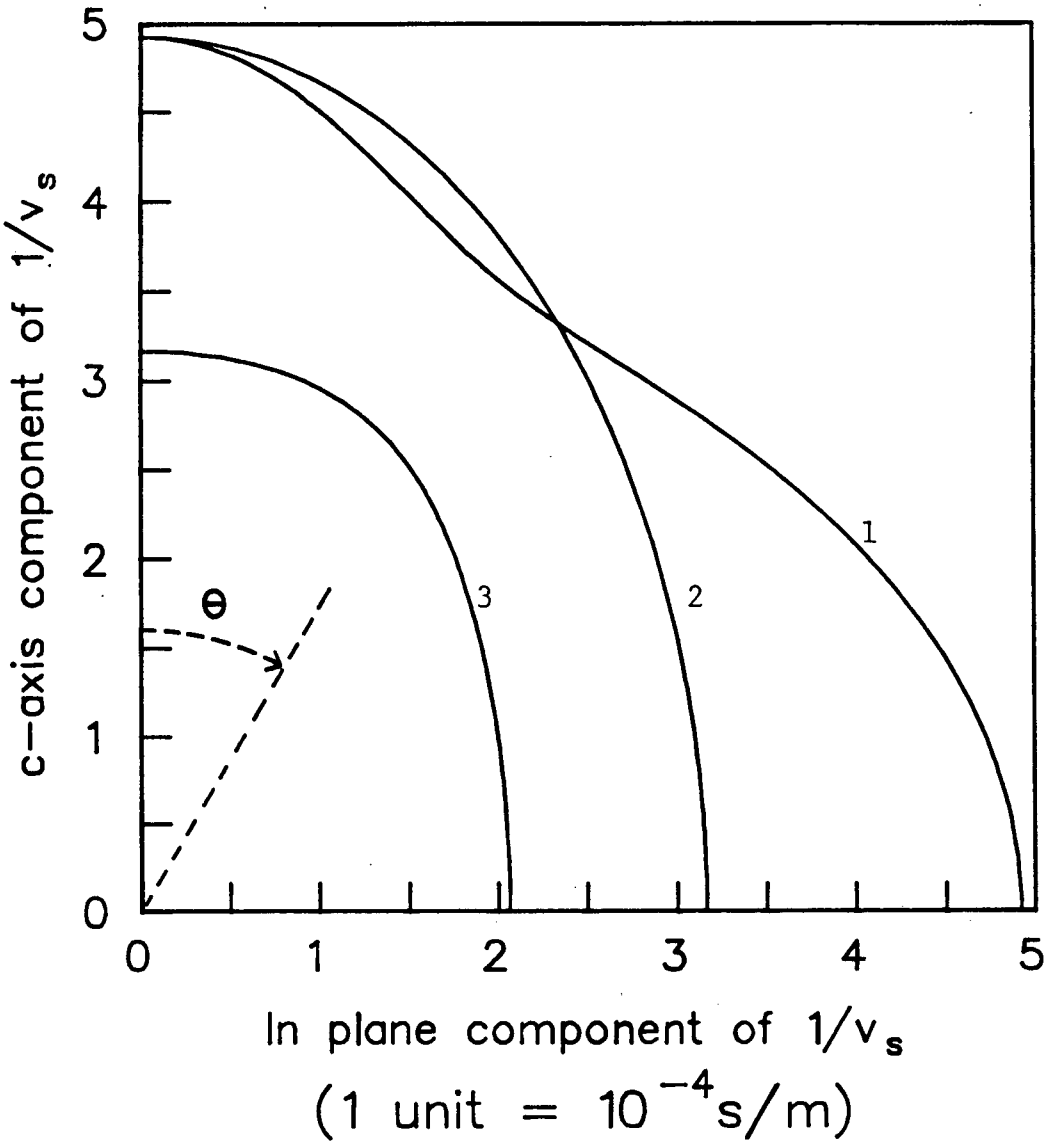

Figure 44: Polar plot of the inverse sound velocities calculated for NbS_2 (see text). The curves are labelled with the mode index s. Modes 1 and 2 intersect the vertical axis at $(\rho/c_{44})^{\frac{1}{2}}$. Mode 3 intersects the vertical axis at $(\rho/c_{33})^{\frac{1}{2}}$. Modes 1, 2, and 3 intersect the horizontal axis at $(\rho/c_{44})^{\frac{1}{2}}$, $(\rho/c_{66})^{\frac{1}{2}}$, and $(\rho/c_{11})^{\frac{1}{2}}$, respectively.

stronger than the interlayer ones, this acoustic wave involves essentially rigid layers vibrating as units. At $\theta=\pi/2$, mode 1 again is a pure shear wave, now propagating in the basal plane with the atomic displacements along the c-axis. That this is also essentially a rigid layer shear mode (at least for long wavelength) is clear from figure 45. The fact that mode 1 is a rigid layer shear wave at both $\theta=0$ and $\pi/2$, results in its sound velocity being $\sqrt{c_{44}/\rho}$ in both those directions. c_{44} is the elastic constant associated with 'rigid layer' shear. Since mode 1 is the mode with the lowest sound velocity it makes the largest contribution to the specific heat.

Mode 2 is a pure shear wave for all θ, polarized in the direction normal to both the c-axis and the direction of propagation. It is a rigid layer shear wave at $\theta=0$, but at $\theta=\pi/2$ it involves shearing of the layers themselves (elastic constant c_{66}). Mode 3 is a quasi-longitudinal wave, which becomes pure longitudinal at $\theta=0$ and $\pi/2$.

Because the sound velocity is a function only of θ, equation (6-12) for the average inverse cube velocity becomes

$$\frac{1}{v^3} = \frac{1}{3}\sum_{s=1}^{3}\int_0^{\pi/2}\frac{\sin\theta\, d\theta}{v_s^3(\theta)} \qquad (6\text{-}20)$$

The integral for the pure shear wave (mode 2) can be

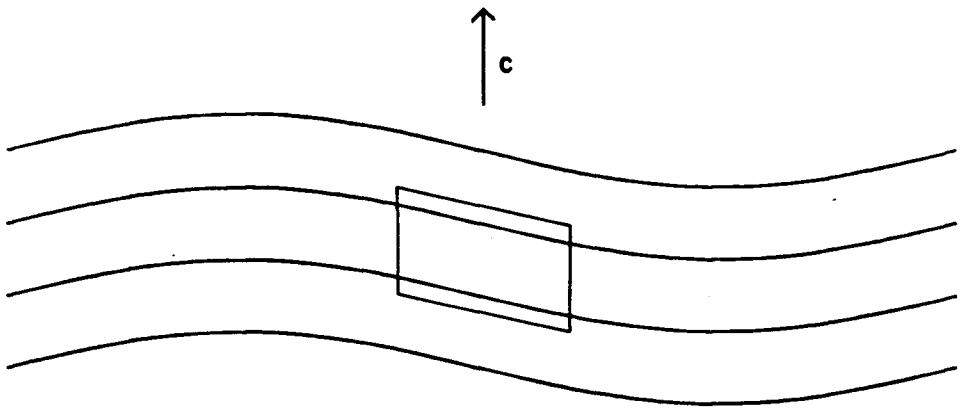

Figure 45: Acoustic mode 1 at $\theta=\pi/2$. The curved lines represent the NbS_2 layers. The parallelogram would be a rectangle in the undistorted material, and indicates the nature of the strains associated with the wave.

evaluated easily and is

$$\int_0^{\pi/2} \frac{\sin\theta \, d\theta}{v_2^3(\theta)} = \frac{\rho^{3/2}}{c_{66}\, c_{44}^{1/2}} = 4.9 \cdot 10^{-11} \ s^3/m^3 \quad (6\text{-}21)$$

The numerical value was calculated using $NbSe_2$ elastic constants and the density of NbS_2. The integrals for the other two modes were calculated numerically, and are $9.21 \cdot 10^{-11} s^3/m^3$ for mode 1 and $1.50 \cdot 10^{-11} s^3/m^3$ for mode 3. The average of these is $1/v^3 = 5.21 \cdot 10^{-11} s^3/m^3$, which, when used in (6-14) gives $\beta = .22 mJ/mole\text{-}K^4$. The experimental value for NbS_2 is $.31 \pm .04 mJ/mole\text{-}K^4$, which is 30% higher. This is reasonable agreement, considering the calculations were made using the elastic constants of $NbSe_2$, a closely related, but different, material. The difference in β indicates that NbS_2 has somewhat softer elastic constants than $NbSe_2$[24]. The corresponding calculated and experimental Debye temperatures are 206K and 187±7K, respectively.

Now the effect of intercalation on the specific heat can be considered in this elastic continuum limit. Of the five elastic constants, there are two, c_{33} and c_{44}, which depend primarily on interlayer forces. c_{33} is associated with compression along the c-axis, and c_{44} is associated

---

[24] McMullen and Irwin's (1984) fit to the Raman spectra does not seem to agree with this conclusion. For example, the fit implies $c_{44} \simeq 2.5 \cdot 10^{10} N/m^2$, which is stiffer than $NbSe_2$. However, this discrepancy may not be significant, since the elastic constants depend on the model used to fit the Raman data.

with rigid layer shear. These two elastic constants are expected to change significantly as x in Li_xNbS_2 is varied.

Of these two interlayer elastic constants, c_{44} plays a much larger role in determining the low temperature specific heat. In the calculation above the contribution to β from mode 1, which depends mainly on c_{44}, is much larger than the contributions from the other modes. Another illustration of the importance of c_{44} comes from a numerical calculation of the derivatives of β with respect to the c's. These are, in units of $10^{-15}m^2J/N\text{-mole-}K^4$,

$$\partial\beta/\partial c_{11}=-.42$$

$$\partial\beta/\partial c_{33}=-1.52$$

$$\partial\beta/\partial c_{44}=-7.91$$

$$\partial\beta/\partial c_{66}=-1.47$$

$$\partial\beta/\partial c_{13}=+1.05$$

$\partial\beta/\partial c_{44}$ is much larger than the others.

To roughly estimate the size of the changes in c_{44} which are required to explain the data, β was calculated for several values of c_{44}. The results are shown in figure 46. A similar plot was also made for c_{33}. As can be seen from the plot, the range of β values covered by the Li_xNbS_2 data (.18 to 1.32 $mJ/mole\text{-}K^4$) corresponds to changes of c_{44} of about a factor of 10, provided the other elastic constants are fixed at their $NbSe_2$ values. Much larger fractional changes in c_{33} (about a factor of 20) would be required.

In addition, the simple 'spring and plate' elastic model to be presented later in this chapter (section 6.6.2)

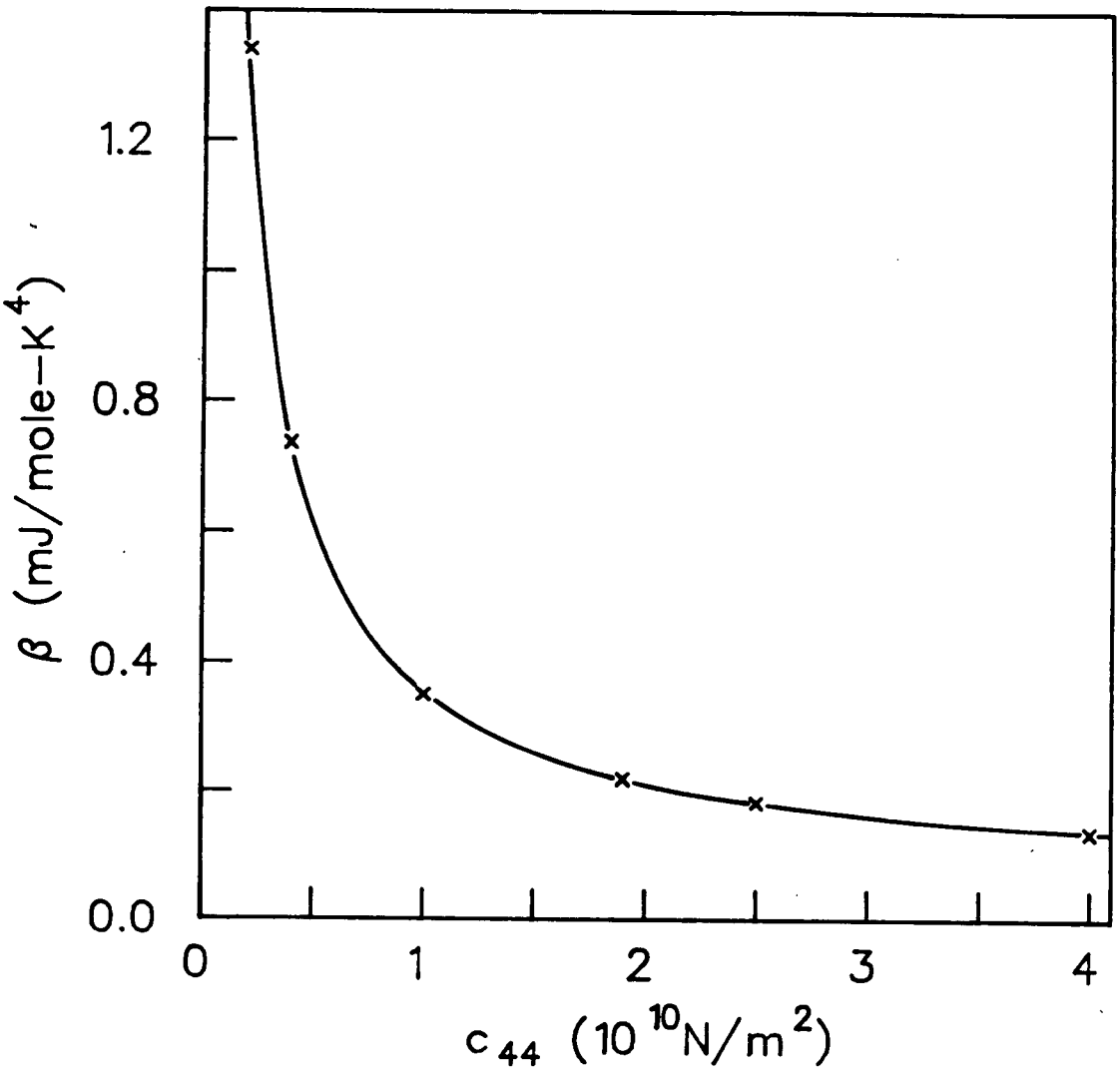

Figure 46: β as a function of c_{44}. The other elastic constants are fixed at their $NbSe_2$ values (see text).

shows that c_{33} should increase monotonically as a function of x in Li_xNbS_2. Basically, the argument is that since the interlayer gaps expand on intercalation, the lithium must be pushing the layers apart. Intercalated lithium atoms can be thought of as compressed springs which act against the original NbS_2 interlayer forces to separate the layers. Since we are adding more interlayer springs as x increases, c_{33} must also increase. The Li_xNbS_2 samples with x between .12 and .5, however, have β values higher than at x=0. This indicates an intercalation induced reduction in whichever elastic constant is primarily responsible for the variations in β. The elastic constant primarily responsible for the changes in β is therefore almost certainly c_{44}.

Another point concerning c_{33} can be made here, although it is not essential to the argument that the data reflect the behavior of c_{44}. Elastic stability conditions may be derived from the requirement that the elastic energy must be a positive definite function of the strains. If it is not, there will be some strain for which the elastic energy is negative, and the crystal will spontaneously distort. This argument leads to the conditions (Born and Huang 1954, Feldman 1976)

$$c_{33}>c_{13}^2/c_{11} \qquad (6\text{-}22)$$

$$c_{33}>2c_{13}^2/(c_{11}+c_{12}) \qquad (6\text{-}23)$$

There are no restrictions on c_{44}, except, of course, that it must be positive. The stability conditions can be evaluated using the $NbSe_2$ elastic constants. In units of $10^{10}N/m^2$,

using c_{13}=1.0 as in the specific heat calculations yields c_{33}>.09 and c_{33}>.16, respectively. If the maximum c_{13} (3.1) consistent with Feldman's (1976) estimates is used we get c_{33}>.89 and c_{33}>1.5, respectively. To explain the data in terms of c_{33} alone would require it to take on a value of about .3 in the x=.16 sample, which might result in a violation of the stability criteria, depending on the actual value of c_{13}. The lattice distortions that would result from this have not been observed in either Li_xNbS_2 (chapter 2), or in Li_xNbSe_2 (D.C.Dahn and Haering 1982).

6.5 BEYOND THE ELASTIC CONTINUUM LIMIT

This section will show how, as the temperature rises, the phonon specific heat begins to deviate from its low temperature T^3 behavior. The reasons for this will be explained, and approximate calculations of the temperature at which significant deviations set in will be made. An understanding of the deviations from T^3 is important, since it

1. allows us to be confident that the experiments have truly found the low temperature limit, and
2. provides some additional insight into the mechanism for changes in the specific heat on intercalation, supporting the conclusion that c_{44} is primarily responsible.

Deviations from T^3 behavior at higher T come about because the phonon dispersion curves are linear only in the

very long wavelength limit, and because they are truncated at the Brillouin zone boundaries. (At higher T we can no longer make the approximation that the integral in (6-6) extends over all of k-space.) Phonon dispersion curves for 2H-$NbSe_2$ have been measured at room temperature by inelastic neutron scattering (Moncton et al. 1977) and are shown in figure 47. The dispersion curves for NbS_2 and its intercalation compounds should be similar. The labelling of the different phonon branches is that of Moncton et al. The long wavelength parts of branches Σ_3 and Δ_6 correspond to acoustic mode 1 of the previous section (the rigid layer shear mode), with propagation along the a and c axes, respectively. Note that at point A on the zone boundary there is no splitting between the Δ_6 acoustic and Δ_5 optical shear branches, or between the Δ_1 and Δ_2 longitudinal branches. This is because of the symmetry of the two layer high unit cell. We could think of the Δ_6 and Δ_5 branches as an acoustic branch in the double zone, which has simply been folded over. In a stage 2 intercalation compound the symmetry is broken and a small gap should appear at the zone boundary.

Looking further at the dispersion curves of figure 47, we notice two features that may cause the first deviations from T^3 as the temperature is raised. One of these is the relatively low energy of the top of the Δ_6,Δ_5 branch. The other is the anomalous upward curvature of the Σ_3 branch.

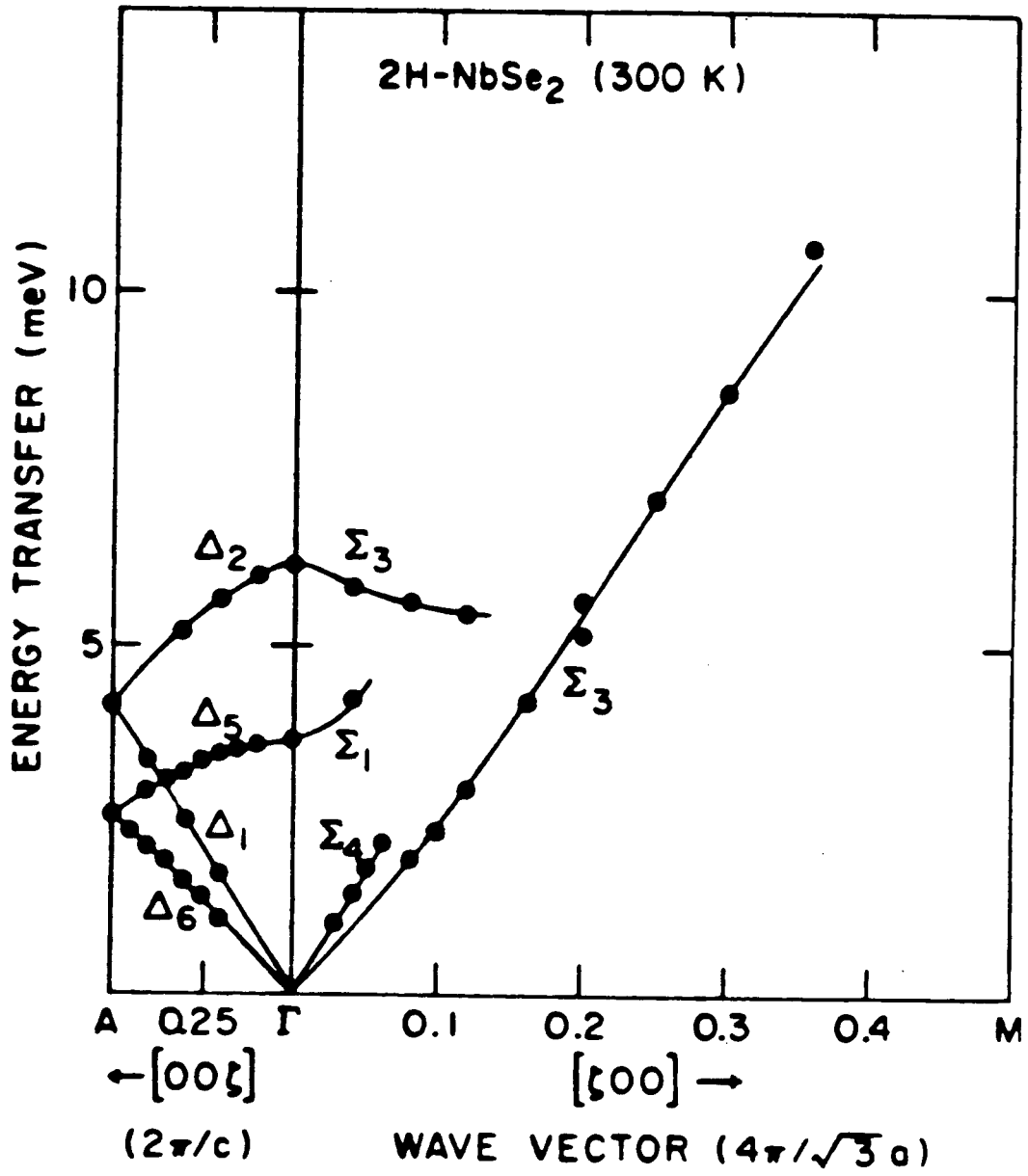

Figure 47: Phonon dispersion curves from inelastic neutron scattering measurements on $NbSe_2$. After Moncton et al. (1977).

This upward curvature can be explained in terms of forces associated with bending of the layers, as was first demonstrated in theoretical studies of the specific heat of graphite (Komatsu 1955, Bowman and Krumhansl 1958). Acoustic waves propagating in the basal plane with atomic displacements along the c-axis, although they are basically shear waves, also involve bending of the layers (see figure 45 in the previous section). Since the layers are stiff and c_{44} is small, the energy due to bending the layers can be significant, especially at short wavelengths. The layer bending energy density is proportional to the square of the layer curvature, that is, it is proportional to $(\partial^2 u/\partial y^2)^2$, where u is the atomic displacement associated with the wave, and y is a coordinate along the direction of propagation. The shear elastic energy is $c_{44}(\partial u/\partial y)^2$. It can be shown (Komatsu 1955) that when the potential energy is a sum of layer bending and shear terms, the dispersion relation for waves is

$$\rho\omega^2 = c_{44}k^2 + bk^4 \qquad (6\text{-}24)$$

where b is a positive constant. The second term is due to the layer bending forces. This explains the upward curvature of the Σ_3 phonon branch. The value b can be estimated graphically from figure 47, and is approximately $4 \cdot 10^{-14} m^4/s^2$.

To estimate the temperatures at which the bk^4 term and the truncation of the Δ_6, Δ_5 mode will cause deviations from T^3 in the specific heat, we first recall (6-6), the general

expression for the phonon specific heat. This involved integrals of the form

$$\int d\vec{k} \frac{\hbar\omega_s(\vec{k})}{e^{\hbar\omega_s(\vec{k})/k_BT} - 1} \qquad (6\text{-}25)$$

If we assume for the moment an isotropic elastic material (as in the Debye model), this becomes

$$\int \frac{2\pi k^2 \hbar v k}{e^{\hbar v k/k_BT} - 1} dk \qquad (6\text{-}26)$$

If we define $z=\hbar vk/k_BT$, then the integrand is proportional to $z^3/(e^z-1)$. This function is the same as the black body radiation spectrum (Kittel 1969, p256, for example) and has its maximum value at $z\simeq3$. It drops to zero at large z, and has half its peak value at $z\simeq5.5$. What this means is that the specific heat is quite sensitive to phonons with energies up to about 5 times k_BT. The general conclusion that the specific heat is sensitive to phonon energies up to several times k_BT is expected to be true even for anisotropic materials.

It is now possible to produce rough estimates of the temperatures at which the two different effects being considered will cause deviations from T^3 in the specific heat. The top of the Δ_6,Δ_5 branch occurs at a phonon energy $\hbar\omega$ of order $\hbar\sqrt{c_{44}/\rho(2\pi/c)}$, where c is the height of the two layer unit cell. As we have just seen, deviations from T^3 will occur when this phonon energy becomes less than about $5k_BT$. If T_t is defined as the temperature above which this

c-axis truncation causes deviations from T^3, we have

$$T_t \simeq \frac{\hbar}{5k_B}\frac{2\pi}{c}\sqrt{\frac{c_{44}}{\rho}} \qquad (6\text{-}27)$$

Similarly, we can define T_b as the temperature above which the bk^4 term in the dispersion relation for the layer bending (Σ_3) branch causes deviations from T^3. This can be estimated by setting $5k_bT_b$ equal to the energy at which the two terms $c_{44}k^2$ and bk^4 in the dispersion relation (6-24) are equal. This gives

$$T_b \simeq \frac{\hbar}{5k_B}\frac{c_{44}}{\sqrt{\rho b}} \qquad (6\text{-}28)$$

For $c_{44}=1.9\cdot10^{10}N/m^2$, the value used for the calculation of β for NbS_2, we get $T_t=16K$ and $T_b=30K$. The estimates of of T_t and T_b are very approximate, but we can see that both mechanisms are probably important. This is unlike the case of graphite, where T_b appears to be significantly lower than T_t (Komatsu 1955). To compare these estimates with the data, the quantity $T_{10\%}$ will be used. This is defined as the temperature at which the lattice specific heat data deviate by 10% from βT^3. The results are given in table VI.

The value for NbS_2 (16±1K) is reasonably close to the estimated temperatures T_t and T_b. This suggests that the explanation of the deviations from T^3 given above is correct.

The $T_{10\%}$ data also show that there is a strong correlation between high β values (which we believe to be

Table VI

β and $T_{10\%}$ for the Li_xNbS_2 samples.

x	β(mJ/mole-K^4)	$T_{10\%}$(K)
0	.31	16±1
.13	.7	9.5±1
.16	1.32	9.5±.5
.23	.55	13±.5
.25	.66	9±2
.30	.96	9±.5
.32	.36	16±2
.35	.29	Insufficient data
.41	.36	≥9
.50	.19	≥15
.68	.24	13±1.5
1.00	.18	15±2

due to low c_{44}'s), and low $T_{10\%}$. This is what is expected on the basis of the equations (6-27 and 6-28) for T_t and T_b. Taking another numerical example, the value of β for the x=.16 sample implies a c_{44} value of about $0.2 \cdot 10^{10} N/m^2$. This yields T_t=5K and T_b=3K. $T_{10\%}$ was 9.5±.5K. Again, this is reasonable agreement, considering the roughness of the theoretical estimates.

An interesting feature to note is that because of the different ways that T_t and T_b depend on c_{44}, the plate bending mechanism will become relatively more important as c_{44} is lowered. This suggests that the specific heat *vs* temperature curves of different Li_xNbS_2 samples will have different shapes. This is unlike simple Debye theory, where the specific heats of different materials all fall on one universal curve if they are plotted as a function of T/θ_D. The present Li_xNbS_2 data for higher temperatures (above 10K) are not, unfortunately, of sufficient quantity or quality to allow a satisfactory test of this result.

A more complete discussion of the specific heat above the T^3 regime would best be based on a detailed atomic force constant model such as those used by Wakabayashi and Nicklow (1979), or Feldman (1982). Such models attempt to fit the entire phonon spectrum, and allow calculation of the specific heat at arbitrary temperatures directly from the general expression (6-6). At present, because of the limited high temperature specific heat data, and the lack of other measurements of the phonon spectra, the effort involved in such an approach would not appear to be justified.

6.6 SIMPLE MICROSCOPIC MODELS

So far in this chapter, the approach to lattice dynamics has been primarily through an elastic continuum approximation. To complement this view, and to gain some further insight into the specific heat of Li_xNbS_2, it is useful to consider

some simple microscopic dynamical models.

6.6.1 VIBRATIONAL MOTION OF A SINGLE INTERCALATED LITHIUM ION

When one lithium ion is inserted into a site between the layers of a NbS_2 crystal, we expect the appearance of three new vibrational modes, because of the three new degrees of freedom associated with motion of the lithium ion about the center of its three dimensional site. These new modes are localized vibrational modes involving the lithium as well as neighboring sulfur and niobium atoms (see Pryce 1969, for example). However, because the mass of lithium is so small compared to the other atoms in the compound, the amplitude of vibration of the lithium will be very much larger than that of the surrounding heavy atoms. The approximate frequency of the localized modes can therefore be calculated assuming the surrounding NbS_2 layers are fixed. To model the forces on the lithium, we assume it is connected to the fixed rigid layers by springs. A reasonable value for the spring constant G_c associated with lithium motion in the c-axis direction is 160 N/m. This will come out of the 'spring and plate' model calculations in the next section. The vibrational frequency of the mode where the lithium motion is along the c-axis is then

$$\omega_c = \sqrt{G_c/m} \qquad (6\text{-}29)$$

where m is the mass of a lithium atom. Numerical values are $\omega_c = 1.\cdot 10^{14} s^{-1}$ and $\hbar\omega_c/k_B = 900K$, so that this vibrational mode will clearly not contribute to the low temperature specific heat.

The spring constant G_a associated with motion parallel to the layers can be estimated from the fact that there is a potential energy barrier of order .3eV high between adjacent lithium sites (Kleinberg 1982). Assuming the lithium atom sits in a harmonic potential well of depth .3eV and width equal to half the distance between sites yields $G_a \simeq 4N/m^2$. This yields an in-plane vibrational frequency

$$\omega_a = \sqrt{G_a/m} = 2\cdot 10^{13} s^{-1} \qquad (6\text{-}30)$$

which is equivalent to a temperature of 140K. This is also much too high to be seen in the low temperature specific heat.

In the discussion above, it was assumed that the lithium atom was in a 'typical' site, and that the only forces on it were those associated with localizing it on its site (that is, those due to interaction with the host layers). The situation may be somewhat more complicated.

Staged intercalation compounds are generally believed to posess a domain or island structure as proposed by Daumas and Herold (1969). Within each domain there is a well defined staging sequence, but globally there are guest atoms in every interlayer gap. As an

example, a stage 2 Li_xNbS_2 crystal would have lithium in gaps 1,3,5, etc. in some domains and in gaps 2,4,6, etc. in the others. Kaluarachchi and Frindt (1983) have found that the domain size is of order 130Å in Ag_xTiS_2. At the boundaries between the staging domains, the host layers must bend, and this raises the possibility that some of the lithium sites are significantly distorted. Lithium atoms in these sites would have different vibrational frequencies than the others, and we cannot rule out the possibility that they would contribute to the low temperature specific heat.

Another complication arises from the fact that intercalated lithium atoms interact with each other. There is some evidence that this interaction is relatively weak. Lattice gas model fits to electrochemical data on Li_xTiS_2 (J.R.Dahn, D.C.Dahn, and Haering 1982) used a repulsive nearest-neighbor lithium-lithium interaction of 50meV, which is small compared to the .3eV barrier between sites. Because of this, it may be that the effect of lithium-lithium interaction on the vibrational frequencies is small. On the other hand, the lithium-lithium interaction is the driving force for the lithium ordering transitions which occur in Li_xTaS_2 (J.R.Dahn and McKinnon 1984), and probably in 'fresh' Li_xNbS_2 (section 2.3), and it cannot be completely ignored. A wide range of unusual elastic behavior is possible in systems where there is a

competition between a periodic background potential (in this case due to the NbS_2 layers) and an interparticle interaction. (For discussions of one dimensional systems of this type see, for example, Von Hohneyen et al. 1981, Sharma and Bergerson 1984, and references therein.) One possibility in the case of Li_xNbS_2 is that for lithium concentrations near but not equal to values such as x=1/3 where ordering occurs, the lithium configuration in each gap may consist of ordered two dimensional regions separated by discommensurations (domain walls). There could be soft modes associated with these domain walls. Further theoretical and experimental work is needed to determine if any such soft modes actually exist in Li_xNbS_2.

6.6.2 ONE DIMENSIONAL MODELS

The basic model to be used in this section is a one dimensional infinite chain of masses M separated by springs of spring constant K. The model will be used to describe rigid layer longitudinal modes, so each mass can be thought of as representing an entire NbS_2 layer. K represents the interlayer forces (figure 48). Since both M and K are both proportional to the area of the layer and because the vibrational frequencies depend only on their ratio K/M, the layer area is arbitrary. For convenience, we will take the area to be the base of a unit cell, so that M is just the mass of one NbS_2

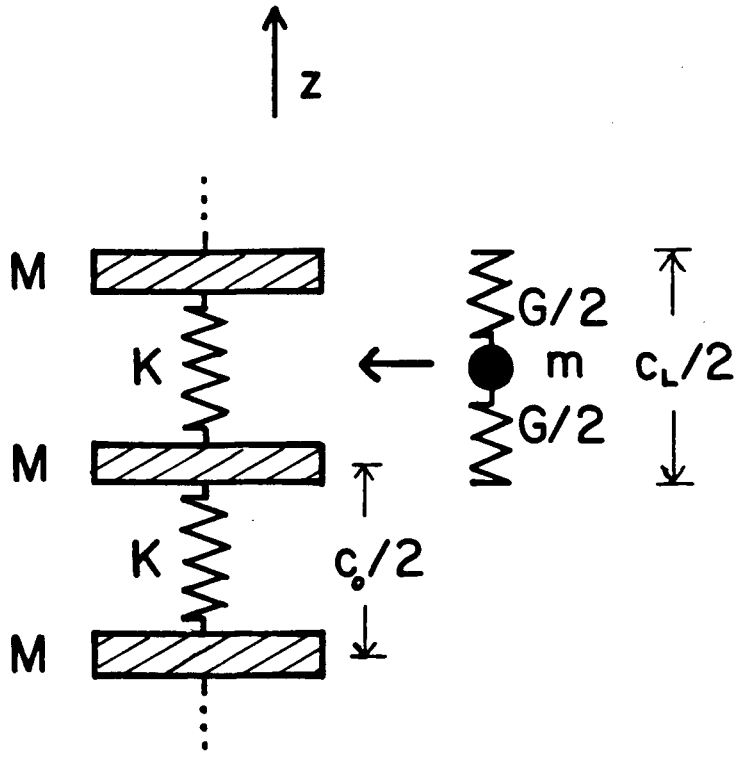

Figure 48: Definition of terms used in the one-dimensional 'spring and plate' model (see text).

unit. We also take the system to lie along the z axis. The distance between masses is c/2, because the unit cell is two layers high. The dispersion relation for waves in this system is well known, and is

$$\omega = 2\sqrt{\frac{M}{K}} \left|\sin \frac{kc}{4}\right| \qquad (6\text{-}31)$$

where k and ω are the wavenumber and frequency, respectively. The spring constant K is related to c_{33} by

$$K=\sqrt{3}c_{33}a^2/c \qquad (6\text{-}32)$$

where c and a are the lattice parameters. The $NbSe_2$ value $c_{33}=4.6\cdot10^{10}N/m^2$ gives K=7.4 N/m. The same equations apply for vibrations normal to the z-axis (rigid layer shear waves), except that K is then $\sqrt{3}c_{44}a^2/c$.

To deal with the longitudinal rigid layer waves of intercalated material, it is possible to use the 'spring and plate' model of intercalation (J.R.Dahn 1982; J.R.Dahn, D.C.Dahn, and Haering 1982) In this model the host material is again considered to be a system of rigid plates joined by springs of strength K. The equilibrium length of these 'host springs' is taken to be the host layer spacing $c_0/2$. Intercalation is modelled by the insertion of 'lithium springs' of strength G and length $c_L/2>c_0/2$. In Li_xNbS_2, there are x lithium springs for each host spring. Balancing the forces of the springs yields an equation for the c-axis

of the intercalation compound as a function of x.

$$\frac{c(x) - c_0}{c_L - c_0} = \frac{x}{x+K/G} \qquad (6\text{-}33)$$

With appropriate values of c_L and K/G, this equation gives a c-axis expansion in approximate agreement with experimental results for many intercalation compounds. A rough fit to the Li_xNbS_2 lattice expansion data requires $K/G \cong .2$. The most striking success of the spring and plate model has been its use in statistical mechanical lattice gas models of intercalation compounds. These models can be used to calculate the voltage V(x) of intercalation cells, but fit the data for systems such as Li_xTiS_2, Li_xNbSe_2, and Li_xNbS_2 very poorly unless the elastic energy associated with the lattice expansion (6-33) is included in the Hamiltonian. The elastic energy also provides a mechanism which produces staging.

To use the spring and plate model to discuss vibrational modes, consider first the case of Li_1NbS_2. According to the model, each pair of adjacent layers is now separated by two springs in parallel, with spring constants K and G. This is equivalent to one spring with spring constant $K_{eff}=K+G$. The lithium ion of mass m is placed in the center of this effective spring, dividing it into two springs each of strength[25]

---

[25] The spring constant G_c of the previous section is $4K_{eff}$, or about 160 N/m.

$2K_{eff}$. The dispersion relation for this system has two branches, corresponding to the + and - signs in

$$\omega^2 = \frac{2K_{eff}}{mM}\left(m + M \pm \sqrt{m^2+M^2+2mM\cos(kc(1)/2)} \right) \qquad (6\text{-}34)$$

where c(1) is the c-axis of Li_1NbS_2. The - branch is an acoustic branch. Using the fact that m/M=.045 is small, we can justify the use of the approximate relation

$$\omega \simeq 2\sqrt{\frac{K_{eff}}{M}}\left|\sin\frac{kc(1)}{4}\right| \qquad (6\text{-}35)$$

in which the mass of the lithium has been ignored.

For the optical (+) branch, the same approximation results in

$$\omega = 2\sqrt{K_{eff}/m} \qquad (6\text{-}36)$$

As might be expected, the frequency is the same as that of a single lithium vibrating between stationary layers. The new modes associated with the lithium degrees of freedom are contained in this optical branch. The optical branch is at too high a frequency to contribute to the low temperature specific heat, and it will therefore be ignored in the rest of this discussion.

Since only the acoustic mode is important, we can, as we have just seen, ignore the lithium mass and say that the only effects of intercalation are to alter the spring constant from K to K_{eff} and to expand the c-axis. (Of these, the first is far more important.) This approach will now be used to discuss Li_xNbS_2 with x<1.

For stage one compounds, the spring constant between each layer is $K_{eff}=K+xG$, and the dispersion relation is just

$$\omega = 2\sqrt{\frac{K_{eff}}{M}}\left|\sin\frac{kc(x)}{4}\right| \qquad (6\text{-}37)$$

where c(x) is the height of the two layer unit cell of Li_xNbS_2.

A stage two compound may be modelled by alternating springs of strength K (empty gaps) and $K_{eff}=K+2xG$ (full gaps), where x is the overall lithium concentration. The dispersion relations are

$$\omega^2 = \frac{K+K_{eff}}{M} \pm \frac{1}{M}\sqrt{K^2+K_{eff}^2+2KK_{eff}\cos kc(x)} \qquad (6\text{-}38)$$

Here again there is an optical and an acoustic branch.

In figure 49, dispersion relations representing NbS_2, stage 2 $Li_{.15}NbS_2$, and stage 1 $Li_{.3}NbS_2$ are shown. The dispersion relations for the stage 1 compounds have been 'folded over' into the smaller one dimensional Brillouin zone of the stage 2 compound. We see that the initial slope of the stage two curve lies between that of the x=0 and stage 1 curves, in spite of the lowering of part of the acoustic branch due to the gap at the zone boundary. This is a general result, and indicates that in the spring and plate model the contribution to the specific heat from the rigid layer longitudinal mode (elastic constant c_{33}) will be a monotonically decreasing function of x, even when staging is taken

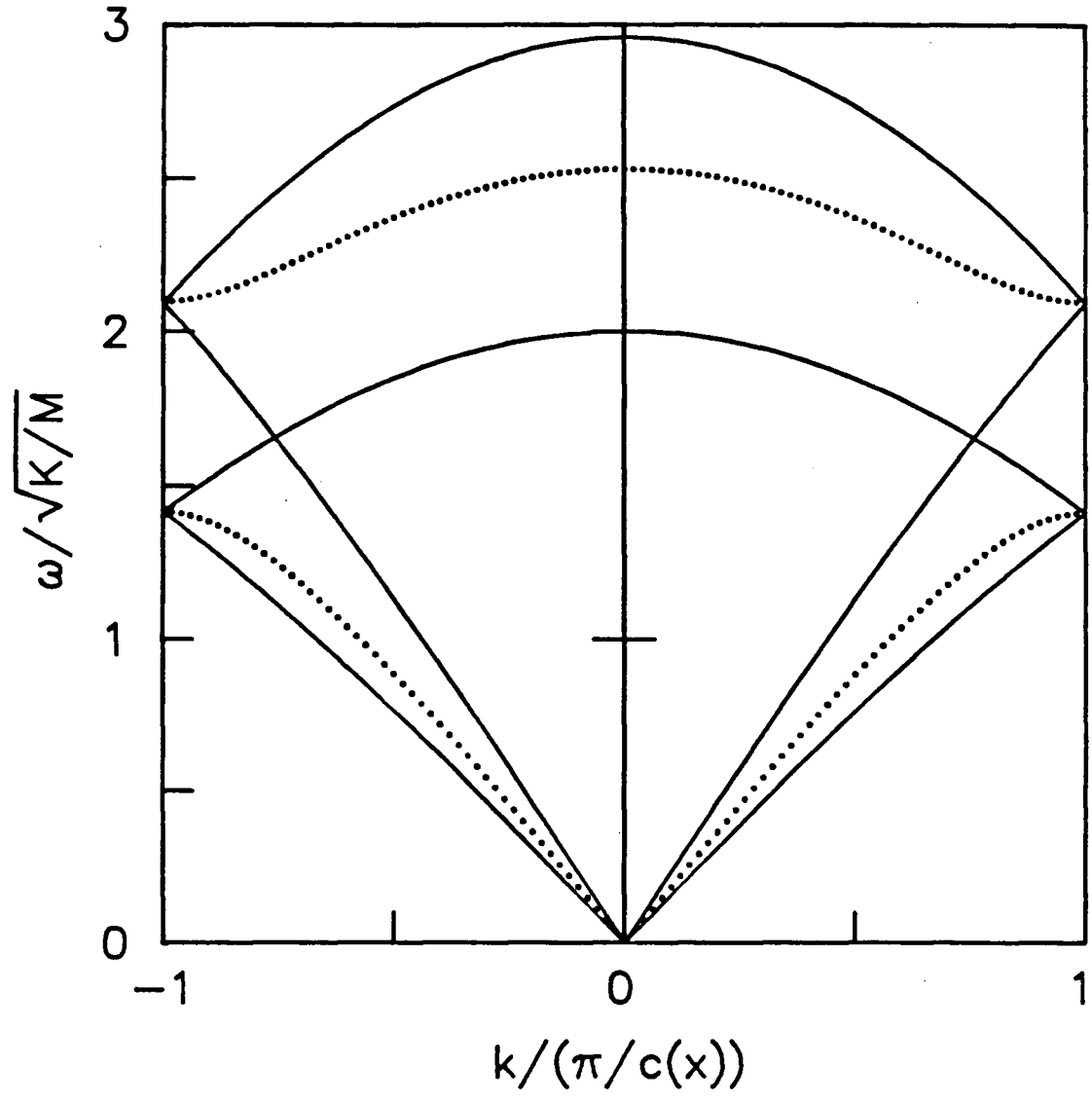

Figure 49: Model dispersion relations for the longitudinal mode propagating along the c-axis in Li_xNbS_2. Included are curves representing $^xNbS_2$ (lower solid lines), stage 2 $Li_{.15}NbS_2$ (dotted lines), and stage 1 $Li_{.3}NbS_2$ (upper solid lines).

into account.

6.7 DISCUSSION

The simple theoretical arguments put forward in this chapter indicate that the elastic constant c_{44} and the rigid layer shear modes associated with it are primarily responsible for the differences in the specific heat coefficients β of the different Li_xNbS_2 samples. The extra vibrational modes due to the addition of lithium are at frequencies too high to contribute to the specific heat. Looking at the data again in this light, it is possible to draw the following conclusions:

1. In the samples with $x \leq .3$, c_{44} was significantly smaller than in pure NbS_2. Most of the c-axis expansion which takes place on intercalation happens at low x (figure 7). By x=.3, the expansion is almost complete, and if we assume the expansion is all in the interlayer gaps, the gaps have expanded by about 15%. Intercalation and gap expansion appear to greatly reduce the interlayer shear forces that were present in the pure host.

   It is interesting to note that the sample with the highest β (lowest c_{44}) was stage 2 (x=.16). This is surprising, since only half of the interlayer gaps contain lithium and are expanded. If the shear forces between two layers depend only on the lithium concentration in the gap between them, we would expect

c_{44} for stage 2 to be between the values for x=0 and stage 1. That this is not so seems to imply that the shear forces across an interlayer gap are sensitive not only to the lithium in that gap, but also to the lithium in neighboring gaps. It is possible that charge transfer has something to do with this. Another possibility has been mentioned in section 6.6.1; there may be soft modes associated with Daumas-Herold staging domain boundaries.

2. As x approaches 1, the lattice stiffens up again. At x=1, β is actually smaller than x=0, indicating c_{44} is greater than in the pure host. A rough calculation shows that it may be possible to explain the stiffening at large x by assuming shear stresses are transmitted from one NbS_2 layer to the next through the intervening layer of lithium. From the activation energy for lithium hopping between sites it was estimated (section 6.6.1) that an effective spring constant for in-plane motion of a lithium atom near the center of its site is 4 N/m. If we consider this as being due to two 'springs', one connecting the lithium ion to each of the two adjacent layers, the spring constant of each is 2 N/m. These springs are joined end to end at the lithium atom, and are therefore equivalent to a single spring of strength 1 N/m connecting the layers. If we assume these springs are the only interlayer shear forces, the elastic constant c_{44} is given by

$$c_{44}=2cGx/\sqrt{3}a^2 \qquad (6\text{-}39)$$

where c and a are the dimensions of the unit cell and G is the spring constant (1 N/m) per lithium. For Li_1NbS_2 this yields $c_{44}=1.3\cdot10^{10}N/m^2$. Although this is smaller than the value of about $2.5\cdot10^{10}N/m^2$ implied by the specific heat data, it is at least of the right order of magnitude, and indicates that lithium contributes to the interlayer shear forces.

3. β, and therefore c_{44}, do not appear to be smoothly varying functions of x for the set of samples studied. In particular, the samples at x=.16 and .30 have higher β values than the samples near them in x. These two samples were both prepared from NbS_2 from batch DD12, shortly after that batch was grown. As mentioned in chapter 2, freshly prepared and aged DD12 material behaved differently electrochemically. Cells made from fresh material showed two small peaks in -dx/dV near 2.67V, which may be due to lithium ordering. Recall that 2.67V is also the voltage used for preparation of the x=.30 (fresh) and x=.32 (aged) specific heat samples. Since all of the specific heat samples except for x=.16 and .30 (which were anomalous) and x=.50 (which was prepared at a voltage far from the extra dx/dV peaks) were made from relatively old NbS_2, it seems likely that whatever aging effect caused changes in the electrochemistry also caused changes in the specific heat. If the aging effect is due to loss of sulfur and subsequent intercalation of excess niobium into the

interlayer gaps, this might serve to help bind the layers together and reduce the specific heat. The presence of lithium ordering might itself influence the specific heat. It should be noted that both the x=.3 and x=.16 samples had compositions near values where ordering might be expected, since the x=.16 sample was stage 2 and therefore had a lithium concentration near x=1/3 in the filled gaps. The effects of aging obviously need to be investigated further.

7. SUPERCONDUCTIVITY

7.1 INTRODUCTION

Specific heat anomalies due to superconductivity were observed in only three of the samples, NbS_2 (T_c=5.7K), $Li_{.23}NbS_2$ (3.1K), and $Li_{.25}NbS_2$ (3.1K). The data are reproduced here (table VII), together with the electronic specific heat coefficient γ. It is, of course, likely that at least some of the other samples were superconductors, but with T_c's below the temperatures at which the measurements were made. These minimum temperatures are also listed in the table. Some results related to superconductivity in the NbS_2 sample have already been presented in section 4.3.

Because of the reduction in $N(\epsilon_F)$, the density of electron states at the Fermi level, which is due to charge transfer into the dz^2 band, the general result that superconductivity is eventually destroyed at large x is to be expected. Some of the results, however, clearly cannot be explained on the basis of rigid band charge transfer alone. The stage 2 samples at x=.12 and .16 did not exhibit superconductivity, even though the .16 sample was measured down to 2.0K. This is surprising, since the γ values for the stage two samples are roughly equal to those of the superconducting samples, indicating that they have about the same $N(\epsilon_F)$. A similar situation occurs for the stage one samples at x=.30, .32 and .35, These all had γ values comparable to the superconducting samples, but did not have

Table VII

Superconducting transition temperatures and electronic specific heat coefficients for the Li_xNbS_2 samples. Where no transition was observed, T_c is listed as being lower than the lowest temperature at which measurements were made.

x	T_c(K)	γ(mJ/mole-K^4)
0	5.7	19.3
.13	<2.7	10.9
.16	<2.0	13.1
.23	3.1	11.6
.25	3.1	10.3
.30	<1.8	9.4
.32	<2.8	11.4
.35	<2.8	10.6
.41	<2.6	6.0
.50	<2.8	5.8
.68	<2.8	4.8
1.00	None observed	1.3

superconducting transitions. This puzzling state of affairs will be discussed further at the end of this chapter.

In the next section, a Meissner effect measurement on one of the Li_xNbS_2 samples is described. This verifies that the specific heat anomalies observed were truly due to

superconductivity. In section 7.3, the present results will be compared with previous data (McEwan 1983, McEwan and Sienko 1982).

7.2 MEISSNER EFFECT MEASUREMENT

A magnetic measurement was made on a piece of the $Li_{.25}NbS_2$ sample[26]. The cryostat used (R.H.Dee and J.F.Carolan, unpublished) contains two identical, oppositely wound, superconducting coils in series. The sample was placed in the center of one of these pickup coils, and a piece of pure indium for calibration purposes in the other. The coils are connected to an RF-SQUID, which, together with its associated electronics, produces an output signal proportional to the total magnetic flux through the pickup circuit. The arrangement is insensitive to uniform magnetic fields, because the coils are oppositely wound. Whenever either the sample or the indium standard becomes superconducting, it expells magnetic flux (Meissner effect), and produces a signal. Transitions in the sample and indium can be distinguished because the flux change signals are of opposite sign. Thermometry for the experiment was provided by an Allen-Bradley carbon resistor which had previously been calibrated in the specific heat system by comparison with the germanium thermometers. The magnetic field in the vicinity of the sample could be varied by means of a

---

[26]The experiment was performed by J.Beis and the author

solenoid surrounding the pickup coil assembly. The fields used were of order a few gauss or less.

Data taken during a temperature sweep are shown in figure 50. The transitions due to both the sample and indium can be seen. There is also a slowly varying background, presumably due to paramagnetism in some of the components of the pickup coil - sample holder assembly. The indium transition is measured at 3.403K. The accepted value is 3.404K (Weast 1970), which provides a check on the thermometer calibration.

The transition of the $Li_{.25}NbS_2$ sample occurred over the range 3.31 to 2.93K, with 50% of maximum flux expulsion at 3.20K. The calorimetrically measured transition was centered at about 3.1K. The slightly higher magnetic transition is not surprizing, if the width of the transitions is due to inhomogenieties in the sample. This is because a reasonably complete Meissner effect can be seen, even if a significant part of the sample is still normal. All that is necessary to block magnetic flux is that superconducting regions somewhere in the sample extend all the way across a cross-section perpendicular to the field. The calorimetrically measured transition, on the other hand, is sensitive to the bulk of the sample.

Similar temperature scans were made in several different low magnetic fields, going both up and down in temperature. The transition temperature and width were both independent of the sweep direction and the field. (The

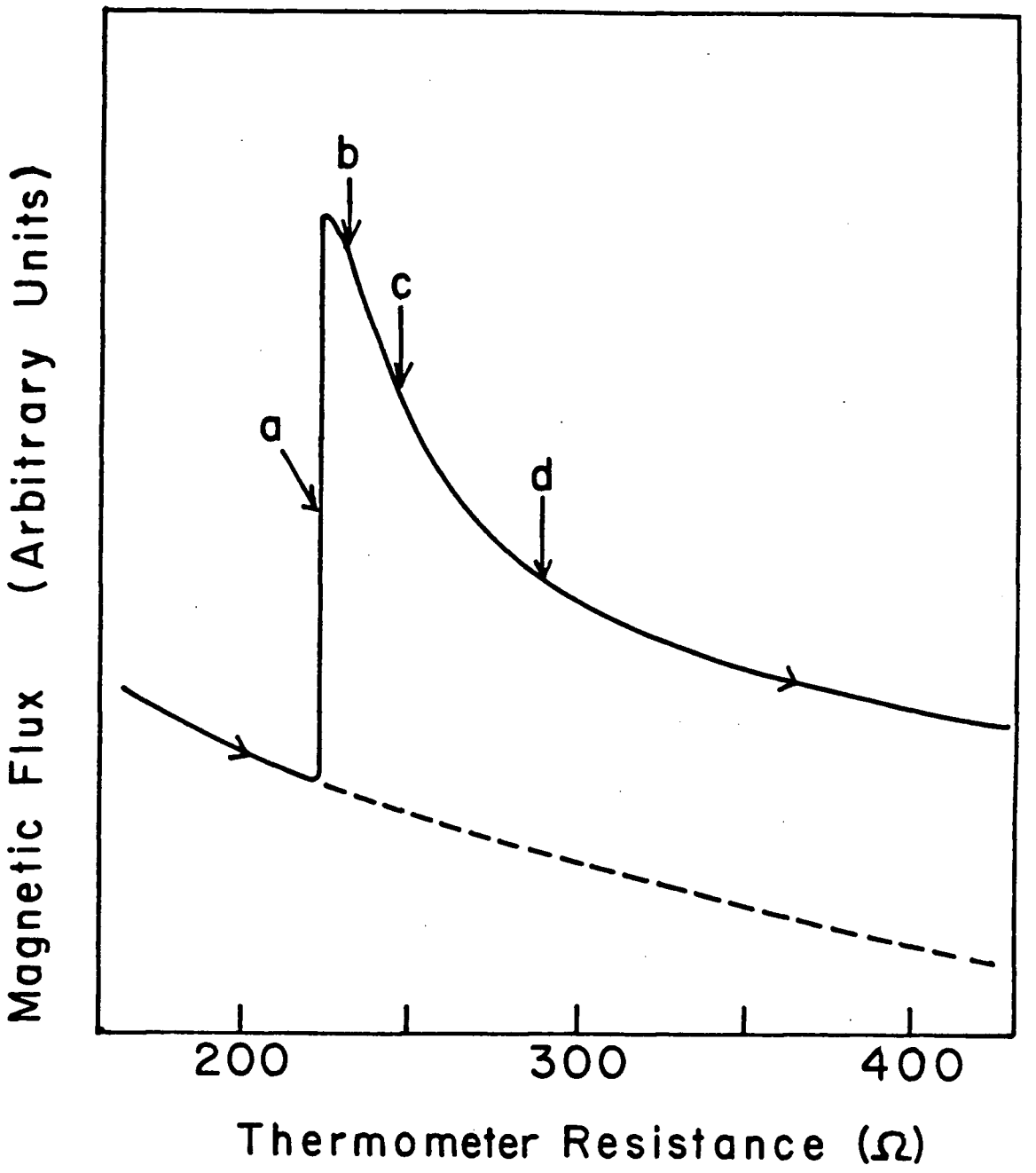

Figure 50: Meissner effect data on a $Li_{.25}NbS_2$ sample. The horizontal axis is the resistance of the carbon resistor used as a sample thermometer. The temperatures of important features have been calculated:

a- Indium transition at 3.403 K.
b- 3.31 K: transition in sample 10% complete.
c- 3.20 K: transition in sample 50% complete.
d- 2.94 K: transition in sample 90% complete.

The dashed line is the estimated background.

solenoid was not calibrated, but the fields used were between zero and a few gauss. The small applied magnetic field was used only to provide some flux to be expelled at the transition. To avoid depressing the transition temperature, the fields used must be much less than the critical field. Fields of a few gauss are expected to satisfy this condition, and the fact that the transition was independent of field, for fields of this magnitude, shows that this is indeed the case.)

7.3 COMPARISON WITH PREVIOUS WORK

The superconducting transition temperature of Li_xNbS_2 has been measured by McEwan and Sienko (McEwan 1983, McEwan and Sienko 1982). The results are shown in figure 51. The samples were prepared by high temperature reaction, and for $x \leq .13$ are phase mixtures of the 2H and 3R crystal types. Samples which were phase mixtures sometimes showed two separate transitions, and this is why the figure has two T_c's for some values of x. Li_xNbS_2 prepared by room temperature intercalation is 2H at all x, and so it is not possible to directly compare the results for $x \leq .13$.

For $x \geq .13$, however, McEwan and Sienko's samples were pure 2H, and in principle should have had the same properties as room temperature prepared material. For x between .13 and .17, McEwan and Sienko's samples exhibited (007) Bragg peaks in x-ray diffaction. Although they did not realize this, this line indicates that these samples were

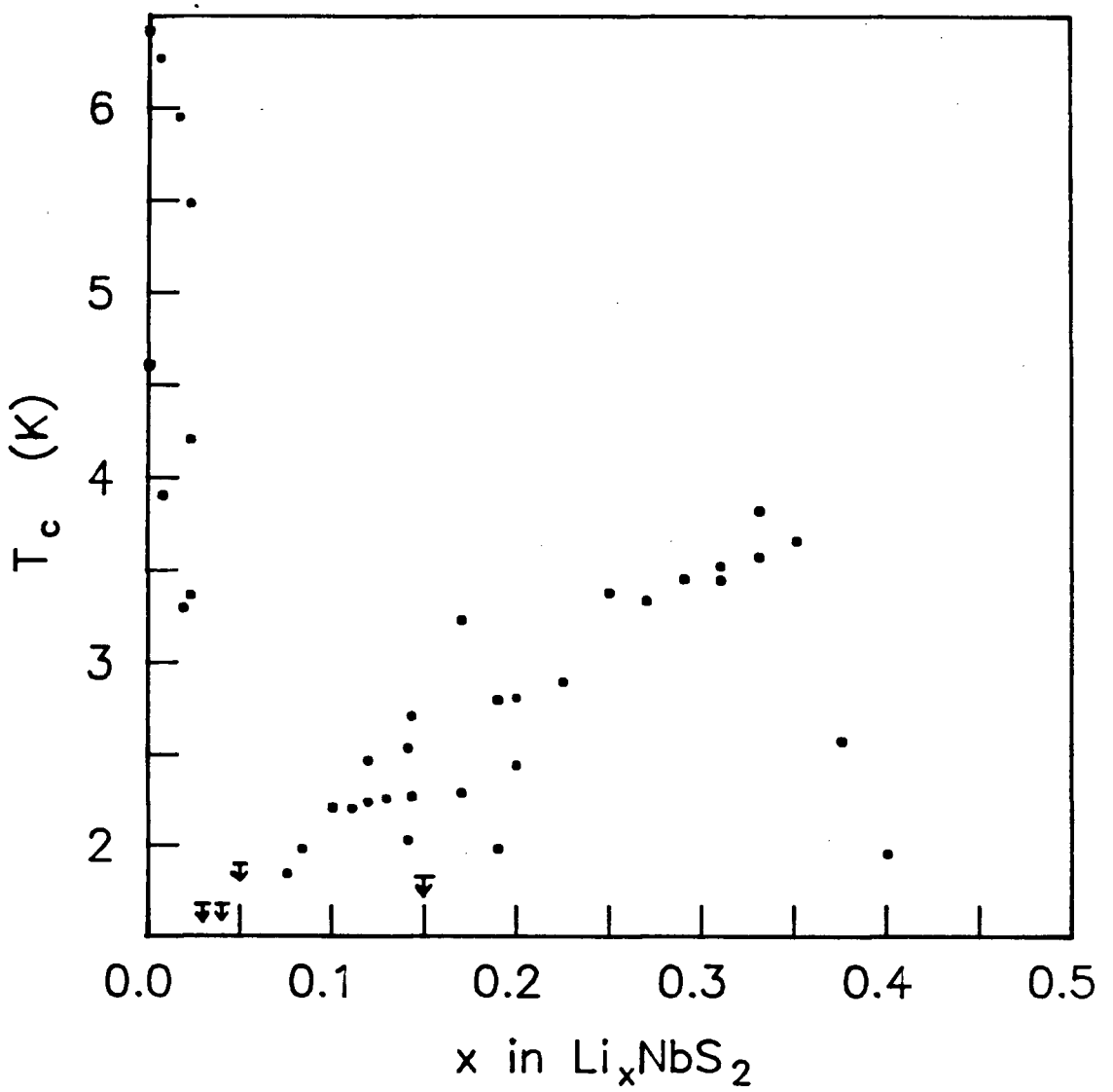

Figure 51: T_c as a function of x for a series of Li_xNbS_2 samples prepared at high temperatures (McEwan 1983). For samples where no T_c was observed, the symbol ↧ indicates the lowest temperature measured.

stage 2, or stage 2-stage 1 phase mixtures (section 2.3). Their result that T_c in the stage 2 region is lower than in the stage 1 region near x=.25 agrees with the results of the present study.

As McEwan and Sienko increased x above .17, they first passed through a region where the presence of two T_c's probably indicates a stage 2-stage 1 phase mixture. Near x=.25, close to the low x limit of the stage 1 phase, they observed one transition at about 3.2K, also in agreement with the present work. Between x=.30 and .35, however, McEwan and Sienko's T_c values remain in the 3.2 to 3.5K range, while in this work, the x=.30, .32 and .35 samples showed no superconductivity. This disagreement is not significant, since as mentioned in chapter 2 in relation to lattice parameter data, McEwan and Sienko's x values appear to be too high (by about .05 or more) in this region.

7.4 DISCUSSION

In the BCS theory of superconductivity, (Bardeen, Cooper, and Schrieffer 1957), T_c is given by

$$T_c = \frac{\hbar\langle\omega\rangle}{k_B} \exp\left[\frac{-1}{N(\epsilon_F)V}\right] \qquad (7\text{-}1)$$

where $\langle\omega\rangle$ is an average phonon frequency, V is the strength of the phonon mediated effective interaction, and $N(\epsilon_F)$ is the density of states at the Fermi level. Based on this equation, McEwan argued (qualitatively), that if $\langle\omega\rangle$ and V remain constant on intercalation, the rigid band charge

transfer model implies that T_c should be a monotonically decreasing function of x. This argument is correct as far as it goes. Although the BCS equation for T_c does not give accurate numerical values, it does correctly identify the general trends. (For a recent review of the theory of T_c, see Allen and Mitrovic 1982.) As $N(\epsilon_F)$ decreases due to charge transfer and band filling, T_c should drop.

Unlike more accurate equations for T_c, the BCS equation displays the dependence of T_c on $N(\epsilon_F)$ explicitly. It is therefore possible to use it, together with rigid band charge transfer, to calculate numerical values for T_c in Li_xNbS_2. Values for V and $\langle\omega\rangle$ can be estimated from data on NbS_2. Using $N(\epsilon_F)$ from the calculation of Doran, et al (1976), and setting $\hbar\langle\omega\rangle/k_B=\theta_D$, allows V to be determined by solving (7-1) with T_c equal to the observed value of 5.7K. In chapter 5, values of $N(\epsilon_F)$ as a function of x were obtained using the rigid band charge transfer assumption. Putting these values into the BCS equation (7-1) gives the results shown in figure 52.

The results calculated using rigid band charge transfer and the BCS equation do not agree with any of the data. The lack of precise numerical agreement is not serious, since there is no reason to expect it anyway. What is significant is that although the calculation predicts a T_c which decreases almost monotonically as a function of x, McEwan and Sienko's data show a rapid drop at low x, followed by a recovery between x=.1 and .3. McEwan (1983) has explained

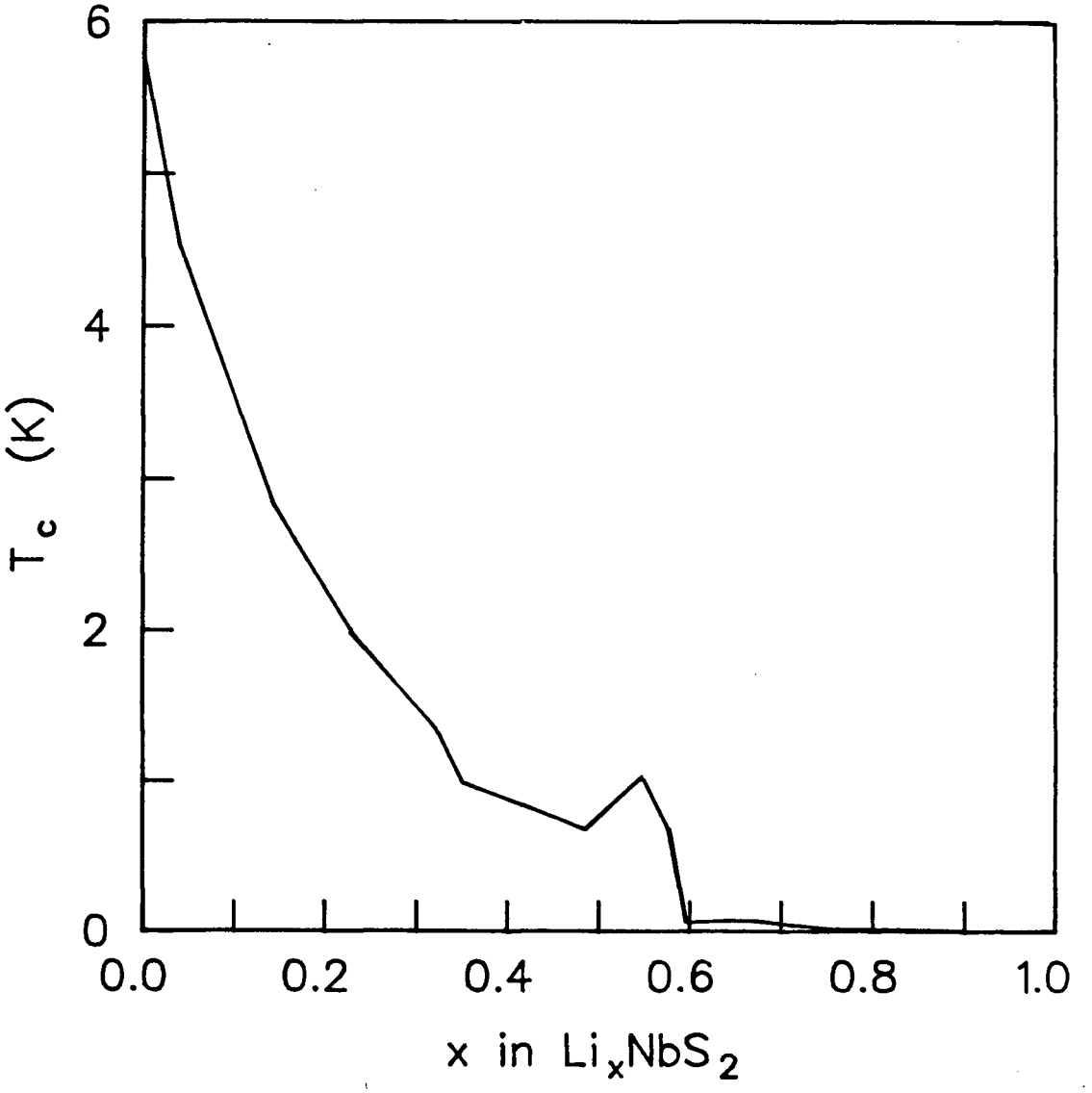

Figure 52: T_c as a function of x, using the rigid band charge transfer model and the BCS equation for T_c (7-1).

the depression of T_c between x≃.02 and .3 in terms of a hypothetical charge density wave which is present only in this composition range. Near x=1/7, some form of lithium ordering along the c-axis with period 7c is supposed to play a role, causing, for example, the lack of any T_c in their x=.15 sample. There are serious problems with this explanation, however. First of all, McEwan searched for evidence of the CDW in the resistivity and magnetic susceptibility, and found none. McEwan also argues that Thompson's empirical relation for CDW transition temperatures in layered transition metal dichalcogenides (Thompson 1975) predicts that a CDW should occur. The Thompson relation is based on the c/a ratio of the crystallographic unit cell. It was not originally intended for use in intercalation compounds. Considering the drastic changes in the Fermi surface that will be produced by intercalation and charge transfer, there is no real reason to expect that the Thompson relation will apply to intercalation compounds. CDW's are now generally believed to be related to Fermi surface nesting (Wilson, et al 1975, Friend and Jerome 1979), and although there may well be a simple relation between Fermi surface geometry and unit cell geometry within a group of materials with similar structures, this will probably break down as soon as intercalation raises the Fermi level. Even if a CDW does occur, it must be a relatively low amplitude, low temperature one, similar to that in $NbSe_2$. Otherwise it

should have been easily observable. In $NbSe_2$, the charge density wave transition temperature T_0 is 33K and T_c is 7.2K. Data on the pressure dependence of T_c (Berthier, et al 1976) gives an idea of the magnitude of the effect that the CDW has on T_c. The application of pressure decreases T_0 and increases T_c, until at 36kbar T_0 disappears and T_c is 8.2K. Further increase in the pressure has little effect on T_c. This can be understood by saying that the CDW opens gaps on the Fermi surface, reducing $N(\epsilon_F)$ and depressing T_c (from 8.2 to 7.2K). Destroying the CDW with pressure then raises T_c. The fractional depression of T_c ($\simeq$12%) by the CDW in $NbSe_2$ is much smaller than the 50% differences between T_c's in Li_xNbS_2 near x=.13 and .25. It may not be possible for a very weak CDW to produce the T_c variations observed. McEwan's evidence for the c-axis lithium ordering is the presence of the (007) Bragg peak, and, as we have seen in section 2.3, this is actually due to a simple stage 2 structure. Ordering along the c-axis with period 7c would give rise to (0,0,1/7) and related peaks, not (007) ones.

A correct and complete explanation of the behavior of T_c as a function of x is not available at present. As we have seen, the rigid band charge transfer model alone cannot explain the data. The behavior of T_c as a function of x should be influenced as well by the large changes in the phonon modes which are caused by intercalation (chapter 6).

The BCS equation tends to overemphasize the importance of the density of states and in any case is valid only in

the limit of weak electron phonon coupling ($\lambda<<1$). Since NbS_2 and its intercalation compounds have the coupling constant λ approximately equal to 1.8 (chapter 5), we are clearly in the regime of 'strong coupling' superconductivity and should really be using a different equation for T_c.

The most widely used such equation is the 'modified McMillan equation' (McMillan 1968, Allen and Mitrovic 1982). This is

$$T_c = \frac{\hbar\omega_{log}}{1.2k_B} \exp\left[\frac{-1.04(1+\lambda)}{\lambda-\mu^*(1+0.62\ )}\right] \qquad (7\text{-}2)$$

where ω_{log} is a logarithmic average phonon frequency, and μ^* is an adjustable parameter of order .1 which represents Coulomb repulsion. This equation was used by Aoki, et al, (1983) to discuss superconductivity in NbS_2 intercalated with organic molecules. Another approach which works well for many materials with $1.2\leq\lambda\leq2.4$ and $.1\leq\mu^*\leq.15$ (the usual range) is the empirical relation of Leavens and Carbotte (1974)

$$T_c=0.1477A \qquad (7\text{-}3)$$

where A is the area under the electron-phonon coupling spectrum $\alpha^2F(\omega)$, that is

$$A = \int_0^\infty \alpha^2F(\omega)\ d\omega \qquad (7\text{-}4)$$

The interaction spectrum $\alpha^2F(\omega)$ is a dimensionless measure of the effectiveness of phonons of frequency ω in scattering electrons between different points on the Fermi surface. It can be obtained from tunneling experiments. The structure in

$\alpha^2F(\omega)$ generally bears a close resemblance to the phonon density of states. The coupling constant λ (also known as the mass enhancement factor), can be related to the interaction spectrum by

$$\lambda = 2 \int_0^\infty \frac{d\omega}{\omega} \alpha^2F(\omega) \qquad (7\text{-}5)$$

for isotropic materials (Allen and Mitrovic 1982).

Although there is insufficient information to actually use the T_c equations (7-2) or (7-3), they do indicate that the phonons and electron-phonon coupling are extremely important in determining T_c. It is clear from the lattice specific heat data that intercalation produces large changes in the phonon spectra, although the low freqency acoustic phonons important in the specific heat are not necessarily the most important in determining T_c.

The mechanism for the T_c variations in Li_xNbS_2 might be revealed by measurements of phonon spectra by tunneling or inelastic neutron scattering. It is not clear, however, that samples of suffient quality to allow these measurements could be prepared using the present methods.

8. CONCLUSION

8.1 SUMMARY OF THIS THESIS

Most of this thesis is concerned with measurements of the low temperature specific heat of Li_xNbS_2. This is the first low temperature specific heat study of lithium intercalation in a layered transition metal dichalcogenide.

Sample preparation was carried out by intercalating lithium into NbS_2 in electrochemical cells. Electrochemical and x-ray diffraction measurements were used to study the structure of Li_xNbS_2. Stage 2 and stage 3 phases were identified for the first time. In addition, there is some preliminary electrochemical evidence for in-plane lithium ordering near $x=1/3$. The extra peaks in $-dx/dV$ which suggest ordering were seen only in electrochemical cells made from freshly prepared NbS_2. The changes in electrochemical behavior may happen because of sulfur loss during storage.

A cryostat suitable for specific heat measurements on small samples of air sensitive compounds was built. It, and the experimental procedure, were described in chapter 3. Measurements were made on NbS_2 and eleven Li_xNbS_2 samples, covering the range $0<x\leq1$.

The original reason for doing this work was to test the rigid band charge transfer model of the electronic properties of intercalation compounds. The results for the electronic specific heat are consistent with complete charge transfer from the intercalated lithium atoms to the bands of

the NbS_2 host. Because the electronic specific heat of Li_xNbS_2 is determined by the filling of the original NbS_2 bands, the data provide information on the electronic density of states of NbS_2. In particular, a shoulder in the density of states predicted by earlier band structure calculations was reflected in the data, and its position was determined.

There were also large changes in the phonon specific heat as a function of x. In chapter 6, we showed that the configurational degrees of freedom of the lithium will not contribute to the low temperature specific heat, since lithium motion will be 'frozen out' at temperatures below about 100 K. Simple models of the vibrational motion of intercalated lithium show that the new vibrational modes due to the addition of lithium are at high frequencies, and will not be seen in the specific heat. Because of this, the data could be discussed in terms of an elastic continuum model of lattice vibrations. The results suggest that intercalation induced changes in the elastic constant c_{44} associated with rigid layer shear are primarily responsible for the changes in phonon specific heat as a function of x. For x less than about .3, c_{44} is significantly lower than in pure NbS_2, indicating that small lithium concentrations between the layers weaken the interlayer shear forces. At higher x, c_{44} increases again, and by x=1 is larger than in NbS_2. This suggests that the bonding in Li_1NbS_2 is more three dimensional than in NbS_2.

Superconductivity in Li_xNbS_2 is discussed briefly in chapter 7. It is shown that the variations in $N(\epsilon_F)$ due to rigid band charge transfer are not sufficient to explain the available data. Intercalation induced changes in the phonon spectrum and the electron-phonon interaction must also be involved.

8.2 SUGGESTIONS FOR FUTURE WORK

The electronic specific heat of Li_xNbS_2 is now reasonably well understood in terms of rigid band charge transfer. The electronic specific heat of other intercalation systems might be of interest. For example TiS_2, which has an empty dz^2 band and is either a semiconductor or semimetal, becomes metallic on intercalation. Li_xTiS_2 would show an electronic specific heat which would increase with x. This might be a good system in which to make detailed comparisons between the data and the predictions of band theorists, since very detailed and supposedly accurate calculations are available for both TiS_2 and Li_1TiS_2 (Umrigar, et al 1983, McCanny 1979).

A class of intercalation hosts for which simple rigid band charge transfer will not work at all are MoS_2 and $Nb_yMo_{1-y}S_2$ $(0<y<1)$. These compounds undergo structural phase transitions when lithium is added. Py and Haering (1983) suggest that the transition is driven by the electronic energy. Electronic specific heat measurements on samples with lithium concentrations near the value at which the

transition occurs could improve our understanding of this process.

The lattice specific heat data show that there is probably a softening of the shear elastic constant c_{44} in samples with $0<x\leq.3$. It is of interest to know whether this is typical of all lithium intercalated transition metal dichalcogenides, or is peculiar to Li_xNbS_2.

As seen in chapters 2 and 6, aging the NbS_2 seems to have had an effect on the electrochemical properties and lattice specific heat of Li_xNbS_2 prepared from it. We have suggested that this may be due to loss of sulfur. It may be possible to test this hypothesis directly by preparing the non-stoichiometric compound $Nb_{1+y}S_2$, with a small well controlled amount y of excess niobium, and then intercalating this with lithium. (It may not, however, be possible to get this to grow in the 2H phase - see Fisher and Sienko 1980.) Another, rather time consuming, approach would be to start with the stoichiometric compound and make a systematic study of the effects of aging and storage conditions on the electrochemical properties.

A series of specific heat measurements on samples prepared from 'fresh' NbS_2 would be of interest. By 'fresh' NbS_2, we mean material which shows the extra peaks in -dx/dV, and which yields specific heat samples which behave like the x=.30 and .16 samples in the present study. It is not yet clear whether the high β values of the x=.30 and .16 samples are related to lithium ordering which was not

present in the other samples, or to the presence of interlayer excess niobium itself. 'Fresh' samples might, in the first case, show peaks in β at x values corresponding to the ordered states, or, in the second case, they might have higher β values throughout the low x range.

The interpretation of the phonon specific heat data in terms of intercalation induced changes in the elastic constant c_{44} suggests a possible application for Li_xNbS_2 or related intercalation compounds. Layered materials, chiefly graphite and MoS_2, are widely used as solid lubricants. Their lubricating ability is related to the fact that because of the relatively weak interlayer interactions, the layers can slide over one another in response to a mechanical force. When some powdered MoS_2, for example, is placed between two sliding surfaces, layer slipping allows it to spread into a smooth lubricating film. A low value of c_{44} means that the interlayer shear forces are weak, and that layer slipping can occur easily. If we assume that the other elastic constants have values close to the ones we used for NbS_2, the specific heat results for $Li_{.16}NbS_2$ imply that it had $c_{44} \simeq .2 \cdot 10^{10} N/m^2$. For comparison, graphite and MoS_2 have $C_{44} \simeq .4 \cdot 10^{10} N/m^2$ and $1.9 \cdot 10^{10} N/m^2$, respectively (Wakabayashi and Nicklow 1979, Feldman 1976). It is possible, therefore, that Li_xNbS_2 with $0<x<.4$ may be a superior solid lubricant for critical applications, and its lubricating properties should be investigated. Although the presence of reactive lithium might seem to rule out the

practical use of Li_xNbS_2, solid lubricants are often used mixed with grease or oil, and this might be sufficient to protect the intercalation compound from air. It may also be that layer compounds intercalated with other, less reactive, species will show similar behavior.

As mentioned in chapter 7, the superconducting properties of Li_xNbS_2 remain something of an enigma. It should be pointed out that the superconducting transition temperature of Li_xNbSe_2 varies as a function of x in a way that is very different than for Li_xNbS_2 (McEwan 1983). McEwan's measurements on Li_xNbSe_2 were made on samples prepared at high temperatures. The samples had the 2H structure, and the presence of (007) and (009) Bragg peaks in the x-ray diffraction patterns for some of the samples indicates the presence of a stage 2 phase similar to that in Li_xNbS_2, and in Li_xNbSe_2 prepared by electrochemical intercalation (D.C.Dahn and R.R.Haering 1982). The band structure of $NbSe_2$ is very similar to that of NbS_2 (Wexler and Wooley 1976). In spite of the fact that its host band structure and staging behavior are almost identical to those of Li_xNbS_2, T_c for Li_xNbSe_2 is a smooth monotonically decreasing function of x. The reasons for the drastically different $T_c(x)$ behavior in these two compounds is an intriguing problem to be solved by future research.

BIBLIOGRAPHY

Allen, P.B., and Mitrovic, B. 1982. In Solid State Physics, vol 37, (ed. H.Ehrenreich, F.Seitz, and D.Turnbull), Academic Press, N.Y.

Anderson, P.W., Halperin, B.I., and Varma, C.M. 1972. Phil. Mag. 25, 1.

Ashcroft, N.W., and Mermin, N.D. 1976. Solid State Physics, Holt, Rinehart, and Winston, N.Y.

Aoki, R., Nakamura, S., and Wada, S. 1983. Synthetic Metals 6, 193.

Auld, B.A. 1973. Acoustic Fields and Waves in Solids, vol 1, Wiley, N.Y.

Bachmann, R., DiSalvo, F.J., Geballe, T.H., Greene, R.L., Howard, R.E., King, C.N., Kirsh, H.C. Lee, K.N., Schwall, R.E., Thomas, H.U., and Zubeck, R.B. 1972. Rev. Sci. Instr. 43, 205.

Bardeen, J., Cooper, L.N., and Schrieffer, J.R. 1957. Phys. Rev. 106, 162, *ibid*, 108, 1175.

Berthier, C., Molinie, P., and Jerome, D. 1976. Solid State Commun. 18, 1393.

Bevington, P.R. 1969. Data Reduction and Error Analysis for the Physical Sciences, McGraw-Hill, N.Y. Chapter 11.

Born, M, and Huang, K, 1954. Dynamical Theory of Crystal Lattices, Oxford University Press, London.

Carslaw, H.S., and Jaeger, J.C., 1959. Conduction of Heat in Solids, 2nd ed., Oxford University Press, Oxford.

Dahn, D.C., and Haering, R.R. 1982. Solid State Commun., 44, 29.

Dahn, J.R., McKinnon, W.R., Haering, R.R., Buyers, W.J.L., and Powell, B.M. 1980. Can. J. Phys. 58, 207.

Dahn, J.R. 1982. Ph.D. Thesis, University of British Columbia, Vancouver.

Dahn, J.R., Dahn, D.C., and Haering, R.R., 1982. Solid State Commun. 42, 179.

Dahn, J.R., Py, M.A., and Haering R.R. 1982. Can. J. Phys. 60, 307.

Dahn, J.R., and Haering, R.R. 1983. Can. J. Phys. 61, 1093.

Dahn, J.R., and McKinnon, W.R. 1984a. J. Electrochem. Soc. 131, 1823.

Dahn, J.R., and McKinnon, W.R. 1984b. J. Phys. C. 17, 4231.

Daumas, N., and Herold, A. 1969. C. R. Hebd. Seanc. Acad. Sci., Paris C 268, 373.

DiPietro, B., Patriarca, M., and Scrosati, B. 1982. Synthetic Metals, 5, 1

Doran, N.J., Ricco, B., Titterington, D.J., and Wexler, G. 1978. J. Phys. C. 11, 685.

Dutcher, J.R. 1985. M.Sc. Thesis, University of British Columbia, Vancouver.

Fagaly, R.L., and Bohn, R.G., 1977. Rev. Sci. Instr. 48, 1502.

Feldman, J.L., 1976. J. Phys. Chem. Solids 37, 1141, see also Erratum (1981), 42, 1029.

Feldman, J.L., 1982. Phys. Rev. B 25, 7132.

Fisher, W.G., and Sienko, M.J., 1980. Inorg. Chem., 19, 39.

Friend, R.H., and Jerome, D. 1979. J. Phys. C. 12, 1441.

Frindt, R.F., and Huntley, D.J. 1976. In Optical and Electrical Properties, (ed. P.A.Lee), Reidel, Dordrecht. p403.

Gmelin, E. 1979. Thermochim. Acta 29, 1

Haag, J., von Alpen, U., Gmelin, E. and Rabenau, A. 1979. Z. Naturforsh. A 34, 969.

Hibma, T. 1982. In Intercalation Chemistry (ed. M.S.Whittingham and A.J.Jacobson) Academic Press, N.Y., p 285.

Holleck, G.L., Schuker, F.S., and Brummer, S.B. 1975. In Proc. Tenth Intersociety Energy Conversion Eng. Conf., IEEE, N.Y. p1.

Hulliger, F. 1976. Structural Chemistry of Layer-Type Phases, Reidel, Dordrecht.

Hunklinger, S., Piche, L., Lasjaunias, J.C., and Dransfeld, K. 1975. J. Phys. C 8, L423.

Ibers, J.A., and Hamilton, W.C. 1974. (ed) International Tables for X-ray Crystallography, vol 4, Kynoch, Birmingham.

Jericho, M.H., Simpson, A.M., and Frindt, R.F. 1980. Phys. Rev. B 22, 4907.

Johnson, G.W. 1982. M.Sc. Thesis, University of British Columbia, Vancouver.

Jones, R.E.,Jr., Shanks, H.R., Finnemore, D.K., and Morosin, B. 1972. Phys. Rev. B 6, 835.

Kaluarachchi, D., and Frindt, R.F. 1983. Phys. Rev. B 28, 3663.

Kleinberg, R.L. 1983. J. Phys. Chem. Solids 43, 285.

Kobayashi, M., and Mizoguchi, N. 1984. J.Phys. Soc. Japan 53, 2353.

Lasjaunias, J.C., Picot, B., Ravex, A., Thoulouze, D., and Vandorpe, M., 1977. Cryogenics, 17, 111.

Leavens, C.R., and Carbotte, J.P., 1974. J. Low Temp. Phys. 14, 195.

Levy, F. 1979. (ed.) Intercalated Layer Materials, Reidel, Dordrecht.

Lieth, R.M.A., and Terhell, J.C.J.M, 1977. In Preparation and Crystal Growth of Materials with Layered Structures, (ed. R.M.A. Lieth), Reidel, Dordrecht.

Marseglia, E.A. 1983. Int. Rev. Phys. Chem. 3, 177.

Mattheiss, L.F., 1973. Phys. Rev. B 8, 3719.

McEwan, C.S. 1983. Ph.D. Thesis, Cornell University, Ithaca, N.Y.

McEwan, C.S. and Sienko, M.J. 1982. Rev. de Chim. Minerale 19 309.

McKinnon, W.R., and Dahn, J.R. 1983. Solid State Commun. 48, 43.

McKinnon, W.R., and Haering, R.R. 1983. In Modern Aspects of Electrochemisry 15, (ed. R.E.White, J.O'M.Bockris, and B.E.Conway), Plenum, N.Y. p235.

McMillan, W.L. 1968. Phys. Rev. 168, 331.

McMullen, W.G., and Irwin, J.C. 1984. Can. J. Phys. 62, 789.

Millman, S.E., and Kirczenow, G. 1983. Phys. Rev. B 28, 3482.

Molinie, P., Jerome, D., and Grant, A.J. 1974. Phil. Mag., ser.8, 30, 1091.

Moncton, D.E., Axe, J.D., and DiSalvo, F.J. 1977. Phys. Rev. B 16, 801.

Moore, C. 1981. UBC Curve, UBC Computing Centre, Vancouver.

Mulhern, P.J., 1982. M.Sc. Thesis, University of British Columbia, Vancouver.

Nakamura, S., and Aoki, R., 1983. Synthetic Metals 6, 201.

Partington, J.R. 1952. An Advanced Treatise on Physical Chemistry, Longmans Green, London. Vol 3, Chap M.

Pryce, M.H.L. 1969. In Modern Solid State Physics, vol.2, (ed. R.H.Enns and R.R.Haering), Gordon and Breach, N.Y.

Py, M.A., and Haering, R.R. 1983. Can. J. Phys.61, 76.

Rau, H., Kutty, T.R.N., Guedes de Carvalho, J.R.F. 1973. J. Chem. Thermodyn., 5, 833.

Rosenbaum, R.L. 1968. Rev. Sci. Instr. 39, 890.

Safran, S.A. 1980. Phys. Rev. Lett. 44, 937.

Schober, T., and Wenzl, H. 1978. In Hydrogen in Metals II, ed. by G.Alefeld and J.Volkl, Springer-Verlag, Berlin. p11.

Schollhorn, R. and Kumpers, M. 1979. Mat. Res. Bull. 14, 1039.

Scholz, G.A., and Frindt, R.F. 1980. Mat. Res. Bull. 15, 1703.

Schwall, R.E, Stewart, G.R., and Geballe, T.H. 1976. J. Low Temp. Phys. 22, 557.

Sellers, G.J., and Anderson, A.C. 1974. Rev. Sci. Instr. 45, 1256.

Sharma, S.R., and Bergersen, B. 1984. Phys. Rev. B 30, 6586.

Silbernagel, B.G. 1975. Solid State Commun. 17, 361.

Sparks, L.L., and Powell, R.L. 1972. J. Res. Nat. Bureau of Standards 76A, 263.

Stewart, G.R. 1983. Rev. Sci. Instr. 54, 1.

Sullivan, P.F., and Seidel, G. 1968. Phys. Rev. 173, 679.

Tinkham, M. 1975. Introduction to Superconductivity, McGraw-Hill, N.Y.

Torikachvili, M.S, Yang, K.N., Calvo, R., Nascimento, O.R., and Maple, M.B. 1983. Cryogenics 23, 52.

Van Maaren, M.H., and Harland, H.B. 1969. Phys. Lett. 29A, 571.

Van Maaren, M.H., and Schaeffer, G.M. 1966. Phys. Lett. 20, 131.

Vandenberg-Voorhoeve, J.M. 1976. In Optical and Electrical Properties, (ed. P.A.Lee), Reidel, Dordrecht. p423.

Von Lohneysen, H., Schink, H.J., Arnold, W., Beyeler, H.U., Pietronero, L., and Strassler, S. 1981. Phys. Rev. Lett. 46, 1213.

Wakabayashi, N., and Nicklow, R.M. 1979. In Electrons and Phonons in Layered Crystal Structures, (ed. T.J.Weiting and M.Schluter), Reidel, Dordrecht. p409.

Warren, B.E., 1969. X-ray Diffraction, Addison-Wesley, N.Y.

Weast, R.C. 1970. Handbook of Chemistry and Physics, Chemical Rubber Co., Cleveland.

Wexler, G., and Wooley, A.M. 1976. J. Phys. C. 9, 1185.

White, G.K. Experimental Techniques in Low Temperature Physics, Clarendon Press, Oxford.

Whittingham, M.S. 1976. Science 192, 1126.

Whittingham, M.S. 1978. Prog. Solid State Chem. 12,41.

Whittingham, M.S., and Jacobsen, A.J. 1982. (ed) Intercalation Chemistry, Academic Press, N.Y.

Williams, P.M. 1976. In Crystallography and Crystal Chemistry of Materials with Layered Structures (ed. F.Levy), Reidel, Dordrecht. p51.

Wilson, J.A., DiSalvo, F.J., and Mahajan, S. 1975. Adv. Phys. 24, 117.

Wilson, J.A., and Yoffe, A.D. 1969. Adv. Phys. 18, 193.

Yoffe, A.D. 1973. Ann. Rev. Mat. Sci. 3, 147.

Yoffe, A.D. 1982. Ann. Chim. Fr. ser.15, 7, 215.

Zemansky, M.W. 1957. Heat and Thermodynamics, McGraw-Hill, N.Y. p394.

APPENDIX 1: INTENSITIES OF X-RAY BRAGG PEAKS FOR STAGE TWO Li_xNbS_2

The purpose of this appendix is to briefly outline a calculation of the Bragg peak intensities for stage 2 Li_xNbS_2, to present the results, and to compare them with measurements on $Li_{.14}NbS_2$ made using an electrochemical cell with a beryllium x-ray window. Portions of this data have already been presented in figure 6(d). The hexagonal lattice parameters were c=12.35 Å and a=3.330 Å.

To calculate the intensities we need to know the positions of the atoms in the unit cell. Atom positions will be given in terms of the three basis vectors $\vec{c}$, $\vec{a}_1$, and $\vec{a}_2$. $\vec{c}$ has length c and lies in the direction normal to the layers. $\vec{a}_1$ and $\vec{a}_2$ both have length a, lie in a plane parallel to the layers, and make an angle of 120° with each other. In the notation to be used (p,q,r) indicates a position $p\vec{a}_1+q\vec{a}_2+r\vec{c}$. Picking the origin to lie halfway between the two niobium atoms in the unit cell (that is, at one of the octahedral sites in the gap), the atom positions for the 2H-NbS_2 structure are (see figure 2):

Nb at ±(0,0,-1/4)

S at ±(1/3,2/3,z), ±(1/3,2/3,1/2-z)

where z is defined in figure A1-1. These atom positions lead to a structure factor of zero for (00*l*) Bragg reflections with *l* odd. The exact value of z for NbS_2 is not known, but, as in most of the 2H transition metal dichalcogenides, it is approximately 1/8 (Hulliger 1976). The extinction of (00*l*)

peaks with l odd does not depend on the value of z.

To get atom positions for stage 2 Li_xNbS_2, we start by taking z=1/8 in pure NbS_2. We then make the assumption that the change in the c-axis in going from NbS_2 to stage 2 Li_xNbS_2 is due entirely to the expansion of only one of the two interlayer gaps in the unit cell (we choose the one at the origin). This is shown schematically in figure A1-1. Since the scattering factor of lithium is very low, the inclusion of the lithium in the calculation makes little difference in the results. The most important factor determining the intensities is the gap expansion. For completeness, however, we will include the intercalated lithium, and will assume it lies in the octahedral sites in the expanded gap. There is not a lithium atom in every unit cell, so for the purposes of the intensity calculation we take the scattering factor at the lithium site to be 2x times the scattering factor of a lithium atom. Here x is the overall value in Li_xNbS_2. Since every second gap is empty, the concentration in the filled gaps is 2x. In terms of the expanded unit cell, the atom positions in stage 2 Li_xNbS_2 are:

Nb at ±(0,0,-.257)

S at ±(1/3,2/3,.136), ±(1/3,2/3,.379)

2x Li at (0,0,0)

Starting with these atom positions, the integrated intensities of the peaks were calculated using a computer

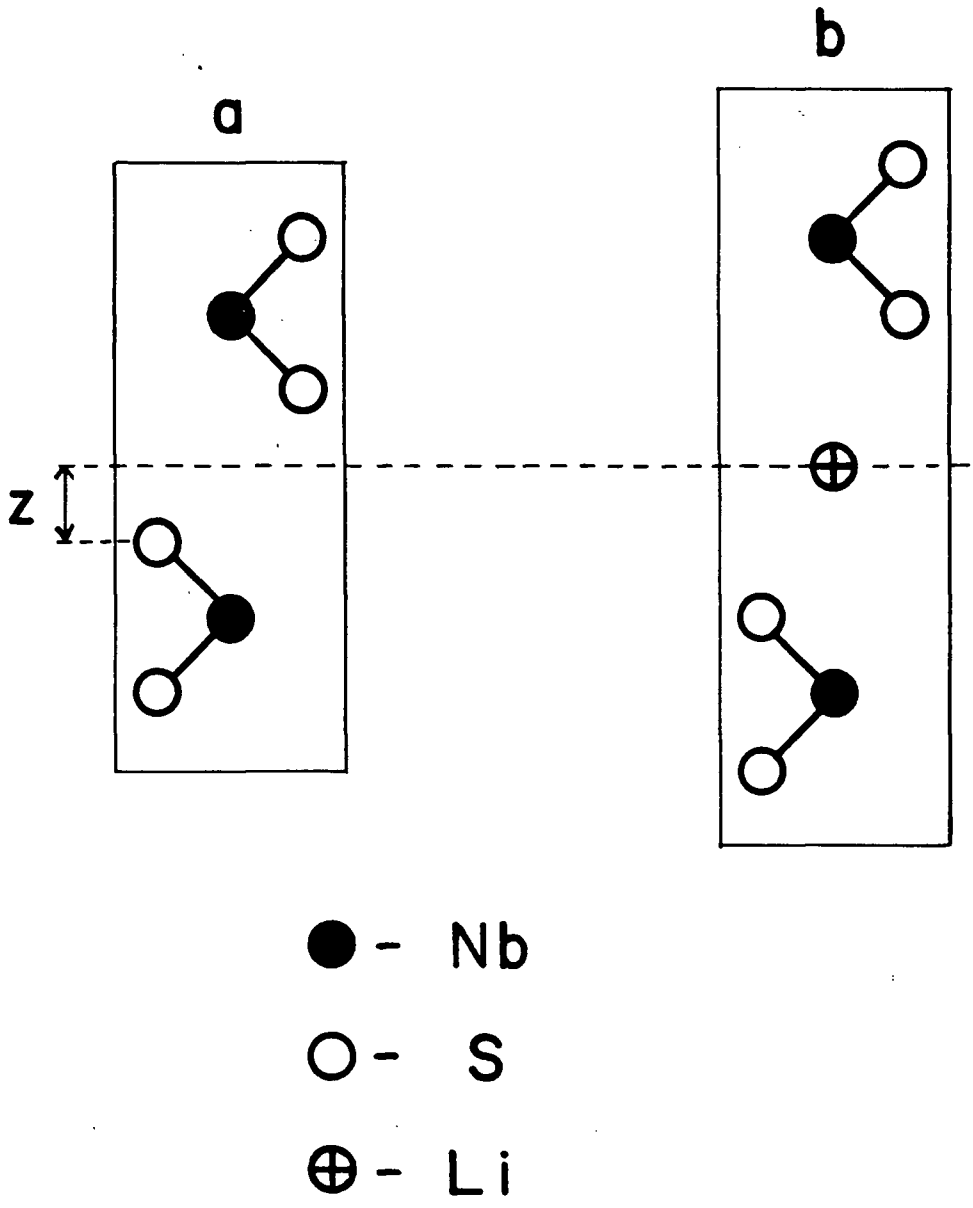

Figure A1-1: Projections onto a (110) plane of the unit cells of
a- NbS_2
b- stage 2 Li_xNbS_2.
(not to scale)

program written by R.Marselais[27]. The program begins by calculating the structure factor F in the usual way. Atomic scattering factors from Ibers and Hamilton (1974) were used. The measurements were made with a Philips PW1050/70 vertical goniometer, which uses the Bragg-Brentano pseudofocusing geometry shown in figure A1-2. For a goniometer with an angular divergence δ of the incident beam, and a diffracted beam monochromator, the integrated intensity of a Bragg peak centered at angle 2θ is (for a thick sample)

$$I = I_0 m |F|^2 \delta \left[\frac{1+\cos^2 2\theta \cos^2 2\phi}{\sin\theta \sin 2\phi} \right] \qquad \text{(A1-1)}$$

where I_0 is a constant, m is the multiplicity of the reflection, and the angles θ and ϕ are defined in the figure. The results of calculations using (A1-1) are listed in table A1-I for peaks at angles $2\theta<90°$. They are in the column labelled 'standard intensity'.

In our diffactometer, δ is not constant because of a Philips PW1386/50 automatic divergence slit, which instead of providing a beam of constant divergence as would a fixed slit, keeps the illuminated area of the sample approximately constant. In addition, when using an x-ray cell, the intensities must be corrected for absorption in the beryllium window. Corrections for these effects have been discussed by Py and Haering (1983) and J.R.Dahn (1982), and are included in the computer program. The corrected

---

[27]XBAT:SPECTRUM.S

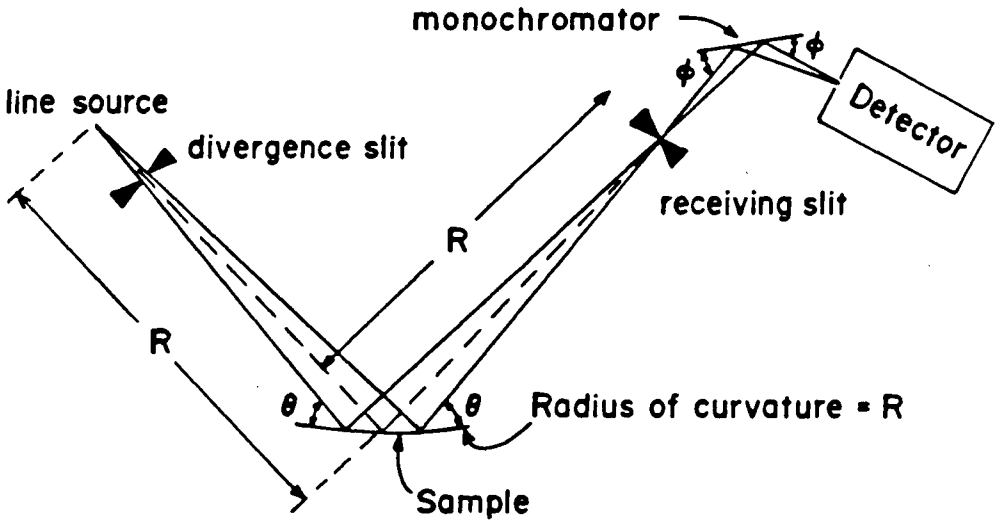

Figure A1-2: The Bragg-Brentano focusing geometry. In most diffractometers the sample is flat, not curved. Because the sample dimensions are much less than R, the focusing condition is still approximately satisfied, hence pseudofocusing.

intensities are also included in the table, as are the diffaction angles 2θ calculated for copper Kα radiation.

Detailed comparison of all the intensities with experiment was not done. This would be difficult because of preferred orientation effects (the calculation assumes random orientation in the powder sample), and in any case we are primarily interested in the (00l) peaks, especially those with l odd. Calculated and observed relative integrated intensities for the (00l) lines are given in table A1-II. Preferrred orientation should have an equal effect on all of the lines in this group. The agreement between calculated and experimental values is reasonably good. The calculation shows why, of all the (00l) peaks with l odd, only the (007) and (009) peaks have been observed in stage 2 Li_xNbS_2 and stage 2 Li_xNbSe_2 (this work, McEwan 1983, D.C.Dahn and Haering 1982).

The (009) peak was considerably wider than the other observed (00l) peaks. The full width at half maximum of the (009) peak was $\simeq .7^\circ$ in 2θ, while the (008) peak, for example, was $.3^\circ$ wide. This indicates some disorder in the staging sequence. It can be shown (J.R.Dahn 1982), that staging disorder broadens the (00l) lines with l odd much more than those with l even.

The experimental (10l) lines had relative intensities in qualitative agreement with the calculation. Since these lines depend strongly on the stacking sequence of the NbS_2 layers, this agreement indicates that the host stacking

sequence is not affected by intercalation (that is, it is still BaB-CaC in the notation of section 1.2).

Table A1-I

Calculated integrated intensities and angles for stage 2 Li_xNbS_2 (see text).

h	k	l	2θ (degrees)	Standard Intensity (relative)	Corrected Intensity (relative)
0	0	1	7.15	0.74	0.07
0	0	2	14.34	100.00	48.08
0	0	3	21.57	0.40	0.39
0	0	4	28.90	1.78	2.71
1	0	0	30.98	20.76	34.85
1	0	1	31.84	7.87	13.73
1	0	-1	31.84	8.54	14.90
1	0	2	34.29	31.58	61.04
1	0	-2	34.29	31.21	60.32
0	0	5	36.35	0.07	0.14
1	0	3	38.07	8.89	19.78
1	0	-3	38.07	0.82	1.82
1	0	4	42.88	27.49	71.52
1	0	-4	42.88	38.44	100.00
0	0	6	43.97	4.00	10.75
1	0	5	48.49	6.42	19.56
1	0	-5	48.49	0.33	1.00
0	0	7	51.79	0.82	2.71
1	0	6	54.76	7.95	28.16
1	0	-6	54.76	8.75	31.01
1	1	0	55.11	24.21	86.46
1	1	1	55.65	0.03	0.12
1	1	2	57.26	15.23	57.00
1	1	3	59.87	0.16	0.63
0	0	8	59.88	5.27	20.82
1	0	-7	61.58	2.21	9.04
1	1	4	63.42	1.55	6.58
2	0	0	64.58	2.59	11.21
2	0	1	65.07	0.89	3.90
2	0	-1	65.07	0.81	3.54
2	0	2	66.54	4.34	19.42
2	0	-2	66.54	4.38	19.64
1	1	5	67.83	0.07	0.33
0	0	9	68.32	0.58	2.69
2	0	3	68.95	0.11	0.53
2	0	-3	68.95	1.39	6.48
1	0	8	68.96	3.25	15.17
1	0	-8	68.96	0.86	4.04

Table A1-I (Continued)

h	k	l	2θ (degrees)	Standard Intensity (relative)	Corrected Intensity (relative)
2	0	4	72.26	7.77	38.24
2	0	-4	72.26	5.59	27.53
1	1	6	73.04	5.18	25.81
2	0	5	76.43	0.08	0.42
2	0	-5	76.43	1.62	8.48
1	0	9	76.89	0.07	0.40
1	0	-9	76.89	1.61	8.47
0	0	10	77.20	1.04	5.53
1	1	7	79.02	1.40	7.58
2	0	6	81.43	2.77	15.50
2	0	-6	81.43	2.51	14.07
1	0	10	85.48	1.81	10.63
1	0	-10	85.48	1.31	7.70
1	1	8	85.77	11.81	69.62
0	0	11	86.67	0.11	0.64
2	0	7	87.26	0.87	5.21
2	1	0	89.93	2.19	13.51

Table A1-II

Integrated (00*l*) intensities for stage 2 Li_xNbS_2. The (007) peak was not observed because its position coincided with a beryllium Bragg peak originating in the cell window. The (002) peak may have been partially obstructed by the cell case.

Peak	Calculated Corrected Intensity (relative to (008))	Observed Intensity (relative to (008))
(001)	0.35	out of range
(002)	230	150
(003)	1.9	not observed
(004)	13	12
(005)	0.67	not observed
(006)	51	70
(007)	13	obscured by Be
(008)	100	100
(009)	13	15
(0010)	27	20
(0011)	3.0	not observed

APPENDIX 2: SOLUTION OF THE HEAT FLOW EQUATIONS

This Appendix contains the solution of the heat flow problem for a relaxation time heat capacity measurement in which the sample's thermal conductivity is finite. Some of the results are given in Bachmann, et al (1972), but it will be useful to outline the derivation here. Also, in the cryostat used in this work, the heat capacity of the wires which support the sample platform is very small compared to the heat capacities of the sample and the platform. This leads to a useful simplification of the resulting equations, which is also discussed.

Consider the system of figure A2-1. If the thermal conductivity of the platform is high enough that it is always essentially isothermal, and if there is no heat loss from the sample's edges, the temperature in the sample will be a function only of z, the coordinate normal to the plane of the platform. In this case, we have a one-dimensional heat flow problem.

It is convenient to work in terms of a relative temperature

$$\theta(z,t)=T(z,t)-T_o \qquad \text{(A2-1)}$$

where T_o is the temperature of the block. The heat equation for an inhomogeneous system is then (Carslaw and Jaeger 1959)

$$\frac{\partial}{\partial z}\left[K(z)\frac{\partial}{\partial z}\theta(z,t)\right] = s(z)\frac{\partial}{\partial t}(z,t) \qquad \text{(A2-2)}$$

where s(z) is the heat capacity per unit length and K(z) is

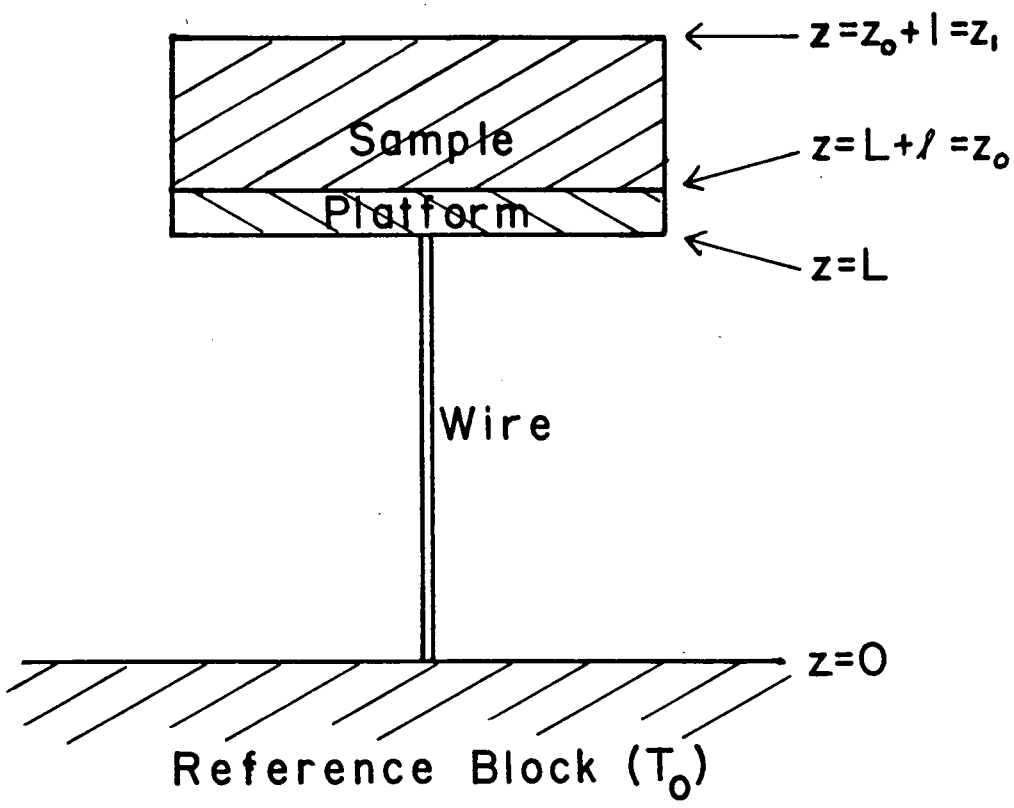

Figure A2-1: Model system for heat flow calculations.

the (1D) thermal conductivity. The thermal diffusivity $K(z)/s(z)$ is constant in each of the three parts of the system and can be described by

$$\begin{aligned} s(z)/K(z) &= C_w/k_w L^2 && 0<z<L \\ s(z)/K(z) &= C_{pl}/k_{pl} l^2 && L<z<z_0 \\ s(z)/K(z) &= C_s/k_s l^2 && z_0<z<z_1 \end{aligned} \qquad \text{(A2-3)}$$

where the C's and k's are, respectively, the appropriate heat capacities and thermal conductances of the parts.

At $z=0$, the temperature is fixed at the block temperature, and at $z=z_1$ there is no heat flow, so the boundary conditions are

$$\theta(0,t)=0 \qquad \text{(A2-4)}$$

$$\partial\theta(z_1,t)/\partial z=0 \qquad \text{(A2-5)}$$

At the internal boundaries $z=L, z_0$ we require that the heat flow be continuous:

$$K(z)\ \partial\theta(z,t)/\partial z \text{ continuous at } z=z_0, L \qquad \text{(A2-6)}$$

If there is no thermal contact resistance at either of the boundaries, we also have

$$\theta(z,t) \text{ continuous at } z=z_0, L \qquad \text{(A2-7)}$$

The case of a non-zero thermal boundary resistance (e.g. a poor grease joint) has been treated by Bachmann, et al (1972).

To solve (A2-2), we begin by separating variables

$$\theta(z,t)=\phi(z)\psi(t) \qquad \text{(A2-8)}$$

Then, defining the separation constant as $-1/\tau$,

$$\frac{\frac{1}{s(z)}\frac{d}{dz}\left[K(z)\frac{d\phi}{dz}\right]}{\phi} = \frac{\frac{d\psi}{dt}}{\psi} = -\frac{1}{\tau} \qquad \text{(A2-9)}$$

which gives

$$\psi(t)=e^{-t/\tau} \qquad \text{(A2-10)}$$

and

$$\frac{d}{dz}\left[K(z)\frac{d\phi}{dz}\right] + \frac{s(z)}{\tau}\phi = 0 \qquad \text{(A2-11)}$$

Equation (A2-11) and the boundary conditions define a Sturm-Liouville system. The eigenfunction solutions will be called ϕ_n and the corresponding eigenvalues τ_n. Using the homogeniety of the boundary conditions, it can be shown that the eigenfunctions are orthogonal with respect to s(z), that is ,

$$\int_0^{z_1} s(z)\phi_n(z)\phi_m(z)dz=0; \qquad m\neq n \qquad \text{(A2-12)}$$

(Strictly speaking, we must also require s(z) and K(z) to be continuous; for this reason (A2-3) should be considered only an approximation to the actual s(z) and K(z) which change rapidly but continuously at z=1 and $z=z_0$.)

The next step is to find the ϕ_n. The following form

satisfies (A2-11) and the boundary conditions;

$$\begin{aligned} \phi_n(z) &= \sin\lambda_n z && 0\le z\le L \\ \phi_n(z) &= a\cos\gamma_n z + b\cos\gamma_n && L\le z\le z_o \\ \phi_n(z) &= d\cos\mu_n(z_1-z) && z_o\le z\le z_1 \end{aligned} \tag{A2-13}$$

where

$$\begin{aligned} (\lambda_n L)^2 &= C_w/k_w\tau_n \\ (\gamma_n l)^2 &= C_{pl}/k_{pl}\tau_n \\ (\mu_n 1)^2 &= C_s/k_s\tau_n \end{aligned} \tag{A2-14}$$

and a, b, and d are constants to be determined from the internal matching conditions (A2-6) and (A2-7). These conditions yield the equations

$$\begin{aligned} \sin\lambda_n L &= a\sin\gamma_n L + b\cos\gamma_n L \\ d\cos\mu_n 1 &= a\sin\gamma_n(L+l) + b\cos\gamma_n(L+l) \\ \lambda_n k_w L\cos\lambda_n L &= a\gamma_n k_{pl} l\cos\gamma_n L - b\gamma_n k_{pl} l\sin\gamma_n L \\ d\mu_n k_s 1\sin\mu_n 1 &= a\gamma_n k_{pl} l\cos\gamma_n(L+l) \\ &\quad - b\gamma_n k_{pl} l\sin\gamma_n(L+l) \end{aligned} \tag{A2-15}$$

We will be interested in the case $k_{pl}\to\infty$ (or $\gamma_n\to 0$), so the problem can be simplified by expanding the right hand sides of these equations to order γ_n^2. Doing this and solving the first three equations for a, b, and d gives

$$\begin{aligned} a &\simeq \gamma_n L\sin\lambda_n L + (\lambda_n L k_w l\tau_n/C_{pl})\cos\lambda_n L \\ b &\simeq \sin\lambda_n L(1-\gamma_n^2 L/2) - (\lambda_n L^2 k_w l\tau_n/C_{pl})\gamma_n^2\cos\lambda_n L \\ d &\simeq \sin\lambda_n L/\cos\mu_n 1 \end{aligned} \tag{A2-16}$$

Substituting these into the fourth equation of (A2-15) and dropping terms of order γ_n^2 gives the eigenvalue equation

$$-(C_w/\lambda_n L)\cot\lambda_n L + (C_s/\mu_n l)\tan\mu_n l + C_{pl} = 0 \qquad \text{(A2-17)}$$

which is valid in the limit $k_{pl}\to\infty$. (This equation can also be derived by taking $k_{pl}=\infty$ at the start of the problem, that is, taking the sample platform to be isothermal. In this case, the internal matching condition (A2-6) is meaningless and must be replaced by a heat balance equation for the platform, which then reduces directly to (A2-17).)

Therefore, the eigenfunctions ϕ_n are given by

$$\begin{aligned} \phi_n &= \sin\lambda_n z && 0\le z\le L \\ \phi_n &= \sin\lambda_n L && L\le z\le z_0 \\ \phi_n &= \sin\lambda_n L\,\cos\mu_n(z_1-z)/\cos\mu_n l && z_0\le z\le z_1 \end{aligned} \qquad \text{(A2-18)}$$

where μ_n and λ_n are defined in terms of τ_n by (A2-14) and τ_n is the n^{th} solution of the eigenvalue equation (A2-17).

The solution to the entire time-dependent heat flow problem is then

$$\theta(z,t) = \sum_{n=1}^{\infty} A_n\phi_n(z)\, e^{-t/\tau_n} \qquad \text{(A2-19)}$$

where the coefficients A_n are determined by the initial conditions. In the case of a relaxation time heat capacity measurement, we take t=0 to be the time the sample heater is switched off. Heat has been supplied to the sample platform at a rate P for t<0. Thus the initial condition is

$$\theta(z,0)=\theta_0=P/k_w \qquad L\le z\le z_1 \qquad \text{(A2-20)}$$

$$\theta(z,0)=\theta z/L \qquad 0\le z\le L$$

So, since the ϕ_n form an orthogonal basis,

$$A_n = \frac{\int_0^z dz\ s(z)\theta(z,0)\phi_n(z)}{\int_0^z dz\ s(z)\{\phi_n(z)\}^2} \qquad \text{(A2-21)}$$

Evaluating the integrals and using (A2-14) and (A2-17) gives

$$A_n = \frac{2\theta_0 C_w}{C_s\lambda_n^2 L^2 \sin\lambda_n L}\left(1+\tan^2\mu_n 1 \mp \frac{C_w}{C_s}(1+\cot^2\lambda_n L) + \frac{C_{pl}}{C_s}\right)^{-1} \qquad \text{(A2-22)}$$

which, together with (A2-14), (A2-17), (A2-18), and (A2-19), completely specifies the solution.

Bachmann, et al (1973) outline a method of data analysis which is based on a numerical solution of equations (A2-17) and(A2-22) with n=1. It uses as input data the values of C_w, k_w, C_{pl}, τ_1, and $A_1\phi_1(L)/\theta_0$. C_{pl} and C_w must be known beforehand; the other values can be determined from a fit to the thermal decay data. ($A_1\phi_1(L)$ is available from the data because the temperature is measured at the platform, that is, at z=L.)

In the cryostat used for this work, however, the wire heat capacity C_w is not accurately known. It is, however, much smaller than either the platform heat capacity C_{pl} or the sample heat capacity C_s. Rough estimates also show that $C_w/k_w\tau_1=(\lambda_1 L)^2$ is typically about .02, and that C_s/C_w is of

order 100. It is therefore useful to examine the equations in the limit where C_w and $\lambda_1 L$ are small. Setting $\tan\lambda_1 L \simeq \lambda_1 L$ in (A2-22), and using the fact that $C_w << C_s$, gives

$$\frac{A_1 \sin\lambda_1 L}{\theta_0} = \frac{2k_w\tau_1}{C_s(1+\tan^2\mu_1 l) + k_w\tau_1 + C_{pl}} \qquad \text{(A2-23)}$$

Treating the eigenvalue equation (A2-17) the same way and solving for C_s gives

$$C_s = (k_w\tau_1 - C_{pl})\mu_1 l/\tan\mu_1 l \qquad \text{(A2-24)}$$

Substituting this into (A2-23) gives

$$\frac{A_1 \sin\lambda_1 L}{\theta_0} = \frac{2k_w\tau_1}{\mu_1 l(\cot\mu_1 l + \tan\mu_1 l)(k_w\tau_1 - C_{pl}) + k_w\tau_1 + C_{pl}} \qquad \text{(A2-25)}$$

Section 3.4.2 describes how (A2-24) and (A2-25) were used in analysis of Li_xNbS_2 specific heat data. In the notation used there, $A_1 \sin\lambda_1 L$ is θ_1.